Formation of narrow optical resonances in thin atomic vapor layers of Cs, Rb, K and applications.

Arevik Amiryan

UNIVERSITÉ BOURGOGNE FRANCHE-COMTÉ
Laboratoire Interdisciplinaire Carnot de Bourgogne – UMR CNRS 6303

NATIONAL ACADEMY OF SCIENCES OF ARMENIA
Institute for Physical Research

FORMATION OF NARROW OPTICAL RESONANCES IN THIN ATOMIC VAPOR LAYERS OF Cs, Rb, K AND APPLICATIONS

by

Arevik AMIRYAN

A Thesis in Physics
Submitted for the Degree of Doctor of Philosophy

Date of defense September 18 2019

Jury

Mr Claude LEROY	Professor Dijon, ICB – UBFC	Supervisor
Mr David SARKISYAN	Professor Ashtarak IPR – NAS	Supervisor
Mr Wojciech GAWLIK	Professor Krakow, JU	Referee
Mr Marcis AUZINSH	Professor Riga, UL	Referee
Mr Tigran VARTANYAN	Professor Saint Petersburg, ITMO	Examiner
Mrs Yevgenya PASHAYAN-LEROY	Dr. of Physics Besançon, UFBC	Examiner
Mr Aram PAPOYAN	Professor Ashtarak, IPR – NAS	Examiner Président du Jury

Laboratoire Interdisciplinaire Carnot de Bourgogne – UMR CNRS 6303, Université Bourgogne Franche-Comté, 9 Avenue A. Savary 21078 Dijon, France

Institute for Physical Research – National Academy of Sciences of Armenia, 0203 Ashtarak-2, Armenia

Contents

Acknowledgements

I would like to express my deepest appreciation to all those who provided me the possibility to complete this thesis. Foremost, I would like to express my sincere gratitude to my supervisors Prof. Claude Leroy and Prof. David Sarkisyan for their continuous support, for their patience, motivation, enthusiasm, and immense knowledge. Their guidance have been invaluable over the past few years.

Besides my supervisors, I would like to thank the rest of the academic staff of the Institute for Physical Research of National Academy of Sciences of Armenia, Ashtarak and Laboratoire Interdisciplinaire Carnot de Bourgogne of Université Bourgogne - Franche - Comté, Dijon I had the pleasure to work with during these last years with special references to Dr. Armen-Sargsyan who was always very demanding and supportive in any matter and Dr. Yevgenya Pashayan-Leroy for her encouragement and insightful comments.

I acknowledge the support of the French Embassy in Armenia for my Bourse du Gouvernement Français, to Armenian General Benevolent Union (UGAB France) & Pilipossian and Pilossian foundation in Geneva, to Agence universitaire de la Francophonie and State Committee of Science of Republic of Armenia, to Armenian National Science & Education Fund, the Ecole Doctorale Carnot-Pasteur and the International Associated Laboratory IRMAS. as well as to Foundation for Armenian Science and Technology.

Finally, I wish to thank my family for their support and encouragement throughout my study, especially to my deceased father Hovik, to my mother Azniv, to my sisters Hasmik and Armine, to my husband Emmanuel and to our son Jean.


UBFC
UNIVERSITÉ
BOURGOGNE FRANCHE-COMTÉ


cnrs
advancing the frontiers


icb
Laboratoire Interdisciplinaire
Carnot de Bourgogne


uB
UNIVERSITÉ DE BOURGOGNE


ECOLE DOCTORALE
CARNOT - PASTEUR


IRMAS
INTERNATIONAL
ASSOCIATED
LABORATORY


IPR


A.N.S.E.F.


AUF
Agence
UNIVERSITAIRE
DE LA FRANCOPHONIE


State Committee
of Science RA


FONDATION
PHILIPPOSSIAN
& PILOSSIAN
UGAB
L'UNION GÉNÉRALE ARMÉNIENNE DE BIENFAISANCE
PARIS


FAST
DISCOVERING
THE FUTURE


Liberté • Égalité • Fraternité
RÉPUBLIQUE FRANÇAISE
MINISTÈRE
DE L'EUROPE ET DES
AFFAIRES ÉTRANGÈRES
La France en Arménie
Ambassade de France à Erevan

Chapter 1

Introduction

Contents

Introduction

Over the past three decades, a significant progress has been made in the development of continuous narrow-band smoothly tunable (tuning range of about 10 - 100 GHz) diode lasers with a spectral linewidth of $\gamma_L/2\pi \approx 1$ MHz and powers ranging from 1 to 100 mW. The presence of such lasers (which are inexpensive and available) in the near infrared region of the spectrum (700 - 900 nm) led to a rapid growth of research in the field of ultra-high-resolution spectroscopy in atomic media. The alkali metal atoms (rubidium (Rb), cesium (Cs), potassium (K) and sodium (Na)) have only one single valence electron in the external shell and strong atomic transitions in the near infrared region. A large number of optical and magneto-optical processes are implemented via the interaction of narrow-band laser radiation with atomic vapors of Rb, Cs, K and Na, which are widely used in laser technology, high frequency resolution metrology, in the creation of highly sensitive magnetometers, in the problems of quantum communication, recording optical information, etc [1–7]. Therefore the interest in these studies is very high.

For these purposes centimeter-long glass cells filled with thermal atomic vapors of alkali metal atoms were used. They have been used in atomic physics to study optical and magneto-optical processes in a different range of experiments. Compared with the setup used for the experiments with cold-atoms, the thermal vapor experiments have the advantage of being relatively cheap and simple in realization. From the experimental point of view the main advantage of using thermal vapor stems arises from the relation between the temperature of a dilute vapor and the density of atoms.

For numerous applications, it is important to reduce the dimensions of the cell containing atomic vapor [7]. In the pioneering experimental works [8–12] it was experimentally proved that the interaction of resonant laser radiation with atoms in a thin film of alkali vapor with thickness $L = 10 - 1000$ μm (so called micro-cells) may underlie a novel method for sub-Doppler spectroscopy, as was earlier theoretically predicted in [13, 14]. A distinctive feature of thin vapor films is that the duration of the interaction of the atom with the laser radiation, which is

determined by the trajectories from wall to wall, is anisotropic.

The contribution of atoms flying almost parallel to the cell windows significantly increases in the registered response signal due to their longer interaction time with the laser field: $t_D = D/v$ (D is the diameter of the laser beam, v is the atomic thermal speed), whereas for atoms flying along the beam, the interaction time $t_L = L/v$ (L is the distance between the inner surfaces of the windows of the micro-cell) is shorter, since $D \ll L$. Particularly, under special experimental conditions in thin atomic vapor column, the so-called velocity selective optical pumping / saturation (VSOP) sub-Doppler resonance peaks of reduced absorption appear in transmission spectra at the exact positions of atomic resonances. Obviously, the atoms flying nearly parallel to the cell window contribute in the formation of the VSOP resonances, by making the VSOP resonances insensitive to the Doppler shift.

Further strong progress in the field of atomic laser spectroscopy was caused by recently developed so-called nano-cells (NC), that are extremely thin cells of sub-micron thickness L of vapor of atomic alkali metals. Cells having a nano-metric thickness in the propagation direction of the laser radiation, have proven to be an excellent spectroscopic tool, allowing one to study even more pronounced peculiarities of resonant absorption, reflection, fluorescence as well as magneto-optical processes for the case when the thickness L is of the order or less than the resonant optical radiation wavelength λ [15–33]. The use of nano-cells filled with Rb, Cs and K vapors and use of the new techniques of formation of narrow atomic transitions (which are described below) allow us further exploration of the atomic transitions of Rb, Cs and K in a much wider range of magnetic field values, than was performed previously, using a compact laboratory device.

Note that the contrast of VSOP resonances recorded with the use of nano-cell thickness $L = \lambda$ is very good and is better than that obtained with the use of micro-cells. The VSOP parameters are shown to be immune against 10% thickness deviation from $L = \lambda$, which makes the λ-method feasible. A laser intensity of 100 mW/cm^2 is enough to form a VSOP resonance with the linewidth of 10 to 30 MHz. In addition, several new striking features were revealed in

the nano-cell spectra, which are absent in those of micro-cells [34–37].

The results of experimental absorption and resonance fluorescence spectra from the nano-cells show that the main parameter determining the nature of interaction is not the thickness L itself, but the ratio L/λ. In particular, it has been revealed that for a low pump intensity (< 1 mW/cm^2), the linewidth of the absorption spectrum exhibits oscillating behavior, and has minimum value when $L = (2m + 1)\lambda/2$ (m is an integer). The most narrow linewidth of the absorption spectrum is achieved when $L = \lambda/2$, and is $3 - 4$ times less than the Doppler linewidth of the absorption spectrum obtained in ordinary centimeter long cells. In contrast, the maximum value of the absorption linewidth is achieved when $L = m\lambda$ and is close to the linewidth of the absorption spectrum from the ordinary cm-size cells [11]. This effect is known as "collapse and revival of Dicke-type coherent narrowing" effect (CDN) [10–16], which was known earlier for microwave domain. Also, the oscillating behavior of the absorption magnitude depending on the ratio of L/λ was demonstrated. The CDN signature has been observed for the nano-cell thicknesses up to $L = 7/2\lambda$ [16, 38].

External magnetic filed strength can vary in the range of 10 G to 9 kG. Among a number of obtained results we would like to stress two of them by using a new method which is described below: 1) Study of the regime of complete decoupling of the bond between the electronic and nuclear moments of the potassium atoms ^{39}K and the cesium atoms ^{133}Cs (so called hyperfine Paschen-Back regime, HPB). 2) Study of the transitions between the excited and ground levels of the hyperfine structure of the ^{39}K D_2 atomic line in an external magnetic field of 300 - 1000 G have been studied for the first time with the use of the nano-cell and circularly polarized radiation. Selection rules forbid these transitions in zero magnetic field. At the same time, the probabilities of these transitions in a magnetic field increase significantly; for this reason, we refer to these transitions as magnetically induced transitions. Developed theoretical model well described the experimental results. Similar results can be reached only by means of much more complex techniques of atomic beams if NC is not used.

This thesis is dedicated to the formation of narrow optical resonances, for which a state

of the art is presented in chapter 1. This thesis aims at implementing new techniques based on optical vapor nano-cells (section 1.2) and their applications in the investigation of alkali D line spectra in a magnetic field and atom-surface interactions. For this purpose a theoretical model describing the resonant interaction of the laser light with the thin alkali vapor layer in the presence of an external static magnetic field is presented in chapter 2. In chapter 3, we perform experimental studies on the Faraday rotation effect from a nano-cell. At last, in chapter 4, we present two new methods based on a derivation processing of recorded spectra which allows the achievement of a stronger line narrowing than that obtained with the transmission spectrum from a NC. The first one is a modification of the Faraday rotation method from a nano-cell, where the analyzer is slightly rotated away from the crossed position (by about 0.1 rad). In this case, a dispersion spectrum is registered at the analyzer output and is processed by first order derivation. The second method consists of second order derivation processing of the raw transmission spectrum recorded from a nano-cell.

The results presented in this thesis have been published as 12 research articles in peer reviewed journals and have been disseminated at 13 international conferences:

Conferences

- A. Amiryan, A. Sargsyan, Y. Pashayan-Leroy, C. Leroy, D. Sarkisyan. *Investigation of Faraday Rotation effect in Cs nano-layers*, Conference Laser Physics (Ashtarak, Armenia, 2018).

- A. Amiryan, A. Sargsyan, Y. Pashayan-Leroy, C. Leroy, D. Sarkisyan. *Sub-Doppler spectroscopy of the Faraday Rotation effect occurring in nano-layers of alkaline atoms*, 50^{th} Conference of the European Group for Atomic Systems (EGAS) (Krakow, Poland, 2018), Conference Laser Physics (Ashtarak, Armenia, 2018).

- A. Amiryan, A. Sargsyan, C. Leroy, D. Sarkisyan. *Investigation of Faraday Rotation effect*

using pressure-controlled thickness nano-cell, 6^{th} International Symposium on Optics and its Applications (Trento-Povo, Italy, 2018).

- A. Amiryan, A. Sargsyan, C. Leroy, D. Sarkisyan. *Faraday Rotation for Rb D_1 line atomic transitions using a nanocell: modification of Faraday Rotation method*, Conference Laser Physics (Ashtarak, Armenia 2017).

- A. Amiryan, A. Sargsyan, E. Klinger, S. Cartaleva, C. Leroy, D. Sarkisyan. *Resonant Faraday rotation effect in Rb atoms with the use of a nano-cell:impact of cell thicknesses on observed spectra*, 49^{th} Conference of the European Group for Atomic Systems (EGAS) (Durham, UK, 2017).

- A. Amiryan, A. Sargsyan, E. Klinger, S. Cartaleva, C. Leroy, D. Sarkisyan. *Linear Faraday Rotation for Rb D_1 line atomic transitions using a nanometric-thin cell*, XXXIX Max Born Symposium: 5^{th} International Symposium on Optics and its applications (OPTICS-2017) (Wroclaw, Poland, 2017).

- A. Amiryan, E. Klinger, A. Sargsyan, D. Sarkisyan, L. Margalit, A. Wilson-Gordon, Y. Pashayan-Leroy, C. Leroy. *"Experimental and theoretical studies of three different EIT-type resonances formed in a nanocell containing ^{87}Rb vapor"*, 48^{th} Conference of the European Group for Atomic Systems (EGAS – ECAMP) (Frankfurt, Germany, 2016).

- A. Amiryan, A. Sargsyan, Y. Pashayan-Leroy, C. Leroy, D. Sarkisyan. *Investigation of Electromagnetically Induced Transparency effect in potassium vapor using a nanometric-thin cell*, 4^{th} International Symposium "Optics and its Applications". (OPTICS–2016) (Yerevan - Ashtarak, Armenia, 2016).

- Amiryan A., Hakhumyan G., Sargsyan A., Pashayan-Leroy Y., Leroy C., Sarkisyan D. *"Selective Reflection on Rb D_2 Line Using Cell with the Thickness of Order of Light Wavelength"*, 25^{th} Annual International Laser Physics Workshop (Yerevan, Armenia, 2016).

- Amiryan A., Sargsyan A., Hakhumyan G., Pashayan-Leroy Y., Leroy C., Sarkisyan D. *"Peculiarities of Cs atomic transition behavior in strong transverse magnetic fields"*, Conference Laser Physics (Ashtarak, Armenia, 2015).

- Amiryan A., Sargsyan A., Tonoyan A., Pashayan-Leroy Y., Leroy C., Sarkisyan D. *"Peculiarities of Rb atomic transition behavior in strong transverse magnetic fields"*, 3^{rd} International Symposium "Optics and its Applications". (OPTICS - 2015) (Yerevan - Ashtarak, Armenia, 2015).

- Leroy C., Pashayan-Leroy Y., Sargsyan A., Amiryan A., Hakhumyan G., Sarkisyan D. *"Study of Atomic Transitions of Cs D_2 line in Strong Transverse Magnetic Fields by an Optical Half-Wavelength Cell"*, 24^{th} Colloquium on High Resolution Molecular Spectroscopy (Dijon, France, 2015).

- Amiryan A., Sargsyan A., Hakhumyan G., Tonoyan A., Leroy C., Pashayan-Leroy Y., Sarkisyan D. *"Study of Atomic Transitions of Rb D_2 line in Strong Transverse Magnetic Fields by an Optical Half-Wavelength Cell"*, Conferences of atomic and laser physics 47^{th} Conference of the European Group for Atomic Systems (EGAS) (Riga, Latvia, 2015).

Published articles

- [39] A. Sargsyan, R. Mirzoyan, A. Sarkisyan, A. Amiryan, D. Sarkisyan. *Splitting of N-Type optical resonance formed in Λ-system of ^{85}Rb atoms in a strong transverse magnetic field*, J. of Cont. Physics (Arm. Academy of Sciences), **49**(1), pp. 20-27 (2014).

- [40] A. Sargsyan, G. Hakhumyan, A. Amiryan, C. Leroy, D. Sarkisyan. *Cs D_2 atomic transitions in strong transverse magnetic field*, J. of Cont. Physics (Arm. Academy of Sciences), **50**(4), pp. 317-326 (2015).

- [41] A. Sargsyan, G. T. Hakhumyan, A. S. Sarkisyan, A. Amiryan, D. Sarkisyan. *Frequency*

reference for atomic transitions of Rb D_2-line based on the effect of selective reflection, J. of Cont. Physics (Arm. Academy of Sciences), **51**(4), pp. 312-322 (2016).

- [42] A. Sargsyan, A. Amiryan, T. A. Vartanyan, D. Sarkisyan. *Studying the regime of complete decoupling of the bond between the electron and nuclear moments at the D_1-line of the ^{39}K isotope using a spectroscopic microcell* Opt. Spectrosc., **121**(6), pp. 790-797 (2016).

- [43] A. D. Sargsyan, A. O. Amiryan, C. Leroy, T. A. Vartanyan, P. A. Petrov, D. A. Sarkisyan. *Extreme increase in atomic transition probability of the Cs D_2 line in strong magnetic fields under selective reflection*, Sov. J. Opt. Technol., **83**(11), pp. 654-658 (2016).

- [44] A. Sargsyan, A. O. Amiryan, C. Leroy, T. Vartanyan, D. Sarkisyan. *The effect of electromagnetically induced transparency in a potassium nanocell*, Opt. Spectrosc., **123**(1), pp. 139-145 (2017).

- [45] A. Sargsyan, A. Amiryan, S. Cartaleva, D. Sarkisyan. *Nanocell with a pressure-controlled Rb atomic vapor column thickness: Critical influence of the thickness on optical processes*, JETP, **125**(1), pp. 43-49 (2017).

- [46] A. O. Amiryan, *Theoretical investigation of Faraday rotation effect in atomic alkali nano-layers*, J. of Cont. Physics (Arm. Academy of Sciences), **53**(3), pp. 212-221 (2018).

- [47] A. Amiryan, A. Sargsyan, Y. Pashayan-Leroy, C. Leroy, D. Sarkisyan. *Faraday rotation in cesium nano-layers in strong magnetic fields*, J. of Mod. Opt., **66**(3), pp. 328-334 (2018).

- [48] A. Sargsyan, A. Tonoyan, G. Hakhumyan, A. Amiryan, P. Todorov, S. Cartaleva, D Sarkisyan. *Modified Faraday rotation method for studying cesium atomic lines in strong magnetic fields*, J. of Cont. Physics (Arm. Academy of Sciences), 54(1), pp. 84-96 (2019).

- [49] A. Sargsyan, A. Amiryan, T. A. Vartanyan, D. Sarkisyan. *A modified method of Faraday rotation for investigation of atomic lines of rubidium and potassium in ultrathin cells*, Opt. Spectrosc., **126** (3), pp. 173-180 (2019).

- [50] A. Sargsyan, A. Amiryan, D. Sarkisyan. *Faraday effect in rubidium atomic layers thinner than 100 nm*, JETP, **128**(3), pp. 341-346 (2019).

Unpublished articles

- A. Sargsyan, A. Amiryan, Y. Pashayan-Leroy, C. Leroy, A. Papoyan and D. Sarkisyan. *Resolution-enhanced quantitative spectroscopy of atomic vapor in optical nano-cells based on second-derivative processing of spectra*, arXiv:1906.06252, (2019).

1.1 Formation of sub-Doppler optical resonances

1.1.1 Saturated absorption spectroscopy

The saturated absorption of the medium in the field of counter-propagating waves, which leads to a Lamb dip in the center of the absorption line, is one of the methods to form sub-Doppler spectroscopy [51]. The radiation of cw extended cavity diode laser is split into two parts: a strong pump beam (intensity is of the order of a few mW/cm^2) and a weak (weak enough to neglect its influence on populations) probe beam (with an intensity of order of several μ W/ cm^2) which overlap in the cell containing atomic vapor as two counter propagating beams as depicted in Fig. 1.1. In the experiment, the probe beam transmission as function of the laser frequency ω is usually recorded. The apparatus consists of a Extended Cavity Diode Laser (ECDL) emitting radiation with the wavelength of 780 nm and the linewidth of 1 MHz which forms both the pump and probe beams. The pump power is about 0.9 mW and probe power is about 1 μW. The main difference between the experimental setup in Fig. 1.1 and of that presented in Fig. 5 in [52] is

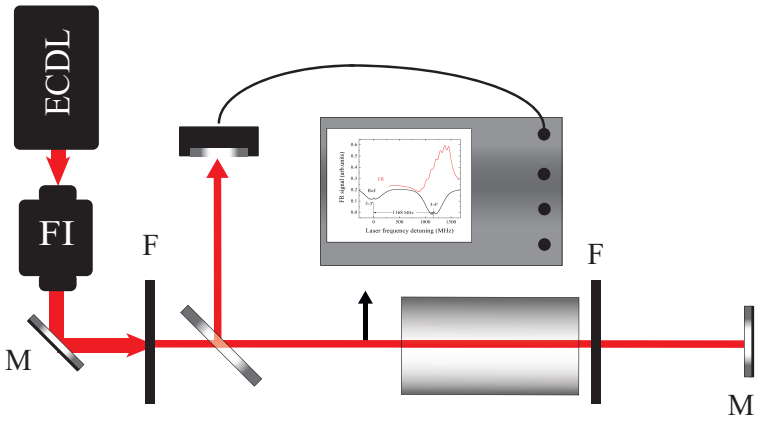

Figure 1.1: Schematic diagram of the experiment for observing the sub-Doppler spectra of atoms by the method of saturated absorption spectroscopy. ECDL - extended cavity diode laser; FI - Faraday isolator; M - mirror; F - filters. The probe beam is formed by the reflection from the mirror, which after passaging through a rubidium vapor cell (room temperature) is sent into a photodiode PD.

that the pump and probe beams crossing angle φ is zero in our case. It is well known that with the increase of the crossing angle φ, the increase of the resonance linewidth takes place [51].

The scheme of the experimental setup that was used in [52] is presented in Fig. 1.2. It consists of an ECDL emitting radiation with the wavelength of 780 nm and the linewidth ≈ 1 MHz which forms the pump and probe beams. Counter propagating pump and probe beams overlap in a 50 mm long vapor cell with a less than 10 mrad crossing angle φ. The cell contains ^{85}Rb and ^{87}Rb in their natural abundances at room temperature. In this apparatus the pump and probe have parallel polarizations. Neutral density filters F were used to attenuate the pump and the probe powers independently. The probe beam was focused onto a photodiode circuit that recorded a voltage linearly proportional to the incident intensity. The pump power is of 0.9 mW and probe power is of 500 nW.

Rubidium D_2 line $F_g = 3 \rightarrow F_e = 2, 3, 4$ (hereafter we will use a simplified notation $3 \rightarrow 2', 3', 4'$), hyperfine transitions, with frequency splittings between the hyperfine energy levels and relative probabilities is presented in Fig. 1.3. The probabilities are normalized to the probability of the strongest transition in the group. The experimental absorption spectrum of the $3 \rightarrow 2', 3', 4'$ transitions obtained by our group is shown in Fig. 1.4a

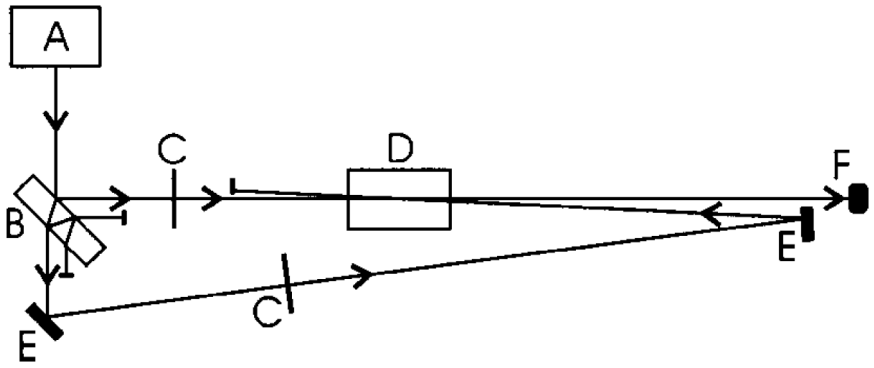

Figure 1.2: Sketch of the experimental setup for realization of saturation absorption technique used in [52]. Laser light is derived from an ECDL (A) and split using a thick glass slide (B) into a probe beam (reflected) and pump beam (transmitted). The probe beam is allowed to pass through a room temperature rubidium vapor cell (D) onto a photodiode (F). Mirrors (E) direct the counter propagating pump beam through the cell. Attenuators (C) are used to vary the power of the pump and probe independently.

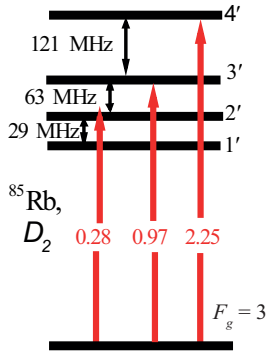

Figure 1.3: Energy level diagram for the ^{85}Rb D_2 line $3 \rightarrow 2', 3', 4'$ transitions. The transition probabilities are normalized to the probability of the strongest transition in the group.

As it was expected [51], six sub-Doppler features, each of them having a linewidth almost equal to the natural linewidth, are observed at low pump intensity, *i.e.* three velocity selective optical pumping (VSOP) resonances located at the transitions $3 \rightarrow 2', 3', 4'$ and three crossover (CO) resonances located between the VSOP resonances are observed. The left CO resonance is located between the VSOP resonances formed by the absorption at the transitions $3 \rightarrow 2'$ and $3 \rightarrow 3'$, the middle CO resonance is located between the VSOP resonances formed by absorption at the transitions $3 \rightarrow 2'$ and $3 \rightarrow 4'$ and the right CO resonance (the strongest) is located between the VSOP resonances formed by absorption at the transitions $3 \rightarrow 3'$ and $3 \rightarrow 4'$.

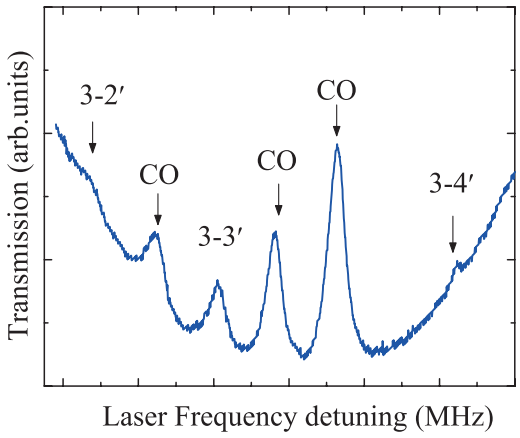

(a)

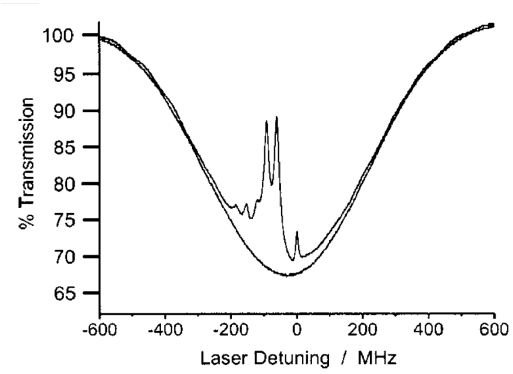

(b)

Figure 1.4: Experimental transmission spectra of the ^{85}Rb D_2 line $3 \rightarrow 2', 3', 4'$ transitions. a) The experimental saturation absorption formed with the experimental setup presented in Fig. 1.2, Rb cell with $L = 50$ mm, at room temperature, b) ^{85}Rb D_2 line $3 \rightarrow 2', 3', 4'$ transitions when cell $L = 50$ mm and the experimental setup presented in Fig. 1.3, from the work of [52] is used.

The absorption spectrum on ^{85}Rb D_2 line, for hyperfine transitions $3 \rightarrow 2', 3', 4'$ obtained with the experimental setup presented in Fig. 1.2 is shown in Fig. 1.4b . As in the case presented in Fig. 1.4a, here also three VSOP resonances located on the hyperfine transitions and three CO resonances located between the VSOP resonances are recorded. The main difference in resolution between the Fig. 1.4a and Fig. 1.4b arises from the crossing angle φ. In Fig. 1.4a $\varphi = 0$ leading to the to the crossover resonances being completely resolved, while in Fig. 1.4b ($\varphi \neq 0$) the two largest crossovers are partially overlapped.

1.1.2 Narrow-band *N*-resonance formation in rubidium thin atomic layers

An alternative process where a narrow-band optical resonance is formed (called below for brevity N-resonance) has been described for the first time in [53]. The theoretical model describing the N-resonance formation mechanism also has been developed in [53], however we would like to give a comparison and qualitatively explain the N-resonance formation, as it was

presented by our group in [39]. The main advantages of N-resonance are the high contrast and narrow (sub-natural) spectral width, even in case of employment of optical cells of micro-meter thickness containing rubidium atomic vapor.

Diagram of the experimental arrangement is demonstrated in Fig. 1.5. We used radiations

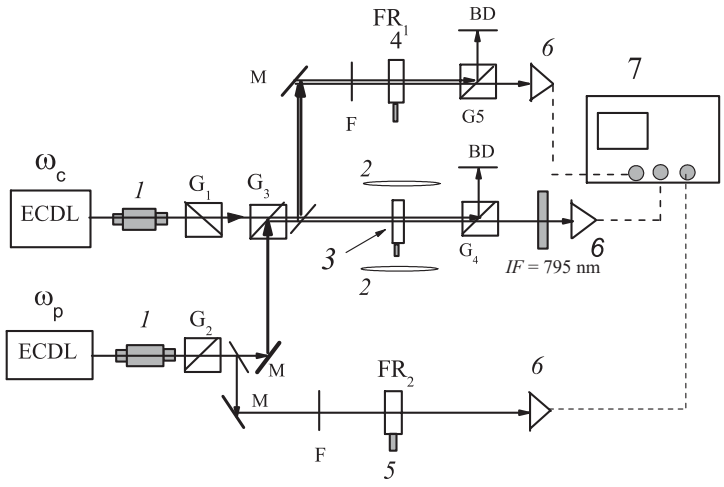

Figure 1.5: Diagram of experimental arrangement (see text for details).

from two cw narrow-band ($\Delta\nu_L$ <1MHz) ECDL, a coupling radiation (at fixed frequency) ν_c and probe radiation (at smoothly tunable frequency) ν_p. With two Glan prisms, G_1 and G_2, polarizations of coupling and probe lasers were made linear and mutually orthogonal. Both radiations of diameters 2 mm were superimposed by the Glan prism G_3 and focused by the lens (F = 20 cm) into the micro-cell (3) with the thickness of about 40 μm, and then collimated by the second lens (the lenses are not shown in Fig. 1.5). A part of the probe and coupling radiations were sent into an additional thin Rb-cell (4) containing buffer gas (thickness L = 0.1 mm) for formation of the N-resonance at zero magnetic field (frequency reference FR_1). Besides, a part of probe radiation was directed into a nano-cell (5) with the thickness of Rb-vapor column $L = \lambda$, (λ is the resonant wavelength) which provides the frequency reference FR_2 [54]. Recording of radiations was performed by photodiodes FD-24 K (6). Signals from photodiodes were amplified by operational amplifier and fed to four-beam digital storage oscilloscope Tektronix TDS2014B (7). For producing weak transverse magnetic fields (in this case the direction of the magnetic

field is perpendicular to the direction of the laser radiation, *i.e.* $\mathbf{B} \perp \mathbf{k}$ with $\mathbf{k}$ the wave vector of laser radiation), we used a pair of wound coils (2) inside which the micro-cell (3) was placed. For producing strong transverse magnetic fields, we used two ring permanent magnets (2) with a diameter of 60 mm and a thickness of about 30 mm. Permanent magnets were mounted on two non-magnetic tables (micro-cell (3) was placed between them) with possibility of smooth variation of the distance between them. Magnetic field in the micro-cell increases with the decrease of this distance.

With the help of prisms G_4 and G_5 the radiation of coupling laser was cut and only the probe radiation was recorded. For better selection of the probe radiation frequency, we used additionally an interference filter (IF = 795 nm) with following parameters: 50% transmission at the wavelength 795 nm and a bandwidth of 10 nm. Beam dumpers (BD) were used for blocking residual radiation of coupling laser. Temperature of the side-arm of micro-cell (which determines the density of rubidium atoms in the cell) was about 100 °C (density of rubidium atom vapor is nearly of 5 $\times 10^{12}$ atoms cm^{-3}).

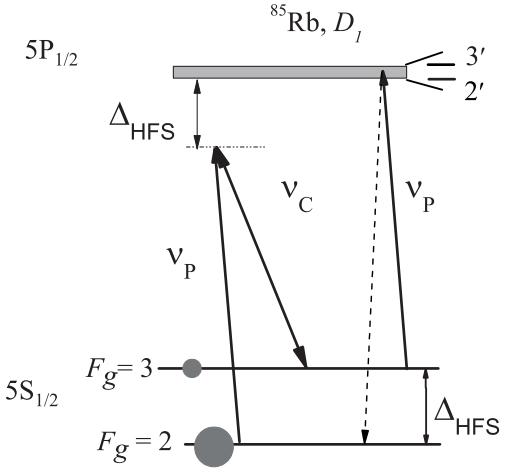

Figure 1.6: Illustration of the N-resonance formation on the Λ-system of ^{85}Rb, D_1 line. The frequencies satisfy to the condition $\nu_P - \nu_C = \Delta_{HFS}$. The probe radiation is in resonance with the transition $5S_{1/2}, F_g = 3 \rightarrow 5P_{1/2}$. This configuration produces the transfer of atoms from the level $F_g = 3$ (shown by a small circle) to the level $F_g = 2$ (shown by a big circle).

Figures 1.6 and 1.7 show the schemes of formation of N-resonance in a Λ-system of ^{85}Rb atoms, D_1 line, where the lower levels of the Λ-system are $F_g = 2, 3$, while two Doppler-broadened

hyperfine levels $5P_{1/2}$, $F_e = 2', 3'$, constitute the upper level. In Fig. 1.6 the probe radiation ν_P transfers atoms from the ground level $5S_{1/2}$, $F_g = 3$ to the excited level $5P_{1/2}$ with subsequent decay into the state $F_g = 2$. This is the well known optical pumping process [54]: due to the

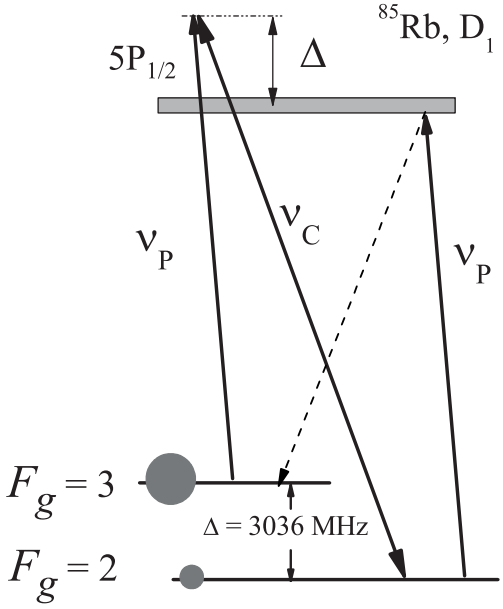

Figure 1.7: Illustration of the N-resonance formation on the Λ-system of ^{85}Rb, D_1 line. The frequencies satisfy to the condition $\nu_P - \nu_C = \Delta_{HFS}$. The probe radiation is in resonance with the transition $5S_{1/2}, F_g = 2 \rightarrow 5P_{1/2}$. This configuration produces the transfer of atoms from the level $F_g = 2$ (shown by a small circle) to the level $F_g = 3$ (shown by a big circle).

optical pumping process the level $F_g = 3$ is depleted (the population is schematically indicated by the small circle), while the population of the $F_g = 2$ level is increased (the population is schematically indicated by the large circle). As a result, the population inversion $N_2 > N_3$ appears and two-photon absorption occurs at a certain coupling laser frequency. In the case of the configuration presented in Fig. 1.7 the atom from the level $F_g = 2$ absorbs the probe radiation photon at frequency ν_P, emits a photon at frequency ν_C, and is transferred to the level $F_g = 3$. Note, that the condition $\nu_P - \nu_C = \Delta_{HFS}$ must be fulfilled. This results in the formation of a narrow N-resonance, which exhibits as an enhanced absorption in the probe radiation spectrum. This process could be considered also as a Raman-type process between the levels $F_g = 2 \rightarrow F_g = 3$. Note, that if $N_2 - N_3 = 0$ (this is true in the absence of the probe radiation) no N-resonance occurs.

This mechanism of N-resonance formation is also supported by the substantial improvement of the contrast when a buffer gas is used. This is explained as follows: it is known that the lower levels of a Λ- system are weakly broadened when the buffer gas in the pressure range 10 - 100 Torr is applied [54] (in the case of Rb atoms and the Ne gas, the collisional cross section between the levels $F_g = 2$ and 3 is about 10^{-22} cm^2). The buffer gas increases the interaction time t with the laser beam $t = D/v$, where D is the diameter of the laser beam and v is the atom thermal velocity, since the atom velocity in the presence of a buffer gas is several orders of magnitude less than the atomic thermal velocity in pure Rb vapor. When the condition $\nu_P - \nu_C = \Delta_{HFS}$ takes place, the optical pumping efficiency is proportional to the interaction time t [19].

When the probe radiation is in resonance with the transition $5S_{1/2},\ F_g = 2 \rightarrow 5P_{1/2}$, the depletion of the population from the level $F_g = 2$ and an increase in the population of the level $F_g = 3$ (see Fig. 1.7)) occur, resulting in in two-photon absorption at frequency ν_P (this process is indicated by dashed lines in Fig. 1.7) and to the transfer of atoms from the level $F_g = 2$ to the level $F_g = 3$.

Construction of the micro-cell filled with the Rb vapor

We used in the experiment a micro-cell with the thickness $L \approx 40\mu$m, filled with rubidium vapor with addition of neon buffer gas under a pressure of 100 Torr. The need to introduce the buffer gas in order to obtain higher contrast of N-resonance was mentioned in [55]. 10×20 mm^2 and thickness of 2 mm were fabricated of crystalline sapphire. The C-axis of the crystal was perpendicular to the window surface reducing thus essentially birefringence of transmitted radiation. Surfaces of sapphire windows were carefully polished (local roughness is less than 5 nm). For formation of a fixed gap (between inner surfaces of windows), in lower and upper parts between the windows platinum strips were placed with sizes 1×1 mm^2 and thickness 40 μm. The micro-cell was filled with natural rubidium consisting of ^{85}Rb (72%) and ^{87}Rb (28%). Usage of micro-cell allows, in particular, employing permanent magnets for producing strong magnetic fields in the atomic vapor enclosed in the micro-cell. A drawback of employment of permanent

magnets is high inhomogeneity (gradient) of the produced magnetic field. However, if we use a micro-cell, the change in the magnetic field value (in case of applying longitudinal magnetic field) within the thickness of vapor column is considerably smaller than this value. In case of applying transverse magnetic field, the diameter of laser radiation should be small (for reducing the magnetic field gradient in transverse direction); in our case it was 100 μm.

Experimental Results

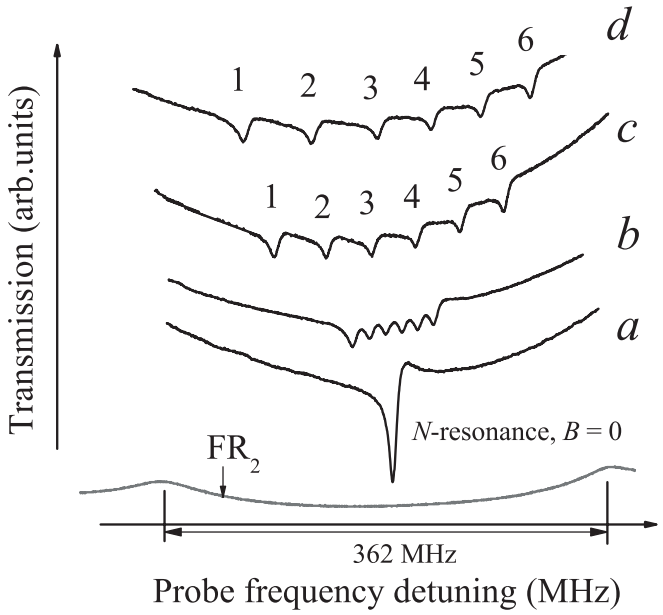

Figure 1.8: Transmission spectra (a, b, c, d) of probe radiation at B = 0, 14, 40, and 50 G, respectively (spectra are vertically shifted for convenience). The $L = 40\mu$m cell was filled with Rb and Ne. The onfiguration of couple and probe beams is shown in Fig. 1.6. The lowest curve is frequency reference FR_2 obtained by means of Rb nano-cell.

Figure 1.8 demonstrates transmission spectra of the probe radiation (for configuration of frequencies of coupling and probe lasers shown in Fig. 1.6 at magnetic field values B =0, 14, 40, and 50 G, for curves a, b, c, and d, respectively. Curve a (frequency reference FR_1) is the spectrum of N-resonance recorded at zero magnetic field. The FWHM is about 6 MHz, which is close to the natural linewidth of Rb atoms $\gamma_N/2\pi = 6$ MHz. The asymmetric shape of the N-resonance is caused by the presence of the buffer gas in the cell. The splitting of N-resonance arises due to the presence of the external magnetic field. Numbers 1-6 mark new components

arising due to the presence of the external magnetic field. For curve d the frequency distance between the components 1 and 6 is equal to $5 \times 0.93 MHz/G \times 50$ G $= 233$ MHz. Figure 1.9

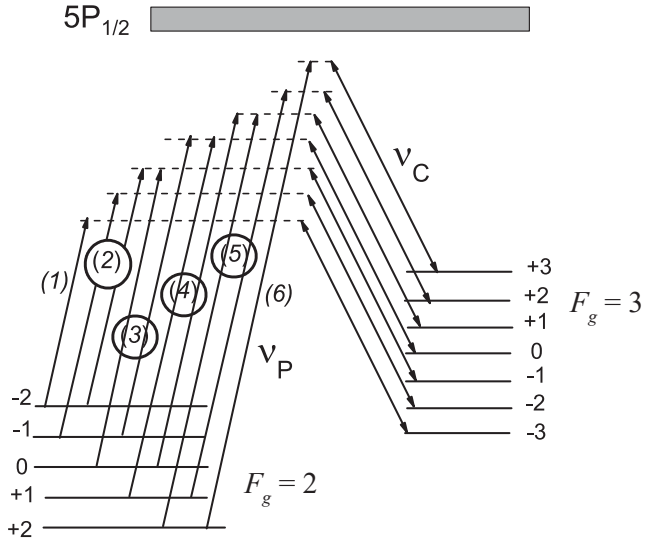

Figure 1.9: Diagram of levels $F_g = 2$ and $F_g = 3$ of the ^{85}Rb atoms which are split in the external field into, respectively, 5 and 7 sublevels. Ten of possible pairs of frequencies of coupling and probe lasers are shown. Pairs, for which the frequencies of probe laser are the same, are enclosed in the circles; the components (1) and (6) contain one transition each.

shows the diagram of energy levels $F_g = 2$ and $F_g = 3$ of the ^{85}Rb atoms which are split in the external field into 5 and 7 sublevels, respectively. The diagram shows ten possible pairs of frequencies of coupling and probe lasers, which can lead to two-photon absorption from lower level $F_g = 2$ with transfer of atoms to the level $F_g = 3$. For the pairs, for which the frequencies of the probe laser are the same, are enclosed in the circles; components (1) and (6) contain only one transition each. Therefore, the diagram in Fig. 1.9 explains the existence of six N-resonance components detected in the transmission spectra from the micro-cell (shown in Fig. 1.8) in the external magnetic field.

1.2 Construction of a nano-cell containing atomic vapors

In a sample of gaseous medium, the individual atoms move in haphazard directions, with an average velocity function of the temperature of the gas. When studying the properties of atoms

using the transmission of the laser through the medium, one records a Voigt profile, which is a convolution of a Lorentz profile with a Gaussian one. Here due to the Doppler broadening, the individual atomic transitions are overlapped and consequently it is not possible to observe these transitions separately.

However, cells having a nano-metric thickness in the propagation direction of the laser radiation, have proven to be an excellent spectroscopic tool, allowing to record atomic transitions having a linewidth four to five times narrower than the Doppler width [15, 16, 24, 38, 56] .

The efficiency of the optical pumping is determined by the expression [19],

$$\eta = \frac{\Omega^2 \gamma_N t}{\left(\Delta + \mathbf{k}\cdot\mathbf{v}\right)^2 + \Gamma^2} \tag{1.1}$$

where Ω is the generalized Rabi frequency, which is directly proportional to the square root of the laser intensity, γ_N is the natural linewidth of an atomic level (for instance 6 MHz for ^{87}Rb)) while Γ is the sum of homogeneous and inhomogeneous broadenings, t is the atom - radiation interaction time, Δ is the detuning from a resonance, $\mathbf{k} = \frac{2\pi}{\lambda}\mathbf{n}$, $\mathbf{n}$ is a unit vector in the propagation direction and $\mathbf{v}$ is the speed of an atom [51].

Equation (1.1) indicates that the efficiency of the process highly depends on the interaction time t. Hereby, in our experiments the interaction time for the atoms flying orthogonally to the laser radiation is $t_D = D/v$, where $D \sim 1$ mm is a diameter of the laser beam and $v \sim 200 - 300$ m/s for alkali atoms in the range of considered temperatures. For the atoms flying along the propagation the interaction time t_L is given by $t_L = L/v$, where L is the distance between the two windows of the NC. Since L is order of a few microns, thus t_D is greater by 3 orders of magnitude than t_L. For the orthogonally flying atoms, $\mathbf{k}\cdot\mathbf{v} = 0$, and Eq. (1.1) takes its maximum value when $\Delta = 0$. This is the reason why the resonances recorded with a use of the NC are exactly located on the atomic transition (no Doppler shift) and these resonances can be used as frequency references. This property will be used to describe the behavior of atomic transitions in strong magnetic fields.

1.2.1 The nano-cell

The construction of an NC with the tapered gap (the thickness of an atomic column varies from 20 nm to several hundreds of micron) is similar to the one demonstrated in Fig. 1.10 and is considered in detail in [15,35,36]. Two rectangular, well polished crystalline sapphire (Al_2O_3) or garnet ($Y_3Al_5O_{12}$) plates *(1)* with the dimensions 20×30 mm^2 and thickness ~ 3 mm have been chosen as cell windows. The choice of these materials comes from their chemical resistance to aggressive alkali metals. The degree of sapphire polishing is required to be very high (less than $\lambda/8$). Since the crystalline sapphire has natural birefringence, the crystal is cut in such a way that the C-axis is perpendicular to the cell windows. A thin strip of titanium or platinum was placed in the bottom part of the cell windows in order to form a nano-metric gap between the windows (see Fig. 1.10a).

In case of particular problems, it was required to use windows having a thickness about

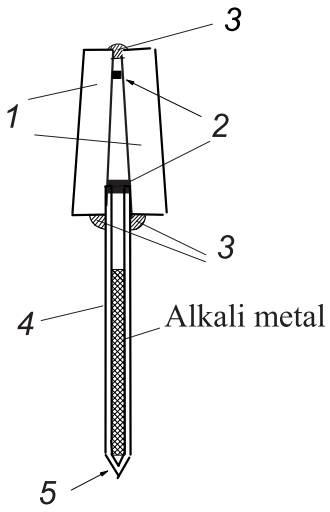

(a)

(b)

Figure 1.10: Scheme and photography of a nano-cell. (a) Description of a nano-cell: 1 - sapphire or garnet plates, 2 - titanium or platinum strips, 3 - glue, 4 - sapphire tube, 5 -glass side-arm. (b) Photograph of a nano-cell containing Cs atomic vapor: L varying in range from 50 nm to 2 μm. One may see the interferometric pattern which is formed by the reflection of visible light from the internal surfaces of the NC.

0.7 mm. In those cases after the cell filling and sealing-off under the pressure of the external atmosphere, the windows were pressed to each other, particularly in the region where the stripe was absent (top of the plates), decreasing the gap between the cell windows up to $20 - 30$ nm. In case when the plates of ~ 0.7 mm were used to increase plates thicknesses in the bottom part, little sapphire or garnet blocks were glued *(3)*, which is well seen in Fig. 1.10b. Inside the thin sapphire, pipe *(4)* with the external diameter ~ 2 mm and ~ 50 mm length was put and glued. For this purpose, a hole was drilled in the bottom side of the cell (where the additional sapphire blocks were glued) with a diameter of ~ 2 mm. Further, all the construction was gathered and glued in the vacuum chamber [57].

It is important to note, that since the distance between the cell windows is small, a more careful and longer pumping (~ 8 hours) at high temperature (~ 400 °C) is necessary. A photograph of the NC with a wage-shape gap between the windows and L in the range 50 nm - 2 μm is given in Fig. 1.10b. It is important to mention, that on this photograph, an interferometric pattern is observed, (see arrow in Fig. 1.10b), which is a result of the reflection of the sunlight from the internal surfaces of the NC windows. Note that the interferometric pattern is observed up to thicknesses 2 – 2,5 μm. A thermocouple is fixed so that its tip *(5)* (see Fig. 1.10a) has a good thermal contact with the upper limit of the metallic alkali column inside the sapphire pipe. It can also be seen in Fig. 1.10b. In order to increase the thermal contact, the tip of the thermocouple is tied to the sapphire pipe by a glass fiber. To prevent the atomic vapor condensation on the cell windows, their temperature is always kept $20 - 30$ °C higher that the one of the side-arm.

1.2.2 Thickness determination

When shining laser radiation normally on the nano-cell, one gets three reflections as demonstrated in Fig. 1.11: R_1 is the reflection from the external surface of the first window; R_2 is the interferometric pattern from the two inner surfaces, it contains information about the thickness

of the cell, and the reflection R_3 is from the outer surface of the second window [58].

These three reflections are spatially resolved since the cell windows are made of wedged sub-

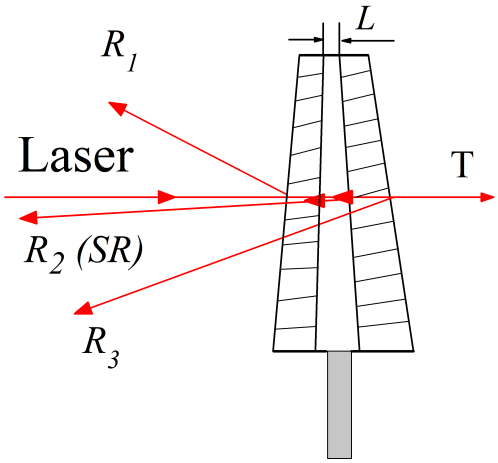

Figure 1.11: Schematic draw of beam reflection from the nano-cell. The beam R_2 contains information about the thickness of the cell.

strates, however the tilt angles are small enough to consider a nano-cell as a low-Q Fabry-Pérot interferometer. Thus measuring the intensity ratio I_{R2}/I_{R1} of reflected beams R_2 and R_1 and using Fabry-Pérot relation one may calculate the cell windows reflection coefficient R and determine the cell thickness L.

$$\frac{I_{R_2}}{I_{R_1}} = \frac{(1-R)^2}{R}\frac{F\sin^2\varphi}{1+F\sin^2\varphi}, \tag{1.2}$$

here $R = [(n-1)/(n+1)]^2$ with $n = 1.8216$ (at $\lambda = 780$ nm), $F = 4R/(1-R)$ is the finesse coefficient and $\varphi = 2\pi L/\lambda$. From Eq. (1.2) follows that when the thickness $L = 2m\lambda/4$ (with m being an integer), a minimum of the reflected radiation (a maximum in the intensity of the transmitted radiation) is achieved, whereas when $L = (2m+1)\lambda/4$, there is a maximum of the reflected radiation (minimum of the intensity of the transmitted radiation).

The plot of intensity ratio versus cell thickness using Eq. (1.2) is presented in Fig. 1.12. The red curve is plotted for laser wavelength $\lambda = 795$ nm (Rb D_1 line) and the blue curve is for $\lambda = 895$ nm (Cs D_1 line). As it is seen the intensity ratio $\frac{I_{R_2}}{I_{R_1}} = 0$ when $L = m\lambda/2$, whereas

the maximum values are achieved when $L = (2m + 1)\lambda/4$. Note that using the aforementioned

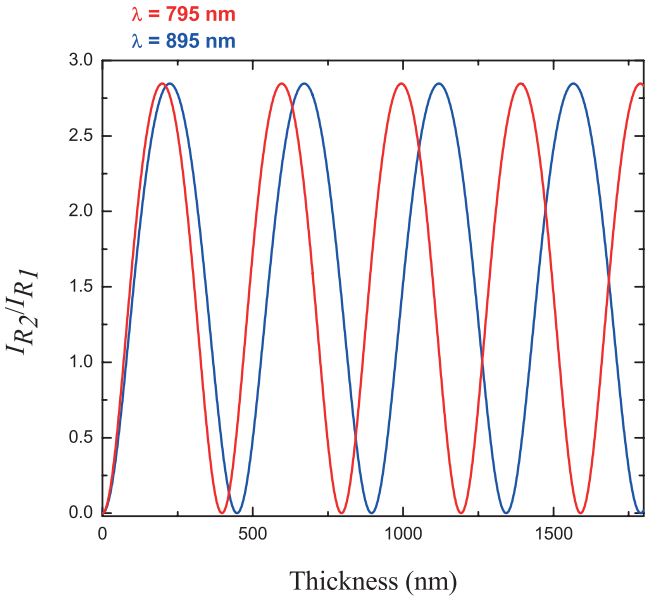

Figure 1.12: Intensity Ratio versus the cell thickness L for laser wavelengths $\lambda = 795$ nm (Rb D_1 line, in red) and $\lambda = 895$ nm (Cs D_1 line, in blue).

method cell thickness measurement uncertainty may arise: due to the periodic modulation of intensity ratio one may determine thickness L up to $\pm m\lambda/2$. Which means that $L = \lambda/2$, $L = \lambda$, *etc.* are indistinguishable in the measurements. In order to solve this problem, we make sure to have a region of $L < 100$ nm while building the nano-cells. This region is easily distinguishable on the photo since the reflection from this layer vanishes (the layer is transparent) and when an optical contact takes place at $L \sim 0$, the reflection is absent. Thus, the use of $L < 100$ nm region as starting point for thickness measurements eliminates the uncertainty. It is important to note, that for some cases the region of homogeneous thickness might be small, in these cases it is important to reduce the beam diameter up to $D_{laser} = 0.3 - 0.5$ mm.

1.2.3 Nano-cell with pressured controlled thickness

As it was mentioned in the previous section the NCs are fabricated with a wedge gap (as a rule, in the vertical direction) between the NC windows [59]. In this case, the required NC thickness (*i.e.*, the required atomic vapor column thickness in NC) was achieved via either

mechanical movement of the NC or spatial translation of the laser beam. In some problems, it is necessary to vary L over wide limits, e.g., in the range 100 - 2000 nm, and mechanical displacements are inconvenient. For this purpose we have constructed a new type of NC that allows to change gradually the atomic column width L over wide limits in a convenient manner. The new type of NC is similar to the one presented here-before except that the thick (2.5 mm) YAG plates were replaced by thin ones (0.5 mm) which makes the NC sensible to the applied pressure. In order to create a nano-metric gap, two thin (2 μm) platinum spacers were placed at the top and bottom part of the NC windows. Before attaching the reservoir it was needed to increase the total length of the cell, for this purpose a thin garnet plate was glued on outer part of each window. The rest of the fabrication details do not differ from the NC presented before. After attaching the reservoir and pumping out the air the residual vacuum in the cell was $\sim 10^{-4}$ Torr. As the windows are thin, the external atmospheric pressure presses them, reducing the

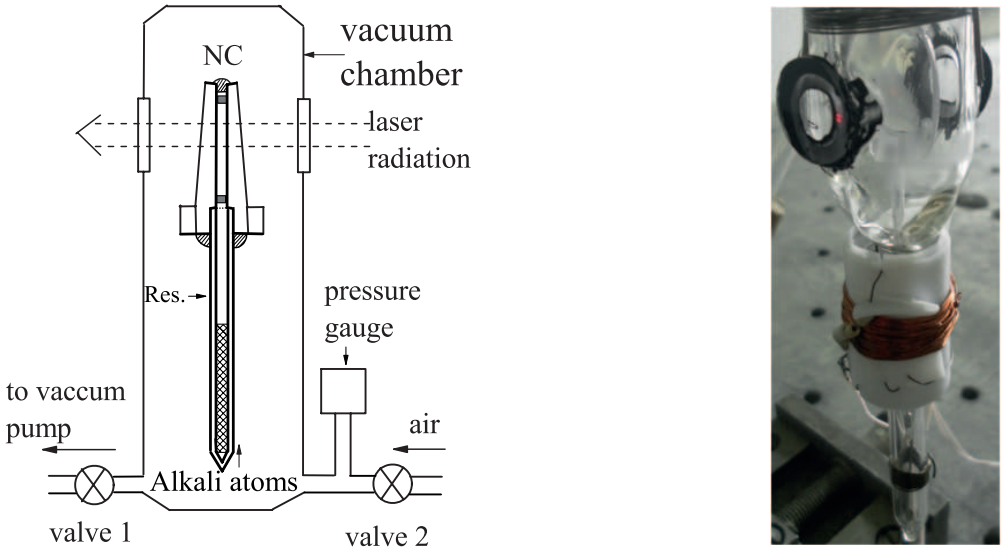

Figure 1.13: Schematic diagram and a photograph of the vacuum chamber. Valve 1 allows one to pump out the air inside the chamber, valve 2 allows one to pump inside the chamber an air with the fixed pressure, which is measured by an usual pressure gauge. (b) Photograph of the glass vacuum chamber with NC (indicated by the arrow) inside.

gap in the central region to 140 nm. Further, the NC was place in a glass vacuum chamber as is presented in Fig. 1.13. The chamber has two outgrowth with two valves, from which valve

1 is used to pump out the air and valve 2 is controlled by pressure gauge and is used to pump in air . When the air is pumped out from the chamber, the NC windows are straighten up and the gap in the central region increases up to 1700 nm. Here thickness control is performed by changing the pump pressure. Controlling the pressure in the chamber with a pressure gauge, we were able to achieve and reproduce the required thickness L. The dependence of thickness L from the inside pressure (at a temperature of 140 °C) is depicted in Fig. 1.14. As one may see, the pressure assisted adjustment of L is 3 nm/Torr in the range]0 - 500] Torr.

As it was mentioned before the new type of NC also behaves like a low-Q Fabry-Pérot

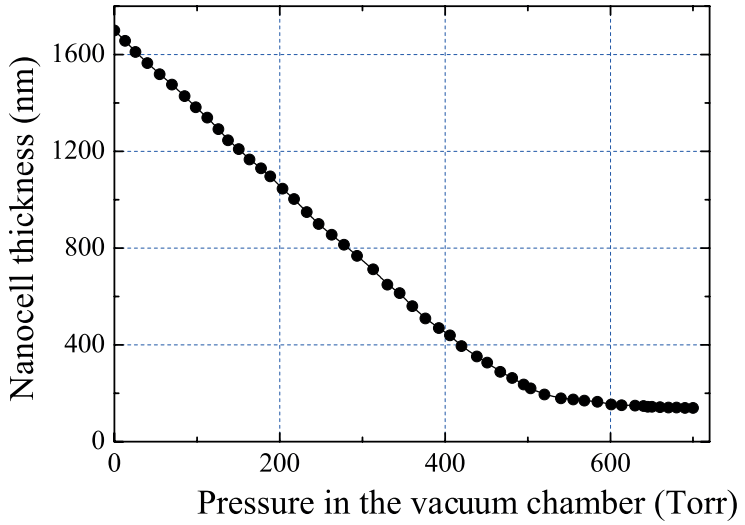

Figure 1.14: Nano-cell thickness versus the pressure of the vacuum chamber. The change of L is 3 nm/Torr in the range]0 - 500] Torr.

etalon, hence, Eq.(1.2) is relevant and may be used.

1.2.4 Atomic number density

Alkali atoms have only one electron in their outermost shell and the charge of the nucleus is shielded by the core electrons. This makes the alkali atoms very chemically reactive due to the relatively low ionization energy of the outermost electron. The vapor pressure P_v (in torr)

of alkali atoms versus temperature T is given by [60–62]:

$$\log P_v = 2.881 + A + B \times T^{-1}, \tag{1.3}$$

the values of A and B for both solid and liquid phases are presented in Table 1.1 [61]. To convert $\log P_v$ from Torr to atmosphere, one should omit the term 2.881. The atomic number density

Atom	Melting point	State	A	B (K)
K	336.65 K	Solid	4.961	-4646
		Liquid	4.402	-4453
Rb	312.45 K	Solid	4.857	-4215
		Liquid	4.312	-4040
Cs	301.59 K	Solid	4.711	-3999
		Liquid	4.165	-3830

Table 1.1: Recommended parameters A and B of Eq.(1.3) and melting point temperature.

N, which is the concentration of atoms or molecules per unit volume can be calculated using Eq. 1.4 [61]

$$N = \frac{133.323 \times P_v}{k_B \times T}, \tag{1.4}$$

The factor 133.323 is used to convert the vapor pressure from Torr to Pa, k_B is the Boltzmann constant and the temperature T to be taken in K. We present in Fig. 1.15 the atomic number density as a function of the temperature calculated using Eq.(1.4), where the temperature was converted in °C. These NC can operate up to 450 °C and provide density of atoms up to $N = 10^{18}$ cm^{-3}.

1.3 Summary

In this chapter, we have presented the review of various sub-Doppler spectroscopic techniques. We have described the construction of nano-cells containing alkali vapors with the thickness varying from 20 nm to several hundreds of nano-meters. The implementation of nano-cells in

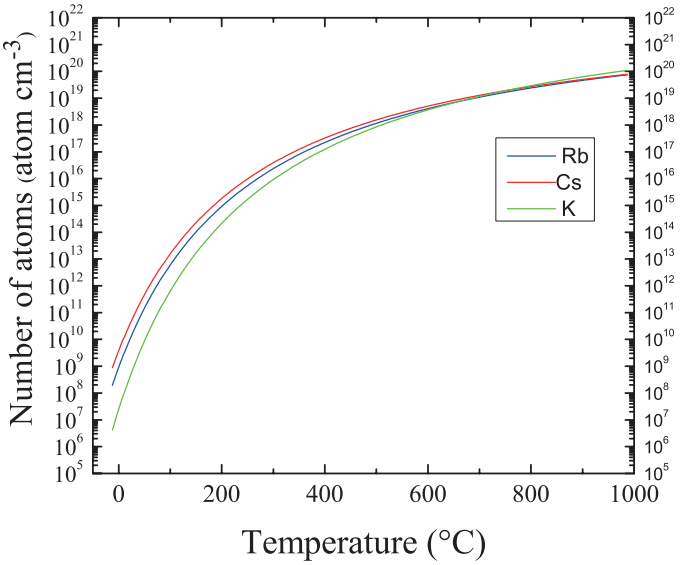

Figure 1.15: Atomic number density N versus temperature for K(in green), Rb (in blue) and Cs (in red) atoms.

the experiments allows the direct obtainment of sub-Doppler spectra without the application of nonlinear techniques. The required nano-cell thickness is achieved via either mechanical displacement of the NC, or spatial translation of the laser beam. Next, we have described a recently developed device allowing to change the atomic vapor thickness precisely and smoothly in the range of $L = 140 - 1700$ nm. This device consists of a NC placed in a vacuum chamber, where the pressure can be varied in the range 0 to 1 atm, and as a result, the NC gap thickness L can be changed in a smooth and reproducible manner.

Note that, unlike the NCs used earlier, the pressure controlled nano-cell has a larger region of homogeneous thickness, which makes it much less sensitive to acoustic vibrations, which is especially important for studying the influence of L on such processes as the van der Waals interaction of atoms with the NC windows. In the last part of this chapter, we have discussed some physical properties of atomic alkali vapors that will be useful for the discussion in the upcoming chapters.

Chapter 2

Spectroscopy from a nano-cell

Contents

2.1 Modeling transmission spectroscopy

The theoretical model describing transmission of a laser radiation through a layer of hot alkali atoms contained in a nano-cell is developed by following the approach presented in [9,17]. In order to describe the passage of an electromagnetic wave in an atomic medium, one needs to solve the Maxwell propagation equation and to evaluate the induced polarization P_0 in the medium. We consider a dilute gaseous medium formed by an ensemble of two-level identical atomic systems of levels $|g\rangle$ and $|e\rangle$, separated with the frequency $\hbar\omega_{eg}$, confined in a NC of thickness L, refractive index n and excited under normal incidence by an arbitrary polarized laser field

$$\mathbf{E}_{in}(z,t) = (\frac{1}{2}E_{in}e^{-i(\omega t - knz)} + c.c.)\mathbf{e}_E \tag{2.1}$$

of angular frequency $\omega = 2\pi\nu$ and wavenumber $k = \omega/c = 2\pi/\lambda$, propagating along the z-axis and the unit vector $\mathbf{e}_E$ is located in the plane (Oxy). We are interested in the study of the field transmitted through the cell. For this purpose as a first step we are going to express the amplitude E_t of the transmitted field,

$$\mathbf{E}_t(z,t) = (\frac{1}{2}E_t e^{-i(\omega t - knz + \phi)} + c.c)\mathbf{e}_E \tag{2.2}$$

and its intensity $I_t = E_t E_t^*$. As it was mentioned in the Chapter 1 the NC is formed with two highly parallel sapphire plates and presents itself a low-finesse Fabry-Pérot etalon of refractive index $n = 1.77$ at $\lambda = 895$ nm. The geometry of the problem is schematically illustrated in Fig. 2.1. The solution of the problem can be set as the sum of the resonant contribution of the medium $E_t^{'}$ and a contribution of an empty FP cell $E_t^{''}$:

$$E_t = E_t^{'} + E_t^{''}. \tag{2.3}$$

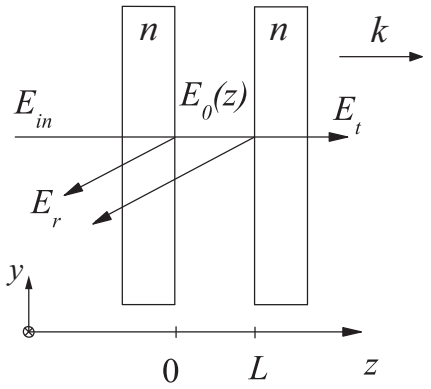

Figure 2.1: The geometry of the problem: an arbitrary polarized laser field of amplitude E_{in} propagates through hot alkali vapors confined between two sapphire plates of refractive index n, the transmitted amplitude E_t propagates in the same direction than that of E_{in}, while the field of amplitude E_r propagates in the backward direction.

We take the field E_0 and the polarization P_0 inside the cell in the form

$$\mathbf{E}_0(z,t) = (\frac{1}{2}E_0(z)e^{-i(\omega t - kz)} + c.c.)\mathbf{e}_E, \tag{2.4a}$$

$$\mathbf{P}_0(z,t) = (\frac{1}{2}P_0(z)e^{-i(\omega t - kz)} + c.c.)\mathbf{e}_E. \tag{2.4b}$$

The field transmitted inside the cell obeys Maxwell's equation for the wave propagation through the medium

$$\frac{\partial^2 E_0(z)}{\partial z^2} + 2ik\frac{\partial E_0(z)}{\partial z} = \frac{-k^2}{\varepsilon_0}P_0(z). \tag{2.5}$$

Solving this equation and using the continuity relations for the electric field at the boundaries $z = 0$ and $z = L$ [17], one obtains for the amplitude of the transmitted signal

$$E_t = E_t^{'} + E_t^{''} = \frac{t_{02}(I_f - 2rI_b)}{F} + \frac{t_{02}t_{10}E_{in}}{F}, \tag{2.6}$$

where the factor $F = 1 - r^2\exp(2ikL)$ takes into account the influence of the beam reflected by the second wall of the cell (which is important in the case were the cell thickness is $L \sim \lambda$), *i.e.* the Fabry-Pérot effect. Here, $r = (n-1)/(n+1)$, $t_{10} = 2n/(n+1)$ and $t_{02} = 2/(n+1)$ stand

for reflection and transmission coefficients, respectively, and

$$I_f = \frac{ik}{2\varepsilon_o}\int_0^L dz P_0(z,\omega), \quad I_b = \frac{ik}{2\varepsilon_o}\int_0^L dz P_0(z,\omega)e^{2ikz} \tag{2.7}$$

being the forward and backward integrals of the induced polarization P_0. The intensity of the transmitted beam is then

$$I_t = |E_t^{'}|^2 + |E_t^{''}|^2 + 2\Re(E_t^{'}E_t^{''}). \tag{2.8}$$

The dilute character of the gas implies $E_t^{'} \ll E_t^{''}$, which allows to neglect the first term in the rhs of Eq. 2.8 and hence the intensity of the transmitted beam mostly depends on $2\Re(E_t^{'}E_t^{''})$, we get

$$S_t \propto \frac{2t_{10}t_{02}^2}{|F|^2}E_{in}\Re(I_T), \tag{2.9}$$

with $I_T = I_f - rI_b$.

The polarization of the medium formed by an ensemble of two-level systems on the frequency of the laser filed is determined by averaging the coherences of the reduced density matrix σ over the distribution of speed $W(v)$, assumed to be Maxwellian (see [9]):

$$P(z,\omega) = N\mu_{eg}\int dv W(v)\sigma_{eg}(z,v,\Delta), \tag{2.10}$$

where N is the atomic density with μ_{eg} being the dipole moment between the states $|e\rangle$ and $|g\rangle$ and $\sigma_{eg}(z,v,\Delta)$ is the optical coherences expressed in the rotating frame and $\Delta = \omega - \omega_{eg}$ is the frequency detuning of the scanning field which is broadened by the Doppler effect term $\pm kv$, depending whether the atom is moving along increasing or decreasing z.

$$\rho_{eg}(z,v,\Delta,t) = \sigma_{eg}(z,v,\Delta)e^{i(kz-\omega t)} + h.c. \tag{2.11}$$

The evolution of the density matrix σ is given by the Liouville equation of motion

$$\frac{d}{dt}\sigma = \frac{1}{i\hbar}\left[H, \sigma\right] + \Gamma\sigma, \tag{2.12}$$

where Γ is the relaxation matrix and H is the Hamiltonian of the atomic system placed in a static magnetic field interacting with a laser field and reads as

$$H = H_m^d - \mathbf{E}\cdot\mathbf{d} = \hbar\omega_{eg}|e\rangle\langle e| - \hbar\Omega|e\rangle\langle g| - \hbar\Omega|g\rangle\langle e|, \tag{2.13}$$

where $\Omega = \boldsymbol{E}\cdot\boldsymbol{\mu_{ge}}/\hbar$ is the Rabi frequency. The Hamiltonian H_m^d is obtained after the diagonalization of the atom-magnetic field interaction Hamiltonian H_m, whose expression will be derived in section 2.2.

Making use of the relation $\dot{w}(z,t) = (\partial_t + v\partial_z)w$, it gives, for the coherences in the steady state regime, the following differential equation:

$$v\frac{\partial}{\partial z}\sigma_{eg} = i\Omega(\sigma_{gg} - \sigma_{ee}) - \Lambda_{\pm}\sigma_{eg}, \tag{2.14}$$

where $\Lambda_{\pm} = \frac{1}{2}\gamma - i\Delta \pm ikv$ is a function of the homogeneous linewidth γ (full width at half maximum). It is well assumed that optical coherences are destroyed when atoms collide with the cell walls, meaning that the good initial conditions are $\sigma_{eg}(0, v, \Delta) = \sigma_{eg}(L, v, \Delta) = 0$. As atoms may move along increasing or decreasing z, the integral in Eq. (2.10) should be performed on both positive and negative velocities:

- atoms departing from $z = 0$, moving to $z = L$ with a positive velocity see a total detuning $\Delta - kv$,
- atoms departing from $z = L$, moving to $z = 0$ with a negative velocity see a total detuning $\Delta + kv$.

Note that $\sigma_{eg}(L-z,v,-\Delta) = -\sigma^*_{eg}(z,v,\Delta)$, the integral in Eq. (2.10) can be performed only on positive velocities

$$P(z,\omega) = N\mu_{eg}\int_0^{+\infty} dvW(v)\left\{\sigma_{eg}(z,v,\Delta) - \sigma^*_{eg}(z,v,\Delta)\right\}. \tag{2.15}$$

The solution of Eq. (2.14) can be found without taking into account the equations on the populations σ_{gg}, σ_{ee} if we consider a non-saturating field, meaning that Ω is small compared to Λ, and the term $\sigma_{gg} - \sigma_{ee} \approx 1$. Equation (2.14) can then be re-written as

$$v\frac{\partial}{\partial z}\sigma_{eg} = i\Omega - \Lambda_+\sigma_{eg}, \tag{2.16}$$

for positive velocities, and the solution is easily calculated using the variation of parameters

$$\sigma_{eg}(z,v,\Delta) = \frac{i\Omega}{\Lambda_+}\left[1 - \exp\left(-\frac{\Lambda_+}{v}z\right)\right]. \tag{2.17}$$

The equivalent of Eq. (2.16) for negative velocities reads

$$-v\frac{\partial}{\partial z}\sigma_{eg} = i\Omega - \Lambda_-\sigma_{eg}, \tag{2.18}$$

and the solution is

$$\sigma_{eg}(L-z,v,\Delta) = \frac{i\Omega}{\Lambda_-}\left[1 - \exp\left(-\frac{\Lambda_-}{v}(L-z)\right)\right]. \tag{2.19}$$

Injecting the solutions for both positive and negative velocities into Eq. (2.15), and making the assumption that $\boldsymbol{E}$ and $\boldsymbol{\mu}$ are aligned, we arrive at

$$P(z,\omega) = \frac{i}{\hbar}NE(\omega)|\mu_{eg}|^2\int_0^{+\infty} dvW(v)R(z,v,\Delta). \tag{2.20}$$

with

$$R(z,v,\Delta)=\frac{1}{\Lambda_+}\left[1-\exp\left(-\frac{\Lambda_+}{v}z\right)\right]+\frac{1}{\Lambda_-}\left[1-\exp\left(\frac{\Lambda_-}{v}(L-z)\right)\right]. \tag{2.21}$$

Coming back to the notation used in [17], in the linear regime of interaction I_T takes the form

$$I_T=I_f-rI_b=\left[1+r^2\exp(2ikL)\right]I_T^{lin}-2rI_{SR}^{lin}, \tag{2.22}$$

where the integrals I_{SR}^{lin} and I_T^{lin} are, respectively, associated with selective reflection and transmission signals, and take the form

$$I_{SR}^{lin}=C\int_{-\infty}^{0}dvW(v)h_-(\Delta,\gamma,L,v)+C\int_{0}^{+\infty}dvW(v)h_+(\Delta,\gamma,L,v), \tag{2.23a}$$

$$I_T^{lin}=C\int_{-\infty}^{+\infty}dvW(v)g(\Delta,\gamma,L,v), \tag{2.23b}$$

with

$$g(\Delta,\gamma,L,v)=-\frac{k}{\Lambda_+}\left\{L-\frac{|v|}{\Lambda_+}\times\left[1-\exp\left(-\frac{\Lambda_+L}{|v|}\right)\right]\right\}, \tag{2.24a}$$

$$h_\pm(\Delta,\gamma,L,v)=\frac{1}{2i}\left[\frac{1}{\Lambda_\mp}-\frac{\exp(2ikL)}{\Lambda_\pm}\right]-\frac{k|v|}{\Lambda_+\Lambda_-}\exp\left(-\frac{\Lambda_\mp L}{|v|}\right). \tag{2.24b}$$

The plus sign refers to the atoms with the veocity $\mathbf{v}$ in the positive dierction of the cell axis, and the minus sign refers to the atoms with $\mathbf{v}$ in the negative direction of the cell axis. In (2.23a) and (2.23b), C is a constant proportional to the square of the dipole moment of the transition from state $|g\rangle$ to state $|e\rangle$ and reads

$$C=\frac{Nt_{10}E_{in}}{4\hbar\varepsilon_0F}|\langle e|\mu_{eg}|g\rangle|^2. \tag{2.25}$$

2.2 Interaction with a static magnetic field

In this section, we will discuss the interaction of an electromagnetic field described by the components $\mathbf{A}$ and V of the electromagnetic four-potential with an atom having spin 1/2 (up to order v^2/c^2) which is given by the time-independent Dirac equation.

$$\left[\frac{1}{2m_e}(\mathbf{p}+\frac{e}{c}\mathbf{S})^2+\frac{e}{m_e c}A\cdot\boldsymbol{\nabla}\times\mathbf{A}-\frac{p^4}{8{m_e}^3c^2}-\frac{e\hbar^2}{8{m_e}^2c^2}\Delta V-\frac{e}{2{m_e}^2c^2}\mathbf{S}\cdot(\boldsymbol{\nabla}V\times\mathbf{p})-eV\right]\Psi=E\Psi, \tag{2.26}$$

with $\mathbf{S}=\hbar\boldsymbol{\sigma}/2$ is the spin momentum of the electron with $\boldsymbol{\sigma}=(\sigma_x,\sigma_y,\sigma_z)$, $\sigma_i(i=x,y,z)$ are the Pauli matrices, $\mathbf{p}$ is the impulsion, m_e is the electron rest mass. The Dirac equation gives very accurate description of hydrogen atom energy levels and since alkali metals also have one electron in their outermost orbit $n^1S_{1/2}$ ($n=3$ for Li, $n=4$ for Na, $n=5$ for Rb, $n=6$ for Cs, etc) the Dirac equation is also applicable to this group of atoms.

The Dirac equation includes the kinetic energy and the interaction term with a magnetic field represented by vector potential $\mathbf{A}$, the interaction of the spin magnetic momentum with the applied magnetic field, the kinetic energy first order relativistic correction, the Darwin term (affects only the S states and produces an energy shift), the spin-orbital interaction and the scalar potential energy.

2.2.1 Non-relativistic electron Hamiltonian

When considering a non-relativistic electron in the gauge $\{\mathbf{A}=\mathbf{0},V\}$ the Dirac equation is then replaced by the Schrödinger equation for a free electron and can be written as

$$H_0\Psi=[H_k+H_p]\Psi_n=(\frac{p^2}{2m_e}-eV)\Psi_n=E_n\Psi_n. \tag{2.27}$$

The solution of Eq. (2.27) in the case of atomic bounded states and for a spherically symmetric electrostatic potential $V\equiv V(r)=e/r$ is know to be Bohr derivation of the energy of each orbit

of the hydrogen atom and is

$$E_n = -\mathcal{R}\frac{1}{n^2}, \tag{2.28}$$

with $\mathcal{R} \equiv m_e e^4/8\varepsilon_0 h^2 \approx 13.6$ eV, is the Rydberg constant.

The the spin-orbit term for hydrogen like atoms inside of a potential, in the central field approximation, can be written as:

$$H_{SO} = -\frac{e}{2{m_e}^2 c^2}\mathbf{S}\cdot(\boldsymbol{\nabla}V \times \mathbf{p}) = \zeta(r)\mathbf{L}\cdot\mathbf{S}, \tag{2.29}$$

with $\zeta(r) = -Ze^2/(2m_e^2c^2r^3)$. Combining Eqs. (2.27) and (2.29) in the case of a potential $V = Ze/r$, one has

$$H = H_0 + H_{SO} = -\frac{\hbar^2}{2m_e}\Delta^2 - \frac{Ze^2}{r} + \zeta(r)\mathbf{L}\cdot\mathbf{S}. \tag{2.30}$$

The coupling between the orbital angular momentum $\mathbf{L}$ and its spin angular momentum $\mathbf{S}$ results in the fine structure. The coupled basis $|L, S, J, m_J\rangle$ and the uncoupled basis$|L, S, m_L, m_S\rangle$ are both the eigenfunctions of the Hamiltonian, meanwhile the uncoupled basis is not eigenfunction of $\mathbf{L}\cdot\mathbf{S}$. Hence, we describe the Hamiltonian in the coupled basis $|L, S, J, m_J\rangle$, where $\mathbf{J} = \mathbf{L} + \mathbf{S}$ is the electron total angular momentum with the projection m_J.

The next step is to find the matrix elements of H_{SO},

$$E_{SO} = \langle L, S, J, m_J|H_{SO}|L', S', J', m'_J\rangle. \tag{2.31}$$

It is important to note that L^2, S^2 and J^2 have only diagonal elements and the off-diagonal elements arise from r^{-3}. According to the perturbation theory the non-diagonal elements can be neglected if they are small compare with the first order correction to the wave function which is the case here. Thus the eigenvalues read

$$E_{SO} = \frac{Z^4e^2\hbar^2}{4a_0^3m_e^2c^2}\cdot\frac{J(J+1) - L(L+1) - S(S+1)}{n^3(L+1)(L+\frac{1}{2})L}. \tag{2.32}$$

The next term in the Dirac Hamiltonian is the kinetic energy first order relativistic correction Hamiltonian $H_R = -\frac{p^4}{8m_e c^2}$, which also has only diagonal elements having the form

$$E_R = -E_n \cdot \frac{Z^2 e^2}{\alpha_0} \cdot \left(\frac{3}{4n^2} - \frac{1}{n(L+1/2)} \right), \tag{2.33}$$

here $\alpha_0 \equiv 4\pi\epsilon_0 \hbar^2 (m_e^2 e^2)^{-1} \approx 53\mathring{A}$ is the Bohr radius. The last term of the Dirac Hamiltonian is the Darwin term $H_D = -\frac{e\hbar^2}{8{m_e}^2 c^2}\Delta V$, which is non-zero only for $L = 0$ states (S-states),

$$E_D = 2E_n^2 \cdot \frac{n}{m_e c^2}. \tag{2.34}$$

To summarize the fine structure Hamiltonian H_f is then

$$H_f = H_0 + H_{SO} + H_R + H_D. \tag{2.35}$$

It is important to note, that Diracs' equation omits the possible interaction between the nuclear spin momentum $\mathbf{I}$ and the electron total angular momentum $\mathbf{J}$. The coupling of $\mathbf{J}$ and $\mathbf{I}$ results in the hyperfine structure of an atom where the total atomic angular momentum $\mathbf{F}$ is given by $\mathbf{F} = \mathbf{L} + \mathbf{S} + \mathbf{I} = \mathbf{J} + \mathbf{I}$. The Hamiltonian that describes the hyperfine structure for each of the D-line components is given in [63, 64].

$$H_{hfs} = A_{hfs}\mathbf{I}\cdot\mathbf{J} + B_{hfs}\frac{3(\mathbf{I}\cdot\mathbf{J})^2 + \frac{3}{2}(\mathbf{I}\cdot\mathbf{J}) - I(I+1)J(J+1)}{2I(2I-1)J(2J-1)}, \tag{2.36}$$

A_{hfs} is the magnetic dipole constant and B_{hfs} is the electric quadrupole constant.

2.2.2 Introducing the magnetic field: Zeeman effect

In the following section will introduce the magnetic field $\mathbf{B}$, which is assumed to constant and uniform ($\mathbf{A} = \frac{1}{2}(\mathbf{B}\times\mathbf{r}), i.e. \boldsymbol{\nabla}\cdot\mathbf{A} = 0$), the latter is fully verified by comparing theoretical and experimental results: one of the advantages of the NC is that, due to the small thickness of

the cell, the variation of the magnetic field inside the NC is several order less than the applied B.Thus we can suppose the magnetic field being homogeneous within the cell. Later, we will see that this hypothesis of homogeneity of the magnetic field within the NC is very well verified by comparing the experimental and calculated results.

The magnetic part H_B of the Dirac equation limited to v^2/c^2 order reads

$$H_B = \frac{\mu_B}{\hbar}\mathbf{B}(\mathbf{L} + 2\mathbf{S} + \mathbf{I}), \tag{2.37}$$

which can be rewritten in a more simple form

$$H_B = -\boldsymbol{\mu}_L \cdot \mathbf{B} - \boldsymbol{\mu}_S \cdot \mathbf{B} - \boldsymbol{\mu}_I \cdot \mathbf{B}, \tag{2.38}$$

using the notations of spin $\boldsymbol{\mu}_S = -g_S\mu_B\mathbf{S}$, orbital $\boldsymbol{\mu}_L = -g_L\mu_B\mathbf{L}$ and nuclear $\boldsymbol{\mu}_I = -g_I\mu_B\mathbf{I}$ magnetic momenta and Bohr magneton $\mu_B = 1.399624$ MHz/G.

Since $\mathbf{B}$ is supposed to be constant and uniform, the frame $(Oxyz)$ can be chosen in such a way that $\mathbf{B} = B\mathbf{e_z}$, defining the quantization axis, thus

$$H_B = \frac{\mu_B B}{\hbar}(g_L L_z + g_S S_z + g_I I_z), \tag{2.39}$$

where L_z, S_z, I_z are the projections of the orbital, spin and nuclear quantum momenta along the z axis with their respective Landé factors, g_L, g_S and g_I.

Hence, the total Hamiltonian can be expressed as the sum of the unperturbed atomic Hamiltonian H_{hfs} with the magnetic interaction Hamiltonian H_B and reads:

$$H = H_{hfs} + H_B, \tag{2.40}$$

The diagonal elements of the Hamiltonian are given in [65]

$$\langle F, m_F|H|F, m_F\rangle = E_0(F) + \mu_B g_F m_F B, \tag{2.41}$$

where $E_0(F)$ is the (degenerate) energy of the hyperfine structure sub-levels having quantum number F in the absence of magnetic field, and g_F is the associated Landé factor. The off-diagonal elements are non zero only between the sub-levels satisfying conditions $\Delta F = \pm 1$ and $\Delta m_F = 0$ and are defined as

$$\begin{aligned}\langle F-1, m_F|H|F, m_F\rangle = \langle F, m_F|H|F-1, m_F\rangle = \frac{\mu_B B}{2}(g_J - g_I)\times \\ \left(\frac{[(J+I+1)^2 - F^2][F^2-(J-I)^2]}{F}\right)^{1/2}\left(\frac{F^2-m_F^2}{F(2F+1)(2F-1)}\right)^{1/2},\end{aligned} \tag{2.42}$$

where g_J is the Landé factor associated to the quantum number J. The Hamiltonian matrix is then a block diagonal matrix where each block corresponds to a given value of m_F.

As an example, we represent here-after the Hamiltonian matrix for ^{133}Cs ground state sub-levels. Since the frequency differences between the ground state $6^2S_{1/2}$ and the excited states $6^2P_{1/2}$ and $6^2P_{3/2}$ are huge compared with the frequency differences between the ground or excited state sub-levels, hence we may study the state $6^2S_{1/2}$ separately from the excited state.

$$
H = \begin{array}{c} \\ \langle 4,-4| \\ \langle 4,-3| \\ \langle 3,-3| \\ \vdots \\ \langle 4,3| \\ \langle 3,3| \\ \langle 4,4| \end{array}
\begin{array}{c}
\begin{array}{ccccccc} |4,-4\rangle & |4,-3\rangle & |3,-3\rangle & \cdots & |4,3\rangle & |3,3\rangle & |4,4\rangle \end{array} \\
\begin{pmatrix}
E_0(4)+\mu_B B & & & & & & \\
& E_0(4)+\frac{3}{4}\mu_B B & -\frac{\sqrt{7}}{4}\mu_B B & & & & \\
& -\frac{\sqrt{7}}{4}\mu_B B & E_0(3)-\frac{3}{4}\mu_B B & & & 0 & \\
& & & \ddots & & & \\
& & & & E_0(4)-\frac{3}{4}\mu_B B & -\frac{\sqrt{7}}{4}\mu_B B & \\
& 0 & & & -\frac{\sqrt{7}}{4}\mu_B B & E_0(3)+\frac{3}{4}\mu_B B & \\
& & & & & & E_0(4)-\mu_B B
\end{pmatrix}
\end{array}
$$

Diagonalization of the Hamiltonian allows the determination of the eigenvectors and eigenvalues (respectively corresponding to the mixing coefficients and energies) of the Zeeman sub-levels. The new state vectors can be expressed in terms of the initial unperturbed atomic state vectors as

$$|\Psi(F_g, m_g)\rangle = \sum_{F'_g} c_{F_g F'_g} |F'_g, m_{Fg}\rangle, \tag{2.43}$$

$$|\Psi(F_e, m_e)\rangle = \sum_{F'_e} c_{F_e F'_e} |F'_e, m_{Fe}\rangle. \tag{2.44}$$

The state vectors $\left|F'_g, m_g\right\rangle$ and $|F'_e, m_e\rangle$ are the ground and excited unperturbed state vectors. The coefficients $c_{F_g F'_g}$ and $c_{F_e F'_e}$ are the ground and excited states mixing coefficients which depend on the B-field strength and magnetic quantum numbers m_{Fe} and m_{Fg}.

The dipole moment of a transition μ_{eg} induced by the interaction of the atoms with the laser electric field, is linked to the spontaneous emission rate of the associated transition A_{eg}, such that

$$|\langle e|\mu_q|g\rangle|^2 = \frac{3\varepsilon_0 \hbar^2 \lambda_{eg}}{8\pi^2} A_{eg} \propto a^2 \left[\Psi(F_e, m_{Fe}); \Psi(F_g, m_{Fg}); q\right], \tag{2.45}$$

where the transfer coefficients $a\left[\Psi(F_e, m_{Fe}); \Psi(F_g, m_{Fg}); q\right]$ are given by

$$a\left[\Psi(F_e, m_{Fe}); \Psi(F_g, m_{Fg}); q\right] = \sum_{F_e' F_g'} c_{F_e F_e'} a\left(F_e, m_{Fe}; F_g, m_{Fg}; q\right) c_{F_g F_g'}, \tag{2.46}$$

with $q = 0, \pm 1$ is associated to polarization of the exciting electric field and unperturbed transfer coefficients $a(F_e, m_{F_e}; F_g, m_{F_g}; q)$, which have the following definition

$$\begin{aligned} a(F_e, m_{F_e}; F_g, m_{F_g}; q) = (-1)^{1+I+J_e+F_e+F_g-m_{Fe}} \\ \times \sqrt{2J_e+1}\sqrt{2F_e+1}\sqrt{2F_g+1} \\ \times \begin{pmatrix} F_e & 1 & F_g \\ -m_{F_e} & q & m_{F_g} \end{pmatrix} \begin{Bmatrix} F_e & 1 & F_g \\ J_g & I & J_e \end{Bmatrix}. \end{aligned} \tag{2.47}$$

Here the parentheses denote the 3-j and the curly brackets are the 6-j symbols.

2.3 Numerical simulations

2.3.1 Computational model

A computational program, which calculates the transition frequencies (with respect to their initial positions) and transition intensity modifications while varying the magnetic field has been developed using FORTRAN90. The magnetic field B varies from 0 to 10 T with a step of 10^{-5}T. Such interval is chosen to completely cover the experimental values.

The program is constructed in the following way: as a first step, all the characteristic data of the atomic system are introduced, such as the quantum numbers describing the hyperfine structure of the studied atom, the Landé factors whose experimental values can be found in [60], the polarization of the laser radiation, the latter modifies the selection rules, and the minimum and the maximum values of the magnetic field. It is important to mention, that the code is written so that it is readily applicable to all alkali atoms.

In the next step the program diagonalizes the Hamiltonian by solving the characteristic equation:

$$det\,|H - \lambda\mathbb{I}| = 0, \tag{2.48}$$

where λ is an eigenvalue of H and $\mathbb{I}$ denotes the identity matrix. The eigenvectors of the Hamiltonian can be found from the relation

$$H\Psi_i = \lambda_i\Psi_i, \tag{2.49}$$

where λ_i denotes the i^{th} eigenvalue with corresponding eigenvector Ψ_i.

Due to the degeneracy of the hyperfine levels, crossing of energy levels is possible. This causes some difficulties for the computing program to distinguish and to match the eigenvalues with their corresponding eigenfunctions. In order to solve this problem, the program performs a first order derivation with respect to B of the given eigenvalue, identifies the good value and matches with its eigenfunction.

In the next step, the calculation of energy level shifts is performed. Then using Eqs. (2.46), (2.47) the program calculates transition intensities for all the possible transitions of the system. When the maximum value of the B-field is achieved, the program records all the data in an external .dat file and stops.

2.3.2 Simulations

Absorption signal versus thickness

It was shown in [9, 51] that the spectral width and the amplitude of the absorption signal oscillate when changing the thickness of the cell; in particular the spectral width gets enlarged at thicknesses $L = m\lambda$ and reaches its minimum when $L = (2m+1)\lambda/2$ (where m is an integer). This effect is known as collapse and revival of the coherent Dicke narrowing effect. The presented theoretical model predicts the CDN behavior of the absorption signal, and as an example, here

after the results of performed numerical calculations of Cs D_1 line absorption spectra for atomic transitions $F_g = 4 \rightarrow F_e = 3, 4$ are presented in Fig. 2.2. In order to illustrate the CDN effect,

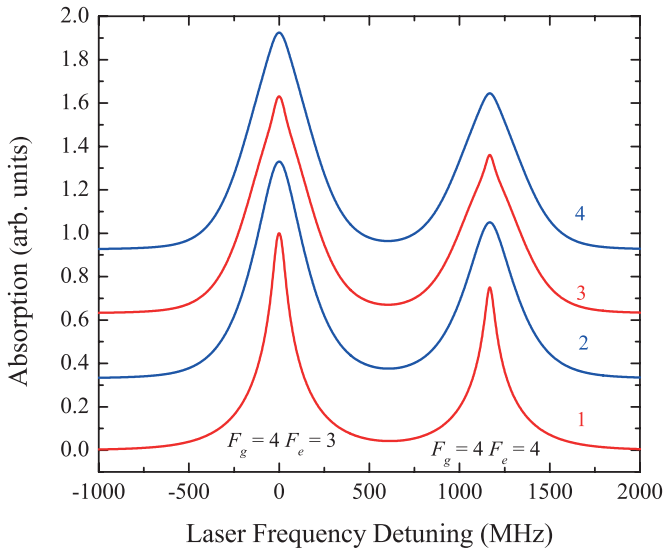

Figure 2.2: Absorption spectra of the Cs D_1 line $F_g = 4 \rightarrow F_e = 3, 4$ transitions for the thicknesses $L = \lambda/2 = 447.5$ nm (curve *1*), $L = \lambda = 895$ nm (curve 2), $L = 3\lambda/2 = 1342.5$ nm (curve 3), and $L = 2\lambda = 1790$ nm (curve *4*). For convenience, the curves have been shifted vertically.

our calculations were performed from the thickness $L = \lambda/2$ to $L = 2\lambda$ with a step of $\lambda/2$. The amplitudes of these transitions are given by the oscillator strength factors $S_{43'} = 7/12$, $S_{44'} = 5/12$ (see Eq. (41)) in [60]. The narrowing of the signal is clearly visible in the absorption spectra at $L = \lambda/2$ nm and $L = 3\lambda/2$ nm, and a strong broadening of the spectra is seen at $L = \lambda$ and $L = 2\lambda$ (collapse of CDN). The theoretical predictions presented in Fig. 2.2 are in agreement with the obtained experimental results for the D_2 line of rubidium atoms [38] as well as for the D_1 line of potassium atoms [34].

There are several advantages to use the thickness $L = \lambda/2$. From the experimental point of view the absorption spectra detection at thickness $L = \lambda/2$ requires a power of the laser radiation intensity of several μW which is 10^3 times less than in the case of the thickness $L = \lambda$ where $P_L = 1$ mW. Moreover, spatial resolution is two times better for $L = \lambda/2$ than for $L = \lambda$, the latter is very important when a strongly inhomogeneous magnetic field is applied.

Transition intensity and shift versus magnetic field

Further, we are interested in studying the evolution of Cs D_1 $F_g = 4 \rightarrow F_e = 3, 4$ transitions versus a magnetic field. In case of π polarized laser radiation, according to the electric dipole selection rules when a weak magnetic field is applied, the transitions obeying $\Delta F = F_e - F_g = \pm 1; 0$ and $m_F = 0$ are allowed.

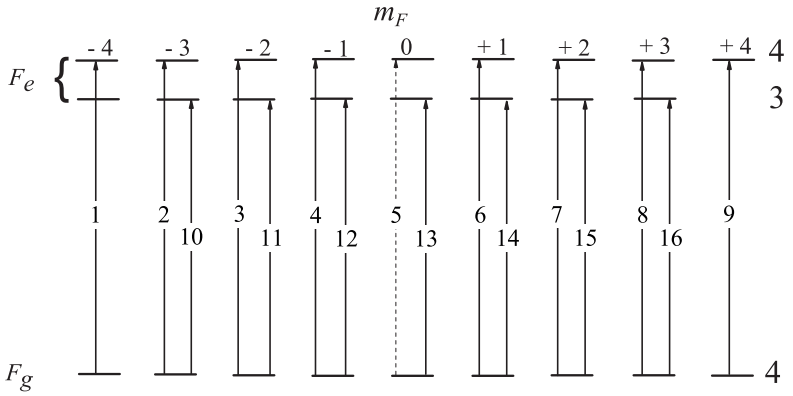

Figure 2.3: Diagram of the Cs D_1 line $F_g = 4 \rightarrow F_e = 3, 4$ atomic transitions in case of π polarization.The selection rules are $\Delta F = \pm 1; 0, \Delta m_F = 0$

In Fig. 2.3, one may see that for weak magnetic fields 16 atomic transitions exist, from which transitions labelled 1 - 9 are the $F_g = 4 \rightarrow F_e = 3$ ones and transitions labeled 10 - 16 relate to $F_g = 4 \rightarrow F_e = 4$ transitions. The transition $F_g = 4, m_F = 0 \rightarrow F_e = 4, m_F = 0$, labelled 5 (dashed line) is forbidden in zero magnetic field, but with the increase of B its probability increases and for some values of magnetic field it is even bigger than the one from allowed ones.

In order to give a complete information about the evolution of atomic transitions in a static magnetic field, we have calculated the transition frequency shifts and probabilities as a function of B.

The frequency shifts dependence on magnetic field, where the magnetic field changes from 0 to 1 T is presented in Fig. 2.4. It is seen that for $B > 8.5$ kG, the frequency separation between two adjacent transitions from 2 to 16 tends to the same value.. This is the manifestation of the Hyperfine Paschen-Back (HPB) effect. The transition labelled 1 joins the group of transitions

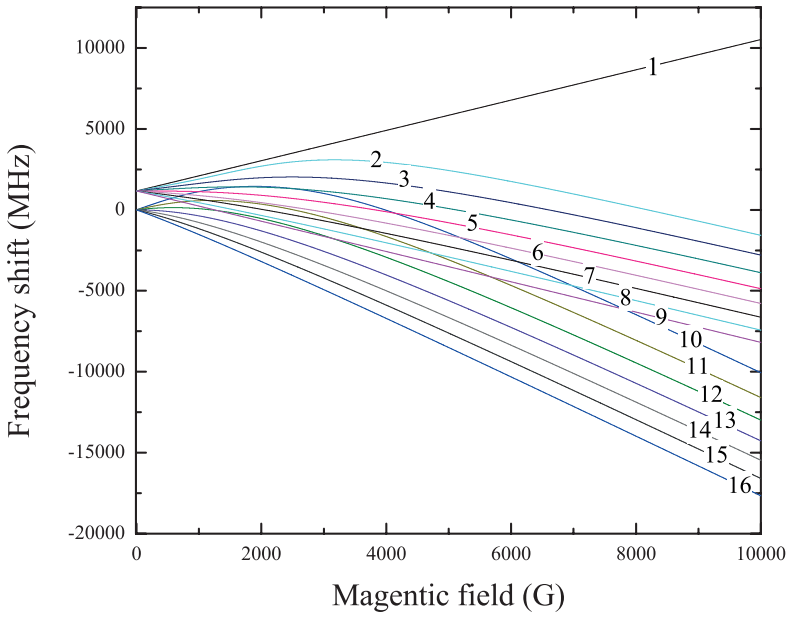

Figure 2.4: Cs D_1 line transition frequency shifts versus magnetic field in case of π polarization. The selection rules are $\Delta F = \pm 1; 0, \Delta m_F = 0 = 0$.

arising from the level $F_g = 3$ in the HPB regime. The transition intensities are significantly different at weak magnetic fields, but tend asymptotically to two limit values with the increase of B. Transitions probabilities labelled 10 - 16 tend to zero, meanwhile the probabilities of the transitions 1 - 9 tend to the same transition intensity (0.08 in arbitrary units). Thus, from the initial 16 transitions only 9 remain in strong magnetic fields. The transition labelled 9 is called "Guiding Transition" [66], since it has an invariant amplitude with the increase of B-field.

Evolution of $F_g = 4 \rightarrow F_e = 3, 4$ transitions in magnetic field

When the external field is applied, the coupling between electronic and nuclear angular momenta is gradually destroyed, leading to the complete decoupling of the bond in very strong magnetic fields. In the case of relatively weak magnetic fields ($B \ll B_0$), the splitting of the atomic levels is described by the total angular momentum $\mathbf{F} = \mathbf{J} + \mathbf{I}$, and its projection m_F, where $\mathbf{J} = \mathbf{L} + \mathbf{S}$ is the total angular momentum of the atom. To evaluate the intensity (weak or strong) of a magnetic field a characteristic value is introduced: $B_0 = A_{hfs}/\mu_B \approx 1.7$ kG, where A_{hfs} is the Cs ground state hyperfine coupling coefficient and μ_B is the Bohr magneton [67].

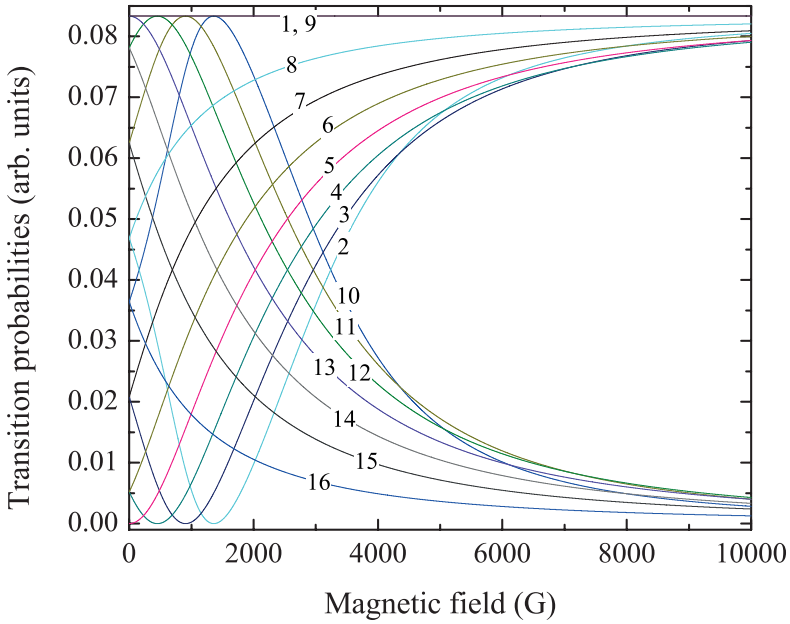

Figure 2.5: Cs D_1 line transition probabilities versus magnetic field in case of π polarization. The selection rules are $\Delta F = \pm 1; 0, \Delta m_F = 0$.

In this section, we study theoretically the evolution of $F_g = 4 \rightarrow F_e = 3, 4$ transitions in relatively strong magnetic fields using the absorption spectra from a NC with the thickness of $L = \lambda/2$. The results of the numerical calculations are presented in Fig. 2.6. During the calculations the temperature $T = 140$ °C, the FWHM is 40 MHz and the laser polarization were preserved. The magnetic field value is increasing from bottom to top order for the curves presented in Fig. 2.6. Magnetic field induction B increases upward and ammounts to $B = 500$, 2000, 4000, 6000 G in the spectra labeled $1, 2, 3, 4$, respectively. It is worth to note that, with the increase of magnetic field, atomic transitions become equidistant and tend to the high-frequency part of the spectrum (positive frequency shift). The Paschen-Back regime for the Cs atoms begins for fields $B \gg 1700$ G [67].

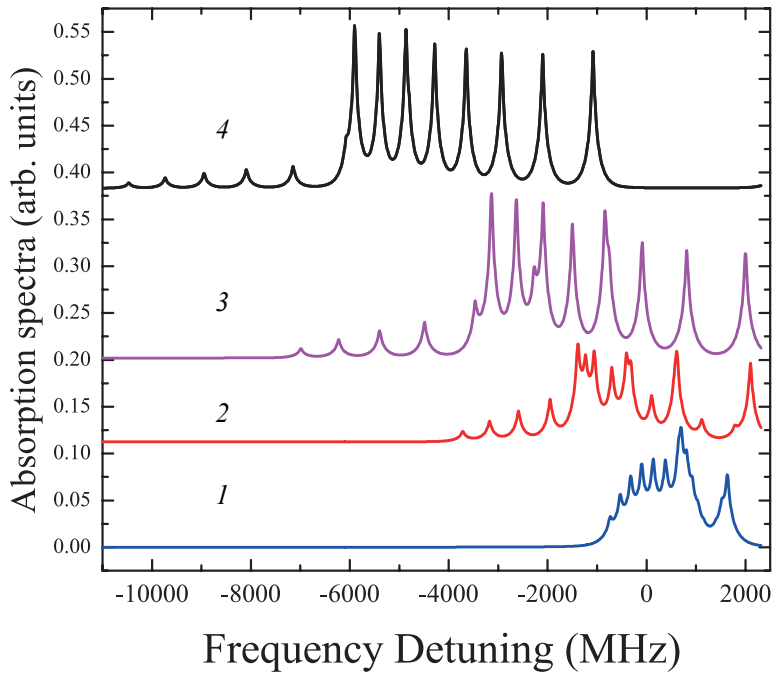

Figure 2.6: Evolution of Cs D_1 line $F_g = 4 \rightarrow F_e = 3, 4$ atomic transitions for $B = 500$ G (1), $B = 2000$ G (2), $B = 4000$ G (3), and for $B = 6000$ G (4).

2.4 Atomic transition of Cs D_2 line in a strong transverse magnetic field

The sketch of the experimental setup is shown in Fig. 2.7. The linearly polarized beam of extended cavity diode laser radiation (ECDL, $\lambda = 852$ nm, $P_L = 5$ mW, $\gamma_L \cong 1$ MHz) resonant with the Cs D_2 transition is passed through a Faraday isolator (FI). After passing the FI the propagation is split with the help of a beam splitter (BS). The first part of the radiation is sent to the auxiliary (Reference) Cs contained nano-cell with the vapor column thickness $L = \lambda = 852$ nm, which is placed in a $B = 0$ field (*3*) and its transmission spectrum is used as a reference.

The second part is directed to a polarization beam splitter (PBS). After the PBS, the radiation is focused (spot diameter ~ 1 mm) at nearly normal incidence onto the Cs NC (*2*) with the vapor column thickness $L = \lambda/2 = 426$ nm. The nano-cell is placed between the permanent

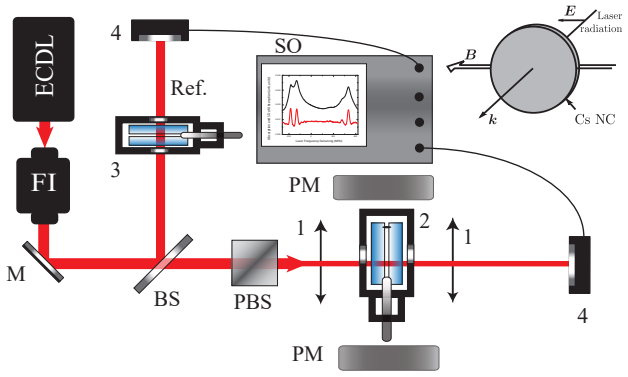

Figure 2.7: Sketch of the experimental setup. The laser radiation produced by ECDL; FI - Faraday isolator; BS - beam splitter; PBS - Polarization beam splitter is used to ensure **E** of laser radiation is parallel to **B** of magnetic field; PM - permanent magnets; M - mirror; 1 - lenses; 2 - Nano-metric thickness cell, inside the oven; 3 - Cs contained auxiliary nano-cell placed in $B = 0$ field; 4 - photodiodes; SO - Tektronix TDS2014B digital four-channel storage oscilloscope. The upper branch is to form the Reference spectrum. On the right side of the setup the configuration of **E** and **B** field is presented.

magnets, which are placed such that the magnetic field B is directed along the laser field vector E ($\mathbf{E} \parallel \mathbf{B}$). The PMs are fixed on nonmagnetic holders. The transmission signal is detected by a photodiode (4) and is recorded by a Tektronix TDS2014B digital four-channel storage oscilloscope (SO). The choice of the thickness $L = \lambda/2$ is motivated by the CDN properties of the signal. When the distance between the PMs is about 0.8 cm, the magnetic field is $B = 6800$ G. Moderate magnetic fields in the range 10 - 200 G are produced by Helmholtz coils. The B-field strength is measured by a calibrated Hall gauge.

In the theoretical model we have made an assumption of having a uniform magnetic field, which is fully verified by comparing theoretical and experimental results: one of of the advantages of the NC is that, due to the small thickness of the cell, the variation of the magnetic field inside the NC is several order less than the applied B. Thus we can suppose the magnetic field being homogeneous within the cell. Later, we will see that this hypothesis of homogeneity of the magnetic field within the NC is very well verified by comparing the experimental and calculated results. When the applied magnetic field is strong ($B \gg B_0$), i.e. strong enough to

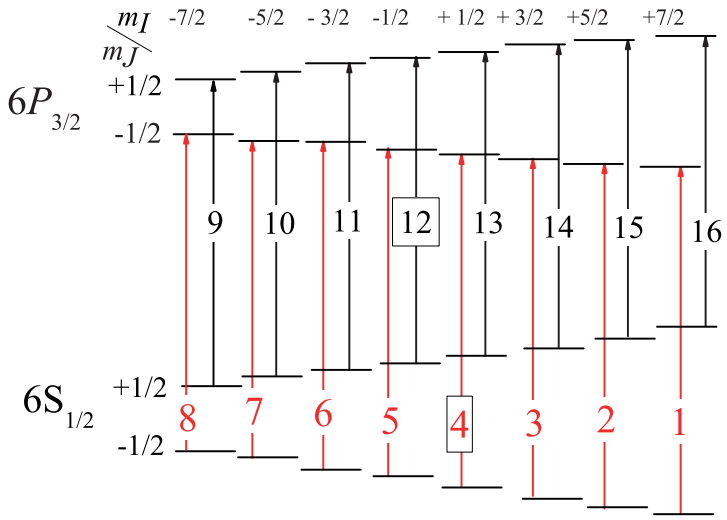

Figure 2.8: Diagram of the Cs D_2 hyperfine structure in Paschen-Back regime. The selection rules are $\Delta m_J = 0$, $\Delta m_I = 0$.

destroy the coupling between electronic and nuclear angular momentum and interact with them independently, the eigenstates of the Hamiltonian are described by the uncoupled basis of **J** and **I** and their projections (m_J, m_I). The nuclear angular momentum **I** of ^{133}Cs is equal to 7/2, which means that its projection m_I takes values from -7/2 to 7/2. The electronic angular momentum is $J = 3/2$, it has 4 projections which are $m_J = 3/2, m_J = 1/2, m_J = -1/2, m_J = -3/2$. In the HPB regime for the π polarized laser radiation, the section rules are $\Delta m_J = 0$, $\Delta m_I = 0$. Fig. 2.8 shows 16 atomic transitions for the case of π polarized laser excitation in the HPB regime. The transitions labeled 4 and 12 are forbidden in zero magnetic field, since in the initial basis they satisfy the selection rule $\Delta F = 0, \Delta m_F = 0$.

Cesium D_2 line absorption spectrum for the transitions $F_g = 4 \rightarrow F_e = 5$ from a $\lambda/2$ nano-cell at $B = 5650$ G and when the π polarized laser radiation is applied is presented in Fig. 2.9. The red and blue curves are the experimental and the theoretical absorption spectra, respectively. As it is seen in Fig. 2.9, the obtained experimental results are fully consistent with theoretical modeling. The Reference curve obtained via $L = \lambda$ auxiliary cell was used for frequency axis scaling but it is not presented among the results. The transitions are spatially resolved in both spectra. The transitions that are marked by a square are forbidden at $B = 0$. They appear for

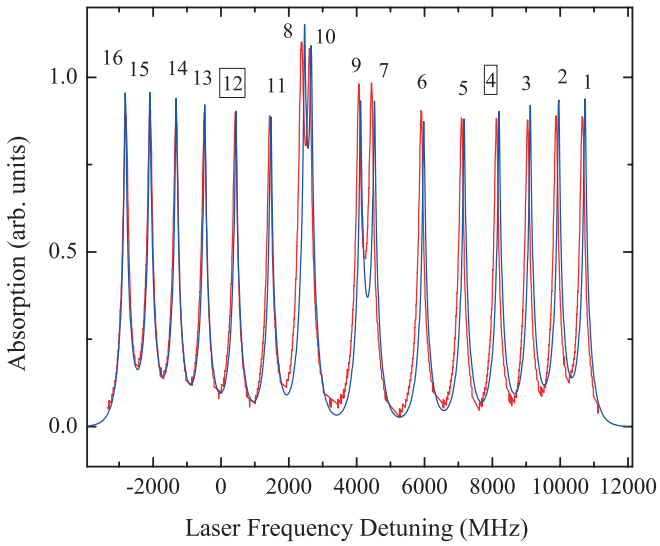

Figure 2.9: Cs D_2 line hyperfine structure absorption spectrum, $L = \lambda/2$ $B \approx 5650$ G, $P_L = 10\mu$W. The blue and red curves are theoretical and experimental results, respectively.

non-zero magnetic field with an increasing probability of the transition with B.

The absorption spectra for the atomic transitions $F_g = 4 \rightarrow F_e = 5$ at $B = 6800$ G magnetic fields are shown in Fig. 2.10. The red and the blue absorption spectra are the experimental and

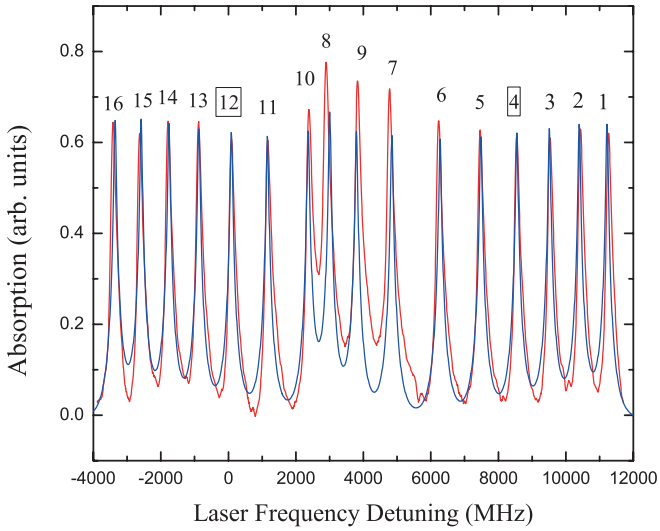

Figure 2.10: Cs D_2 line hyperfine structure absorption spectrum, $B = 6800$ G, $P_L = 6$ μW. The blue and red curves are theoretical and experimental results, respectively.

the theoretical results, respectively. Complete separation of the two groups of transition 1 - 8, 9-16 occur at $B > 8000$G (see Fig. 2.11). In order not to overload the Fig. 2.11, the transition

shifts dependence on magnetic field are presented only for the values $B = [4000 - 8000]$ G. The solid lines show the calculated values of 1 - 16 transition frequencies and the black squares represent the experimental results. The discrepancy between the theoretical and experimental results is less than 2 %.

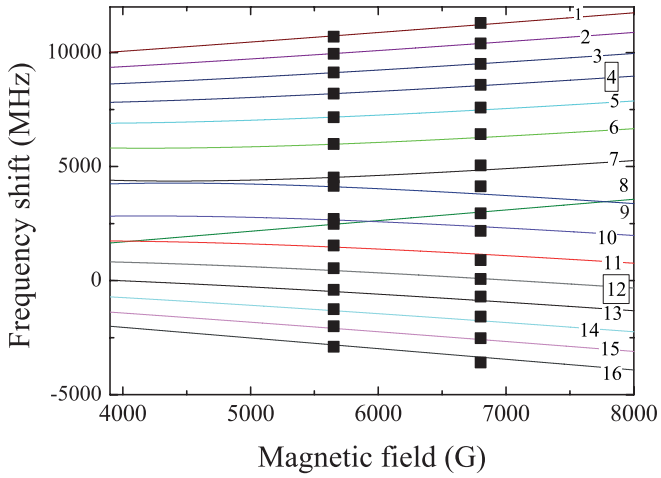

Figure 2.11: Comparison of the theoretical and the experimental results for Cs D_2 line: Solid lines are theoretical curves, squares depict the experimental results.

2.5 Summary

In this chapter, we have developed a theoretical model describing the resonant interaction of the laser light with the thin alkali vapor layer in the presence of an external static magnetic field. We show that due to a transient regime of interaction, only slow atoms contribute to the signal and their transmission spectrum is essentially Doppler-free. The nature of the obtained spectra makes the transmission spectroscopy from a nano-cell, a convenient technique to perform studies of closely-spaced atomic transitions and investigate their behavior in magnetic fields.

We have brought a brief description of the computational program, which calculates the transition frequency and intensity modifications while varying the magnetic field. We have shown that the linewidth of the absorption spectrum exhibits oscillating behavior (coherent Dicke narrowing) with a periodicity of λ. We have also performed the experimental studies of

Cs D lines hyperfine structure transitions for magnetic fields up to 6.8 kG, and we have shown an excellent agreement between experimental and theoretical absorption spectra.

Chapter 3

Faraday rotation

Contents

3.1 Overview of the phenomenon

In 1845 Michael Faraday discovered that when a plane-polarized light passes through a medium placed in a longitudinal magnetic field (applied in the direction of the radiation propagation) (see Fig. 3.1) a rotation of the polarization plane (Faraday rotation) occurs [68]. The Faraday rotation (FR) effect is used, in particular, in magnetometry to determine weak magnetic fields less than μG [69]. Also, narrow-band atomic optical filters (AOF) based on the FR effect have been used where only useful background free signal is transmitted when using crossed polarisers [70–72]. In addition, the linewidth of AOF absorption spectrum can be about three orders of magnitude smaller than that for available interference filters. A light compact optical isolator using the FR effect in Rb atomic vapor in the hyperfine Paschen-Back regime is presented in [73]. In [74], the FR effect is studied in strong magnetic fields for ^{87}Rb atomic vapor with the use of a millimeter-long cell, which nevertheless does not provide sub-Doppler resolution. It was shown in [75] that using thin garnet films doped with iron and applying the FR effect allows one to obtain an image of the domains of magnetic strips of credit cards.

It was shown in [76] that, the resonant Faraday effect with monochromatic light is a very promising method for measuring oscillator strengths.

It was shown earlier in [16, 26] that when using a spectroscopic cell with the thickness of atomic vapor column equal to a half-wavelength of the resonant optical radiation ($L = \lambda/2$), the absorption spectrum exhibits a significant sub-Doppler narrowing (by a factor of 3 or 4) as compared to ordinary cells with the length in the range of $L = 0.1 - 100$ mm, this is the manifestation of the Dicke-narrowing effect. This remarkable feature of nano-cells of thickness $L = \lambda/2$ allowed us to study the FR effect in atomic vapors using small ($\sim$ 1 G) magnetic fields [77,78]. It was also shown experimentally that the biggest rotation angle of the polarization plane is achieved exactly at this thickness of the atomic vapor column. The unusual behavior of optical processes, including the FR effect, in thin atomic layers was theoretically predicted in [9, 14].

In the present chapter, we present the experimental and theoretical studies of FR signal using a Cs vapor nano-cell of a half-wavelength thickness in magnetic fields (up to 6 kG). The fringe of the nano-cell filled with Cs vapor has a relatively large area at the thickness $L = \lambda/2 = 448$ nm that allows us to use a laser beam with a diameter of 1.5 mm and to form a narrow-linewidth FR signal. The latter is especially important for the identification of an individual atomic transition in case of strong magnetic fields, since there could be a spectral overlapping of a large number of FR components. In particular, the HPB regime on the Cs D_1 line is detected when using the FR effect. The effect has been observed in many solids, liquids, and gases. The amount of

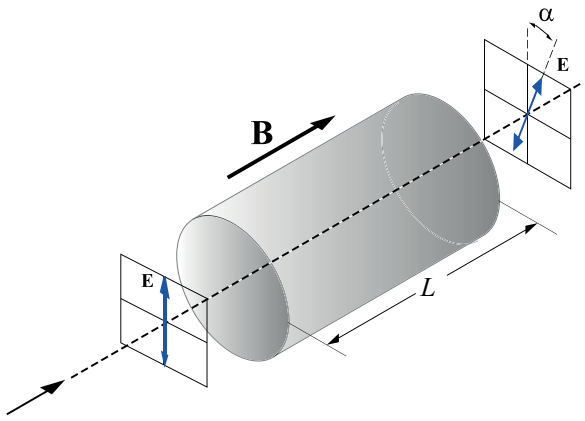

Figure 3.1: Rotation of the polarization plane when a plane-polarized light E passes through a medium in the presence of a longitudinal magnetic field B.

rotation α observed for any given substance is found by experiment to be proportional to the field strength $\mathbf{B}$ and to the length of the medium L.

$$\alpha = VBL, \tag{3.1}$$

where the V is the Verdet constant that is the amount of rotation per field unit and per length unit and depends on the material, the frequency and the temperature [79].

Let us give the explanation of the FR effect on the example of simple atomic level configuration $F_g = 1 \rightarrow F_e = 0$ which is illustrated in Fig. 3.2. In the absence of a magnetic field, energy

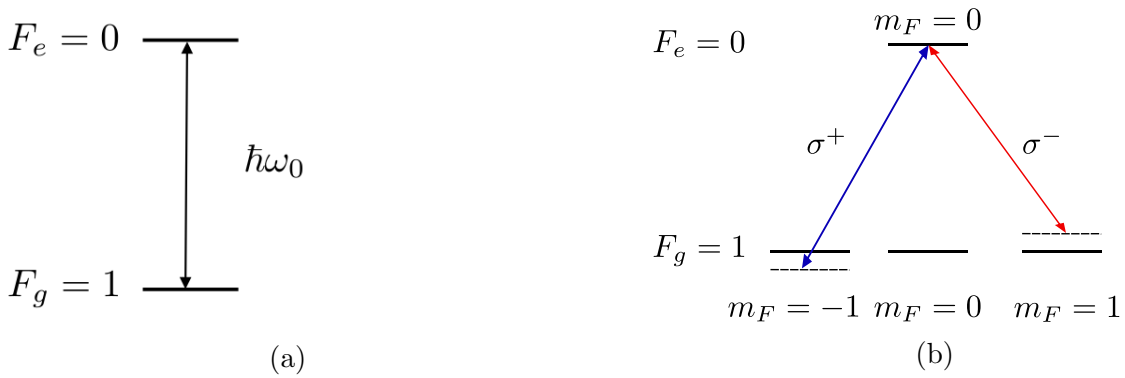

Figure 3.2: The splitting of atomic levels $F_g = 1 \rightarrow F_e = 0$ in the presence of magnetic field.

level degeneracy takes place and there exist only one transition between the ground and excited states. The applied magnetic fields produces $2F + 1$ spitings and shift of the energy levels and hence instead of the initial transition one has two transitions. This leads to a difference in resonance frequencies between left (σ^+) and right (σ^-) circularly polarized components of the linearly polarized light incident on the sample leading to a rotation of the radiation plane of polarization.

3.2 Modeling of Faraday rotation in thin atomic levels

In the following section we perform the study of the FR effect on the transmission of a plane wave through the NC of thickness L and deduce the rotation angle α. An arbitrary polarized plane wave $\mathbf{E}_{in}(z,t) = (\frac{1}{2}E_{in}e^{-i(\omega t - kz)} + c.c.)\mathbf{e}_E$ with angular frequency $\omega = 2\pi\nu$ and wavenumber $k = n\omega/c$, is directed at normal incident onto the nano-cell.

Let us consider a dielectric polarizable medium, where the electron (with rest mass m_e and charge $-e$), placed within an external magnetic field $\mathbf{B_0} = B_0\mathbf{e}_z$, interacts with the weak incident electromagnetic wave $\mathbf{E}_{in}(z,t)$. We assume that all atoms in the medium are identical and each of them has one active electron responding to the external field [80]. We treat the problem with a classical approach: the electron in the medium is considered as a classical particle obeying Newton's second law. We supposed that the velocity of the electron is sufficiently small to

neglect the influence of the oscillating magnetic field of the electromagnetic wave. Then equation of motion of the electron takes the form

$$m_e\ddot{\mathbf{r}} = m_e\omega_0^2\mathbf{r} - e\big(\tfrac{1}{2}E_{in}e^{-i(\omega t-kz)}\mathbf{e}_E + \frac{\mathbf{v}}{c}\times B_0\mathbf{e}_z\big). \tag{3.2}$$

We consider a trial solution of the form $\mathbf{r} = \mathbf{r}_0 e^{i(kz-\omega t)}$, in such a way the previous equation becomes

$$(\omega_0^2-\omega^2)\mathbf{r}_0 - \frac{i\omega eB_0}{m_e c}\mathbf{r}_0\times\mathbf{e}_z = -\frac{e}{m_e}\cdot\frac{1}{2}E_{in}\mathbf{e}_E. \tag{3.3}$$

One may decompose the field $\mathbf{E}_{in}$ on the basis vectors $\mathbf{e}_\pm$ such that

$$\mathbf{E}_{in} = E_{in}^+\mathbf{e}_- + E_{in}^-\mathbf{e}_+, \tag{3.4}$$

with $E_{in}^\pm = \dfrac{E_{inx}\pm iE_{iny}}{\sqrt{2}}$ and the basic vectors $\mathbf{e}_\pm = \dfrac{\mathbf{e}_x\pm i\mathbf{e}_y}{\sqrt{2}}$. Then the equation of motion reduces to

$$(\omega_0^2-\omega^2)\big(r_0^-\mathbf{e}_+ + r_0^+\mathbf{e}_-\big) + \omega\omega_L\big(r_0^-\mathbf{e}_+ + r_0^+\mathbf{e}_-\big) = -\frac{e}{m_e}\big(E_{in}^-\mathbf{e}_+ + E_{in}^+\mathbf{e}_-\big), \tag{3.5}$$

where $\omega_L = \dfrac{eB_0}{m_e c}$ is the Larmor frequency of an electron in the static magnetic field B_0. The equation (3.5) in the basis $\mathbf{e}_\pm$ does not mix the components $r_0^\pm$ [80], hence, we find the solution of form

$$r_{0\pm} = -\frac{e}{m_e}\frac{E_{in}^\pm}{\omega_0^2-\omega^2\mp\omega\omega_L}. \tag{3.6}$$

Then let us input the solution into the expression of the macroscopic polarization P of the medium, with number density N. Hence we get

$$\mathbf{P} = -Ne\mathbf{r} = -Ne\big(r_0^-\mathbf{e}_+ + r_0^+\mathbf{e}_-\big) \equiv \mathcal{P}^-\mathbf{e}_+ + \mathcal{P}^+\mathbf{e}_-, \tag{3.7}$$

where

$$\mathcal{P}^{\pm} = P^{\pm} e^{i(kz-wt)} = \frac{Ne^2}{m_e} \frac{E_{in}^{\pm} e^{i(kz-wt)}}{\omega_0^2 - \omega^2 \mp \omega\omega_L}. \tag{3.8}$$

The electric displacement field $\mathbf{D}_{in}$ is defined as

$$\mathbf{D}_{in} = \mathbf{E}_{in} + 4\pi\mathbf{P} = \left[(E_{in}^{-} + 4\pi P^{-})\mathbf{e}_{+} + (E_{in}^{+} + 4\pi P^{+})\mathbf{e}_{-}\right] e^{i(kz-\omega t)} = \left(\epsilon_{-} E_{in}^{-}\mathbf{e}_{+} + \epsilon_{+} E_{in}^{+}\mathbf{e}_{-}\right) e^{i(kz-\omega t)}, \tag{3.9}$$

where the dielectric constants $\epsilon_{\pm}$ are

$$\epsilon_{\pm} = 1 + \frac{4\pi \frac{Ne^2}{m_e}}{\omega_0^2 - \omega^2 \mp \omega\omega_L} = 1 + \frac{\omega_p^2}{\omega_0^2 - \omega^2 \mp \omega\omega_L}, \tag{3.10}$$

with plasma frequency of the medium $\omega_p = \sqrt{\dfrac{4\pi N e^2}{m_e}}$. The refractive indices of electromagnetic radiation are then equal to

$$n_{\pm} = \sqrt{\epsilon_{\pm}} \approx 1 + \frac{\omega_p^2}{2(\omega_0^2 - \omega^2 \mp \omega\omega_L)}. \tag{3.11}$$

The approximations is true for a low density gaseous medium ($n_{\pm} \approx 1$). The corresponding wavenumbers are

$$k_{\pm} = \frac{\omega n_{\pm}}{c}. \tag{3.12}$$

The latter means that the two components of the electric field travel along the z-direction with different velocities, after inserting (3.12) into (3.4) one gets

$$\mathbf{E_{in}} = E_{in}^{-} e^{i(k_{-}z-\omega t)}\mathbf{e}_{+} + E_{in}^{+} e^{i(k_{+}z-\omega t)}\mathbf{e}_{-}, \tag{3.13}$$

The waves $E_{in}^{-} e^{i(k_{-}z-\omega t)}\mathbf{e}_{+}$ and $E_{in}^{+} e^{i(k_{+}z-\omega t)}\mathbf{e}_{-}$ are labeled as left-handed and right-handed circularly polarized waves, respectively and propagate through a magnetized dielectric medium at

slightly different phase velocities.

In Fig. 3.1 the medium spreads from $z = 0$ to $z = L$. At the boundary $z = 0$, the electric field is

$$\mathbf{E}_{in}(z = 0) = E_{in} e^{i\omega t} \mathbf{e}_x, \tag{3.14}$$

which leads to $E_{in}^{+} = E_{in}^{-} = \frac{E_{in}}{\sqrt{2}}$. At the boundary $z = L$ the electric field takes the form

$$\begin{aligned}
\mathbf{E}_{out} \equiv \ \mathbf{E}_{in}(z = L) =& \frac{E_{in}}{\sqrt{2}} \left(e^{ik_- L} \mathbf{e}_+ + e^{ik_+ L} \mathbf{e}_- \right) e^{-i\omega t} \\
=& \frac{E_{in}}{2} \left((e^{ik_- L} + e^{ik_+ L}) \mathbf{e}_x + (e^{ik_- L} - e^{ik_+ L}) \mathbf{e}_y \right) e^{-i\omega t} \\
=& E_{in} \left(\cos \frac{\Delta n \omega L}{2c} \mathbf{e}_x + \sin \frac{\Delta n \omega L}{2c} \mathbf{e}_y \right) e^{-i(kL - \omega t + (n_{ave} - 1)\omega L/c)},
\end{aligned}$$

where

$$\Delta n = n_+ - n_- \approx \frac{\omega \omega_L \omega_p^2}{(\omega_0^2 - \omega^2)^2 - \omega^2 \omega_L^2}, \quad n_{ave} = \frac{n_+ + n_-}{2} \approx 1 + \frac{(\omega_0^2 - \omega^2)\omega_p^2}{2\left[(\omega_0^2 - \omega^2)^2 - \omega^2 \omega_L^2\right]}. \tag{3.15}$$

Then the rotation angle α of the plane of polarization is given by

$$\Delta\alpha = \frac{\Delta n \omega}{2c} L. \tag{3.16}$$

Recalling the relation between the angular frequency w and frequency ν, the rotation angle can be written as

$$\Delta\alpha = \frac{\pi(n_+ - n_-)L}{\lambda}. \tag{3.17}$$

where n_+ and n_- are the refractive indices for left and right circularly polarized radiations, respectively, L is the medium length and λ is the laser wavelength resonant with the media.

To calculte the profile of FR signal recorded from a nanocell is quite more difficult. Let us note that, if the difference of refractive indices seen by right and left hand polarizations is small

enough, then the intensity S_{FR} of the Faraday rotation signal can be approximated by [9]

$$S_{FR}(\omega) \approx \frac{2t_{10}t_{02}^2}{|F|^2} E_{in} \frac{\partial \Im m(I_T)}{\partial \omega}, \tag{3.18}$$

where the quantities $t_{10} = 2n/(n+1)$, $t_{02} = 2/(n+1)$, $F = 1 - r^2 \exp(2ikL)$ and $I_T = \left[1 + r^2 \exp(2ikL)\right] I_T^{lin} - 2rI_{SR}^{lin}$ have been derived in section 2.1.

3.3 Numerical simulations

As it was shown in in [9, 51] and was discussed in the previous section the spectral width and amplitude of absorption signal oscillate by varying the thickness of the cell. The presented theoretical model predicts the CDN-type dependence of the Cs D_1 line, $F_g = 4 \rightarrow F_e = 3, 4$ atomic transitions FR signal on the cell thickness. As for the absorption signal here also we study this dependence for thicknesses $L = \lambda/2$ to $L = 2\lambda$ with a step of $\lambda/2$. The numerical calculations of Cs D_1 line absorption spectra for atomic transitions $F_g = 4 \rightarrow F_e = 3, 4$ are presented in Fig. 3.3 when the thickness $L = \lambda/2 = 447.5$ nm (1), $L = \lambda = 895$ nm (2), $L = 3\lambda/2 = 1342.5$ nm (3), and when $L = 2\lambda = 1790$ nm (4). The amplitudes of these transitions are given by the oscillator strength factors $S_{43'} = 7/12$, $S_{44'} = 5/12$ (see [60] Eq. (41)).

3.3.1 Transition intensity and shift versus magnetic field

We are interested in studying the evolution of the transitions $F_g = 4 \rightarrow F_e = 3, 4$ for magnetic fields from 0 to 4 kG. In the formation of the FR signal both left and right hand circularly polarized radiation participate. We present the diagrams of the atomic transitions in Fig. 3.4. One may see that for weak magnetic fields there are 30 transitions (for σ^+ and σ^-) from which transitions labeled 1' - 14' are from $F_g = 4$ to$F_e = 3$ and transitions labelled 1 - 16 are from $F_g = 4$ to$F_e = 4$ levels. In the next step we have calculated the the transition frequency shift

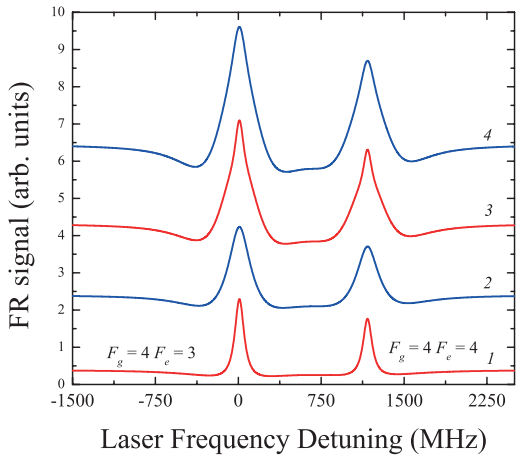

Figure 3.3: FR spectra of the Cs D_1 line $F_g = 4 \rightarrow F_e = 3, 4$ transitions at $B = 10$ G magnetic field for the thicknesses $L = \lambda/2 = 447.5$ nm (curve *1*), $L = \lambda = 895$ nm (curve *2*), $L = 3\lambda/2 = 1342.5$ nm (curve *3*), and $L = 2\lambda = 1790$ nm (curve *4*). For convenience, the curves have been shifted vertically.

and probabilities as a function of B and the results of numerical calculations are illustrated in Figs. 3.5 and 3.6.

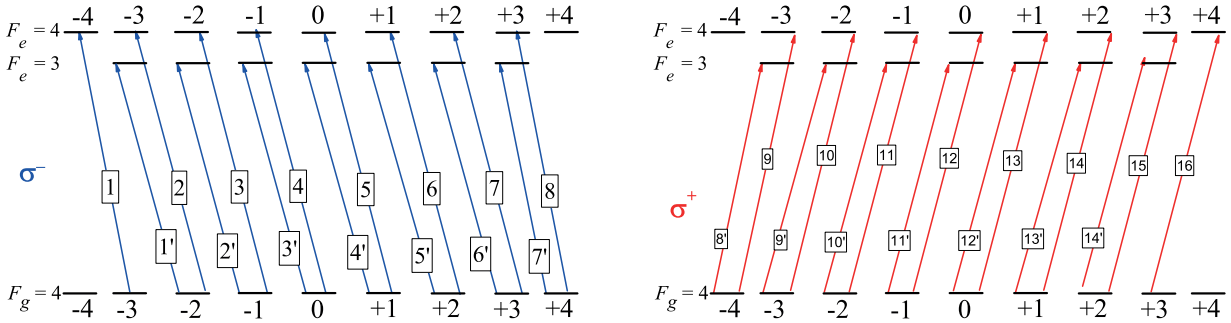

Figure 3.4: Diagram of the Cs D_1 line $F_g = 4 \rightarrow F_e = 3, 4$ atomic transitions in case of (a) σ^- and (b) σ^+ polarizations. The selection rules are (a) $\Delta F = 1; 0, \Delta m_F = -1$ and (b) $\Delta F = 1; 0, \Delta m_F = +1$.

The transition intensities are significantly different at weak magnetic fields, but tend asymptotically to two limit values with the increase of B. Transitions labeled 2 - 8, 10 -16, and 8' -15' tend to zero, meanwhile the transitions 1, 9, and 1' - 7' tend to a transition intensity of 0.16. Thus, from the initial 30 transitions only 9 remain in strong magnetic field. Note that in the case

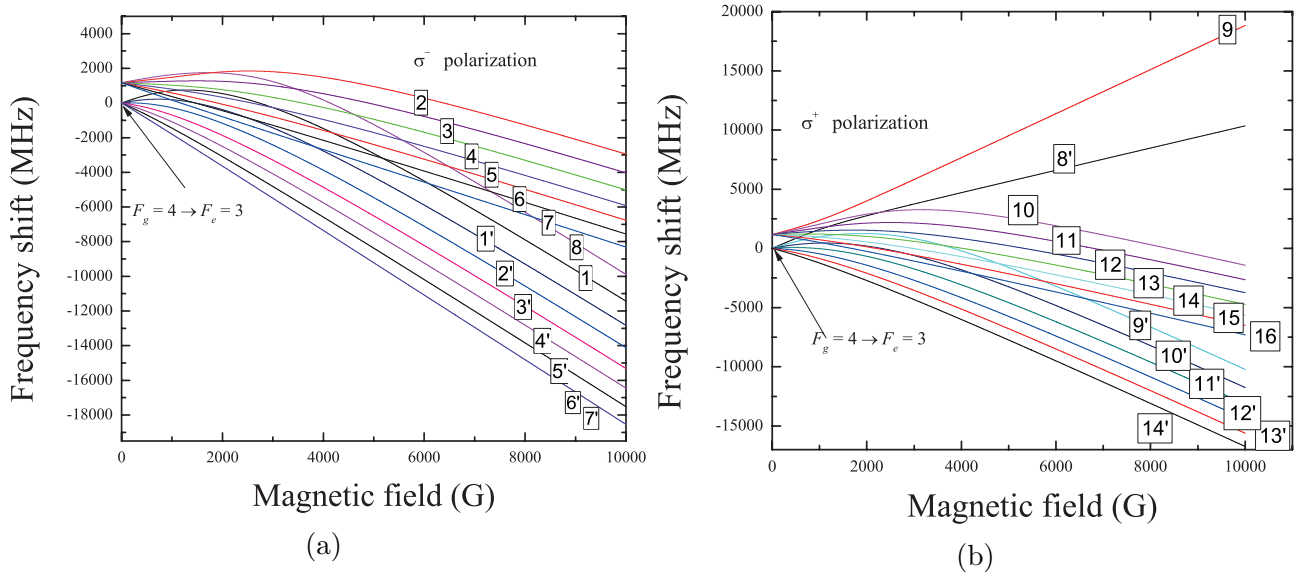

Figure 3.5: Cs D_1 line transition frequency shifts versus magnetic field in case of (a) σ^- and (b) σ^+ polarizations. The selection rules are (a) $\Delta F = 1; 0, \Delta m_F = -1$ and (b) $\Delta F = 1; 0, \Delta m_F = +1$.

of strong magnetic fields and circular polarized radiation from transitions $F_g = 3, 4 \rightarrow F_e = 3, 4$ it remain only 16 transitions. They form two groups of eight atomic transitions for each polarization; as demonstrated in [81].

3.3.2 Evolution of $F_g = 4 \rightarrow F_e = 3, 4$ transitions in magnetic fields

In this section, we study the evolution of $F_g = 4 \rightarrow F_e = 3, 4$ transitions in magnetic fields for the thickness $L = \lambda/2$. The results of the numerical calculations are illustrated in Fig. 3.7. Magnetic field B increases upward and amounts to $B = 500$, 1500, 2400, 4000 G in the spectra labeled $1, 2, 3, 4$, respectively. One may see that in the spectrum labeled 1 the atomic transition are close in frequency and are partly overlapped. It is important to note that with the increase of the magnetic field, atomic transitions become equidistant, which is the manifestation of the hyperfine Paschen-Back regime and tend to the high-frequency part of the spectrum (positive frequency shift). The HPB regime for the Cs atoms begins with fields $B \gg 1700$ G.

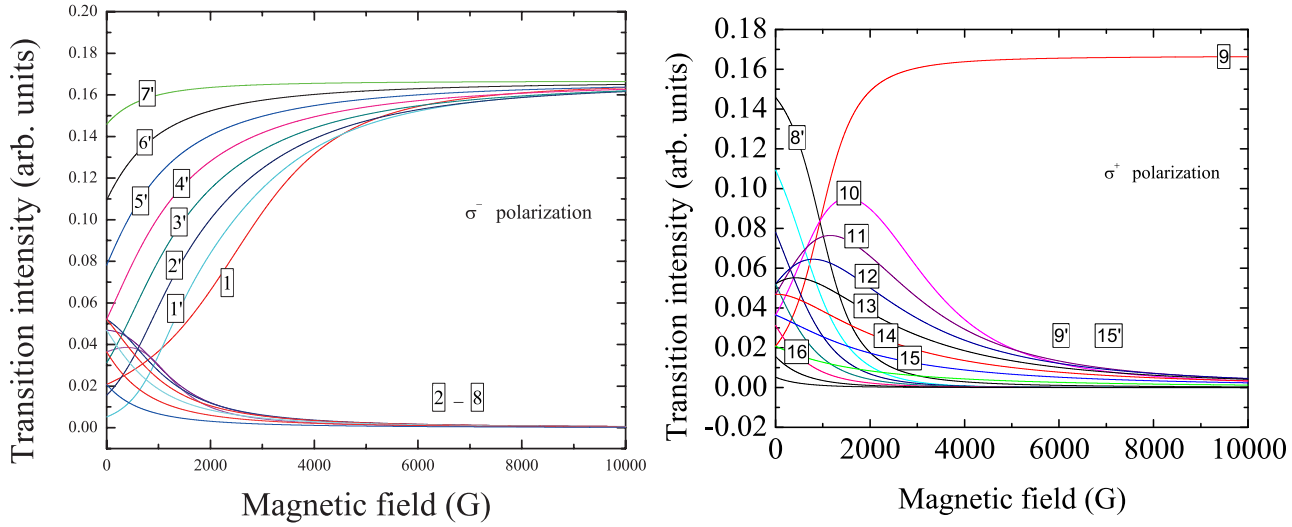

Figure 3.6: Cs D_1 line transition probabilities versus magnetic field in case of (a) σ^- and (b) σ^+ polarizations. The selection rules are (a) $\Delta F = 1; 0, \Delta m_F = -1$ and (b) $\Delta F = 1; 0, \Delta m_F = +1$.

3.4 Features of Faraday rotation effect in Cs D_1 line

The scheme of the experimental setup is shown in Fig 3.8. A continuous wave extended cavity diode laser, with a power of several mW and a spectral linewidth $\Delta\nu_L$ <1MHz is used. The laser with a wavelength $\lambda = 895$ nm is in resonance with the Cs D_1 line. The laser frequency is scanned across the Cs D_1 line resonances. The laser radiation when passing through the Glan-Taylor polariser P_1 becomes linearly polarized. The second polariser (analyser) P_2 is placed at the output of the medium and is oriented to be crossed with the first one. In the absence of a magnetic field, the linearly polarized radiation does not pass through the analyser P_2 and the signal on the photodetector 3 is absent. The NC with Cs vapors is placed between Helmholtz coils (not shown in the figure) to produce a magnetic field B along the direction of the laser radiation propagation. In this case, the plane of polarization will rotate and a FR signal is detected by the photodetector 3. The maximum value of the magnetic field that could be produced with the help of the Helmholtz coils is 220 G. To form stronger magnetic fields, a permanent magnet (PM) in the form of a disk with a diameter of 50 mm and a thickness of 25 mm, having a hole in the center with a diameter of 4 mm for the passage of the laser radiation, is used. The

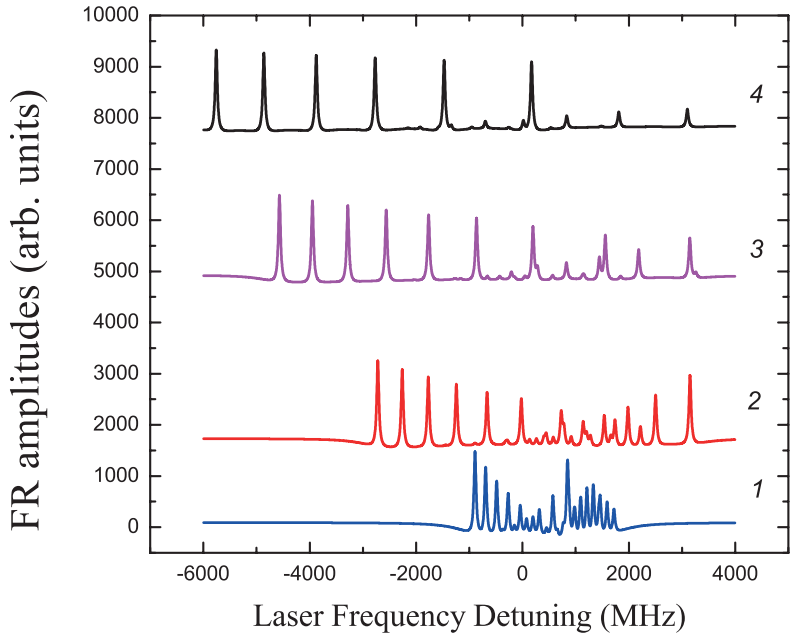

Figure 3.7: Evolution of Cs D_1 line $F_g = 4 \rightarrow F_e = 3, 4$ atomic transitions for $B = 500$ G (1), $B = 1500$ G (2), $B = 2400$ G (3), and for $B = 4000$ G (4).

magnetic field is varied in the range of 1 to 4 kG by changing the distance between the PM and the NC from 60 to 15 mm. The PM creates a gradient magnetic field, however, because of the small thickness of the Cs vapor ($\sim$ 450 nm), the change of the magnetic field within the atomic vapor column is of ~ 0.1 G. Consequently, relatively to its value, the magnetic field in the NC can be considered as being homogeneous. To form a frequency reference, a part of the laser radiation is directed to an additional long Cs cell of thickness $L = 30$ mm where a saturated absorption spectrum is produced. In this section we are going to study the FR effect in Cs D_1 line for different values of magnetic field. Note that all the experimental spectra were recorded for the same thickness of the nano-cell $L = 448$ nm and for the same power of the laser $P = 0.2$ mW, only the value of the applied magnetic field has been changed. In weak magnetic fields, where the splitting of the atomic levels is described by the total angular momentum of the atom $\mathbf{F} = \mathbf{J} + \mathbf{I}$ and its projections m_F, for atomic transitions between the ground F_g and excited F_e states of Cs D_1 line and for circularly σ^+ and σ^- polarized radiation the following selection rules: $F_e - F_g = \Delta F = 0, \pm 1$, $m_{Fe} - m_{Fg} = \Delta m_F = \pm 1$ (for $\sigma^\pm$ radiations respectively) must be

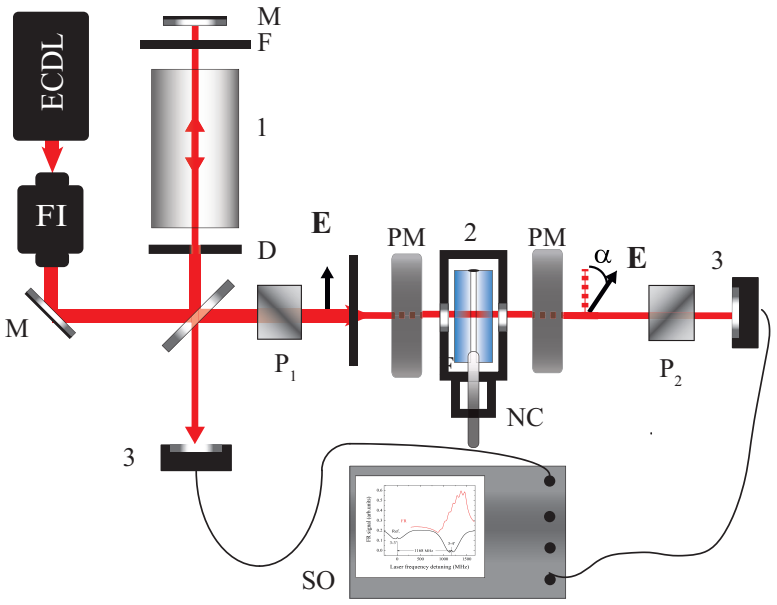

Figure 3.8: Sketch of the experimental setup. The laser produced by ECDL; FI - optical insulator; P_1, P_2 - Glan-Taylor polarizers; F - filter; D -diaphragm; M - mirror; SO - digital storage oscilloscope; 1- frequency reference unit;. 2 - NC filled with Rb or Cs or K and placed inside the oven; PM - permanent strong ring magnets; 3 - photodetectors; α - rotation angle of the polarization plane.

fulfilled (see the diagrams presented in Fig. 3.9). It is seen from Fig. 3.9a, that the σ^+ and σ^- radiations form seven V–pairs of transitions between $F_g = 3 \to F_e = 4$ levels and, as a result, the FR spectrum contains seven components labeled ①–⑦. The diagram of $F_g = 4 \to F_e = 3$ atomic transition is presented in Fig. 3.9b. In this case the σ^+ and σ^- radiations form seven Λ–pairs of transitions labeled $1' - 7'$.

Figure 3.10 presents the FR spectra for the transitions $F_g = 3 \to F_e = 4$ and $F_g = 4 \to F_e = 3$ at the longitudinal magnetic field 200 G. The upper and the middle curves are, respectively, the theoretical and experimental FR spectra, while the lower curve is the frequency reference. It can be seen that the theoretical and experimental spectra are in good agreement. The location of the resonances in frequency and the heights of resonances are well described by the theoretic model. Due to the small thickness L of the nano-cell, the rotation angle α is $\sim 10^{-2}$ rad. Figure 3.11 shows the calculated dependence of the frequency shifts of the transition $F_g = 3 \to F_e = 4$ versus the magnetic field. The FR spectra for the atomic transition $F_g = 3, 4 \to F_e = 4$ in case

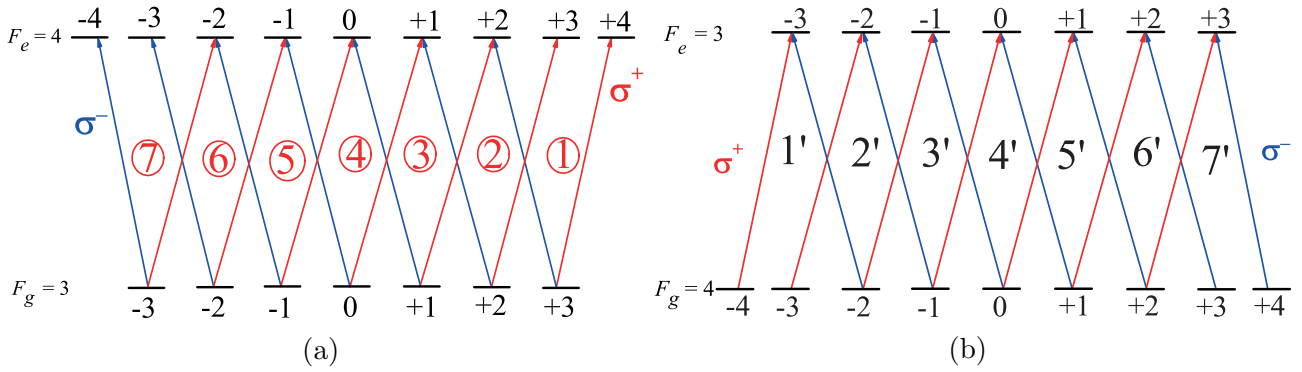

Figure 3.9: Diagram of the Cs D_1 line (a) $F_g = 3 \to F_e = 4$ and(b) $F_g = 4 \to F_e = 3$ atomic transitions in the case of circularly σ^+ and σ^- polarized radiations. The selection rules are: $F_e - F_g = \Delta F = 0, \pm 1$, $m_{Fe} - m_{Fg} = \Delta m_F = \pm 1$ (for $\sigma^\pm$ radiations, respectively). It can also be seen from the diagrams, that the circular radiations σ^+ and σ^- form seven $V(\Lambda)$– pairs of transitions and in the FR spectrum there must be seven components

of the magnetic field $B = 2300$ G are shown in Fig. 3.12. The upper and the middle curves show the theoretical and experimental spectra, respectively. The inset in Fig. 3.12b shows the diagram of the group of atomic transitions $F_g = 4 \to F_e = 4$ having the biggest probabilities. As it is seen, the component labelled ⑧ (arising from the atomic transition $F_g = 4 \to F_e = 4$) at $B \approx 2300$ G is located far into the low-frequency wing and is not present at the recorded spectrum. However, when the laser frequency is detuned into the low-frequency region, the component labelled ⑧ is also detected.

As shown below, for ^{133}Cs atoms ($I = 7/2$) at magnetic fields $B > B_0$(Cs) with B_0(Cs) = 1.7 kG, the decoupling between the nuclear magnetic, **I**, and the total electronic, **J**, angular momenta begins, and the splitting of the atomic levels is described by the projections m_J and m_I [66, 67, 82, 83].

The diagram for Cs D_1 line transitions, in the case of HPB regime, is shown in Fig. 3.13. There are eight atomic transitions that satisfy the selection rules $\Delta m_I = 0$ and $\Delta m_J = 1$ in the case of circular σ^+ radiation. In the case of σ^- radiation there are also eight transitions between ground $m_J = +1/2$ and excited $m_J = -1/2$ levels. The upper curve in Fig. 3.14 shows the theoretical spectrum of the FR signal containing all eight components. The middle curve corresponding to the experimental spectrum of the FR signal contains only the components labeled ⑥ – ⑧.

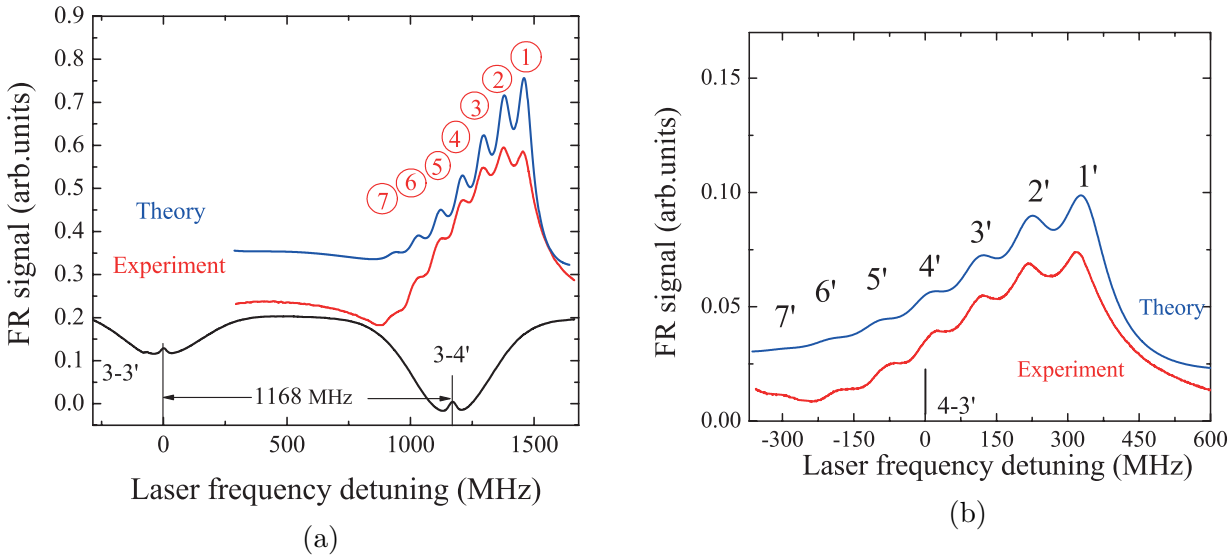

Figure 3.10: Cs D_1 line Faraday rotation spectra for (a) $F_g = 3 \rightarrow F_e = 4$ transitions and for (b) $F_g = 4 \rightarrow F_e = 3$ transitions for the applied magnetic field $B = 200$ G. Upper curve – theoretical spectrum, middle curve – experimental spectrum, lower curve – the reference spectrum. Seven FR components are clearly visible.

This is explained by the fact that diode lasers at the wavelength of 895 nm, as a rule, have a small tuning range of ~ 5 GHz. This is why we present only the most important part of the spectrum containing the FR signal component labelled ⑧. When the laser is re-aligned and the laser frequency tuning range is changed, all other components of the signal, ① – ⑤ , are detected (however, we did not want to present the spectra partially).

With a further increase of the magnetic field B, the eight FR components remain in the spectra while their frequencies increase and the frequency interval between the components tends to the same value, which means that they become equidistant. Note that for convenience, we have shown only FR components ① – ⑧ located in the high-frequency region (see Fig. 3.14), while a similar FR spectrum consisting of eight FR signals exists also in the low-frequency region and the frequency separation between the two groups is ~ 10 GHz.

To produce strong magnetic fields B (6 kG), we used the system presented in [81]. The assembly consists of two strong permanent ring magnets mounted on a 50×50 mm^2 cross section Π–shaped holder made from soft stainless steel. The system with small inlet and outlet radiation holes

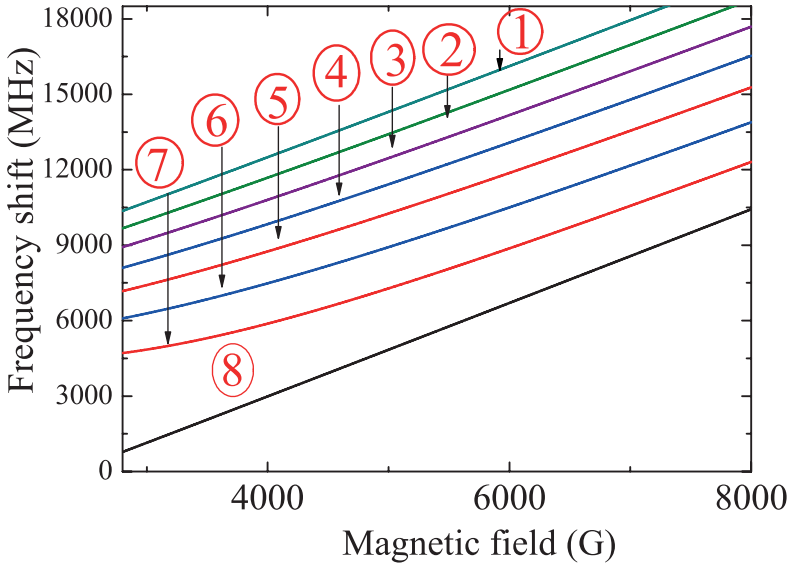

Figure 3.11: The diagram of Cs D_1 line HPB regime (for σ^+ radiation) with the transitions ①–⑧ satisfying the selection rules (see the text).

was designed for the transmission of a small diameter laser beam, and thus was not suitable for the use of the SR technique (the SR technique allows one to provide successful sub-Doppler resolution of atomic transitions [81]). Meanwhile the assembly with strong magnets is suitable for the FR technique, which is an advantage over the SR technique.

3.5 Faraday effect in rubidium atomic layers thinner than 100 nm

The preliminary results show that spectrum of the FR signal is well detectable for the Rb atomic vapor column thickness $L < 100$ nm. The peak in the spectrum of the FR signal is shifted to the red region and a strong asymmetric low-frequency wing appears (as compared to the high-frequency wing) owing to the van der Waals (vdW) interaction of Rb atoms with the windows of the NC.

It is demonstrated in [84], that the angle of FR for the transitions that have the same atomic total angular momentum F for the ground and the excited levels, particularly, ^{85}Rb, D_1 line

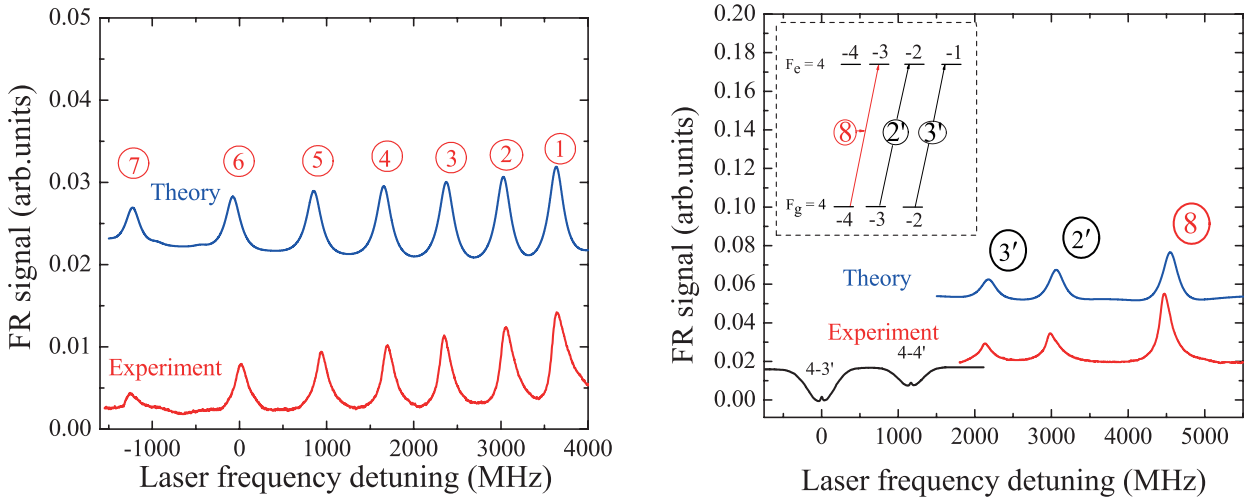

Figure 3.12: Cs D_1 line Faraday rotation spectra for (a) $F_g = 3 \rightarrow F_e = 4$ transitions and for (b) $F_g = 4 \rightarrow F_e = 4$ transitions at $B = 2.3$ kG applied magnetic field. Upper curve – theoretical spectrum, middle – the experimental spectrum, lover curve – the reference spectrum. The inset shows diagram of the group of $F_g = 4 \rightarrow F_e = 4$ transitions which have the biggest probabilities. For simplicity, the insets with the pairs of transitions formed by the circular σ^+ and σ^- radiations are not shown.

transition $F_g = 3 \rightarrow F_e = 3$, is much smaller than that for $F_g = 3 \rightarrow F_e = 2$. This allows one to avoid the spectral overlapping of the strongly broadened transition $F_g = 3 \rightarrow F_e = 2$ (the vdW broadening for $L \sim 40$ nm could reach ~ 0.8 GHz (see Ref. [85]) with the transition $F_g = 3 \rightarrow F_e = 3$ (the frequency separation is of 360 MHz, which is smaller by a factor of 2 -3 than the broadening). This allows one to study the vdW interaction more accurately than it could be provided by the use of other techniques, such as selective reflection or absorption (see Figures 4 and 7 in [85]). In this section we will study the interaction of Rb atom and dielectric surface vdW interaction for thicknesses $L = 40 - 100$ nm.

The experimental setup used for obtaining results in this section is similar to the one already described in 3.4. We used the radiations of continuous narrow-band external cavity diode lasers with wavelengths $L = 795$ nm (D_1 line of Rb) and $L = 780$ nm (D_2 line of Rb) and a linewidth $\Delta\nu_L \sim 1$ MHz. The NC was placed in the center of a pair of Helmholtz coils. In order to form a frequency reference (Ref.) a part of the laser radiation was directed to the Rb cell, with $L = 30$

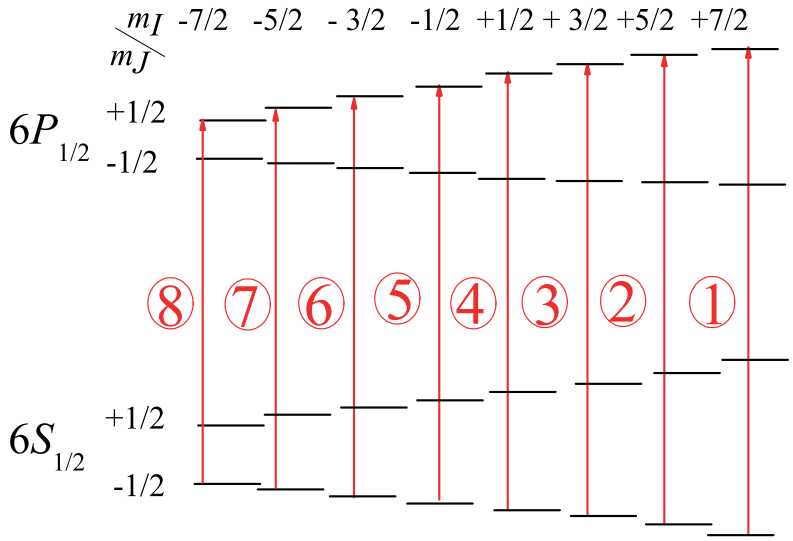

Figure 3.13: The diagram of Cs D_1 line HPB regime (for σ^+ radiation) with the transitions ① – ⑧ satisfying the selection rules (see the text).

mm to form a saturated absorption (SA) spectrum. All the remaining details do not defer from the setup used for detecting the Faraday rotation signal presented before.

3.5.1 D_1 line

Figure 3.15 shows the FR signal spectra on the exit of the second crossed Glan polarizer (P2) when the nano-cell thickness changes from 398 nm (curve 1) to 40 nm (curve 5), the applied magnetic value is $B = 15$ G and the nano-cell reservoir temperature is 160 °C, which corresponds to a density $N_{Rb} \approx 10^{14}$ cm^{-3}. Curve 1 was obtained at $L = \lambda/2 = 398$ nm, where the FR rotation is angle maximal over the entire thickness range 0.1 - 1 μm [45, 78]. The vapor column thickness was determined by the method described in [45]. The curve *Ref.* demonstrates the unshifted (reference) positions of the ^{87}Rb, $F_g = 2 \rightarrow F_e = 2$ and ^{85}Rb, $F_g = 3 \rightarrow F_e = 2, 3$ transition frequencies. It is seen in the Fig. 3.15 that curve 1 does not experience the vdW shift, whose absence is explained by a relatively large distance between atoms and the NC windows. The experimental results are consistent with the theoretical demonstation presented in [84]. It is seen in Fig. 3.15 that for the curve 1 the FR signal is substantially lower for the ^{85}Rb, $F_g = 3 \rightarrow F_e = 3$ transition. As for the FR spectrum at the thickness smaller than 70 nm,

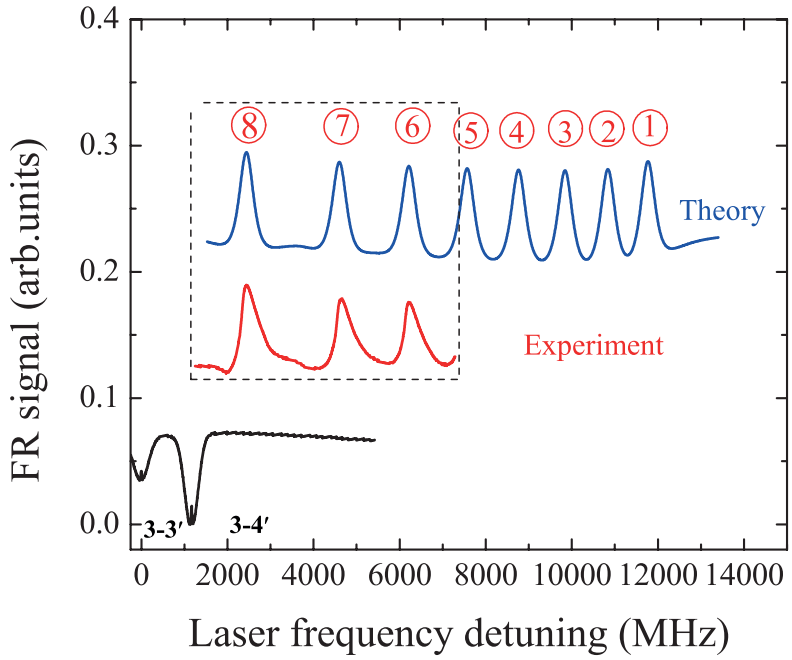

Figure 3.14: Cs D_1 line Faraday rotation spectra for $F_g = 3 \rightarrow F_e = 4$ at $B = 6$ kG applied magnetic field. The upper curve – the theoretical spectrum, the middle – the experimental spectrum, the lower curve – the reference spectrum. The insets show the diagram of Cs D_1 line HPB regime (for σ^+ radiation) with the transitions ①–⑧ satisfying the selection rules (see the text).

the low-frequency wing of the ^{85}Rb $F_g = 3 \rightarrow F_e = 3$ transition does not impact on the ^{85}Rb, $F_g = 3 \rightarrow F_e = 2$ transition. The latter speaks about the obvious advantage of using the FR signal. It is important to note that on the absorption spectra these two transitions are close in frequency leading to the strong overlapping of their wings, which complicated the study of an individual transition [37].

Figure 3.15 shows that the decrease in thickness L leads to the red frequency shift of the FR peak and to a strong asymmetric broadening toward low frequencies caused by the atoms -NC walls (windows) vdW interaction [86]. Note that curves *2* - *5* are well approximated by the following envelopes: the high-frequency wing is approximated by a Gaussian, and the low-frequency wing by a Voigt function (*i.e.*, the convolution of Gaussian and Lorentzian functions). Curve *3* shows an approximating envelope (heavy pink curve) superimposed on the experimental one (black curve).

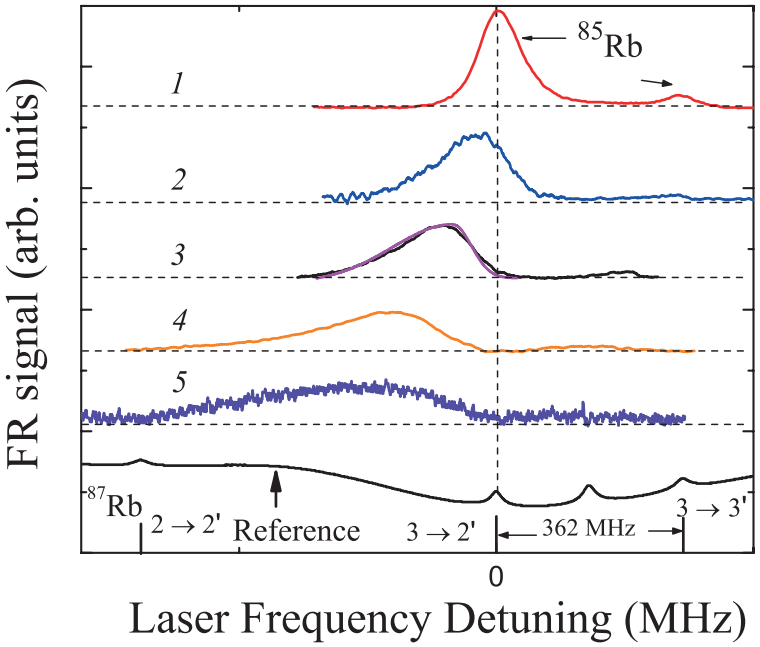

Figure 3.15: ^{85}Rb D_1 line FR spectra for different values of cell thickness at $B = 15$ G: *(1)* $L = 398$ nm, no frequency shift; *(2)* $L = 80 \pm 2$ nm, red frequency shift of - 30 MHz; *(3)* $L = 57 \pm 2$ nm, red shift of - 100 MHz; *(4)* $L = 46 \pm 2$ nm, red shift of - 190 MHz; and *(5)* $L = 40 \pm 2$ nm, red frequency shift of - 250 MHz. The lower curve Ref is the SA-based frequency reference. For convenience, the curves have been shifted vertically.

When assuming that the atom interacts with only one of the windows (let us chose the w_1) the vdW interaction produces a potential $\Delta\nu_{vdW} = -C_3/z_1^3$, where the C_3 coefficient depends on the atomic state and on the surface. A positive C_3 coefficient implies an attractive interaction (red frequency shift). In a NC the atom experiences two potentials produced by each window, which for a NC thickness $L < \lambda/2\pi$ causes a shift of the form (also see [87])

$$\Delta\nu_{vdW} = -\frac{C_3}{z^3} - \frac{C_3}{(L-z)^3}, \tag{3.19}$$

that is plotted in Fig. 3.16. For the atoms located in the center of the NC ($z = L/2$) the total frequency shift is

$$\Delta\nu_{vdW} = -16C_3/L^3. \tag{3.20}$$

The atoms which are located at $(L/2) \pm 5$ nm will form the radiation with the frequencies which

are spread in the frequency interval of ∼30 MHz, while the atoms which are located at $(L/4)\pm5$ nm will form the radiation with the frequencies which are spread in the frequency interval of ≈ 5000 MHz. Since the similar contribution as it is for thickness $L/4$ comes from thichkness $L/4$, that is why the spectral density of the peak in the vdW spectrum for the atoms located nearly at the $L/2$ will be 80 times bigger than that for the atoms located nearly at the $L/4$ and nearly at $3L/4$. It is assumed that the distribution of the atoms in the nano-cell is uniform. Using the frequency shift of the FR signal peak (at a density $N_{Rb} \approx 10^{14}$ cm^{-3}; see Fig. 3.16) and Eq. 3.20 we get $C_3 = 1.2 \pm 0.2$ kHz $\cdot\mu$m^3 for the vdW interaction coefficient C_3 for the Rb atoms (D_1 line transitions) with the sapphire windows, and this value agrees well with that obtained in [35,88].

Keaveney in [88] showed that at a NC thickness $L > 200$ nm when increasing the the side-arm

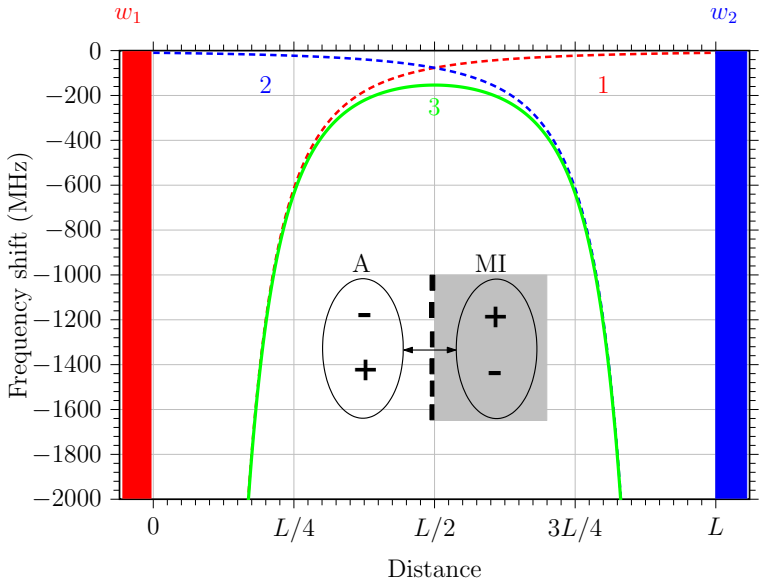

Figure 3.16: Red frequency shift (1) is caused by the nano-cell window w_1 and red frequency shift (2) is caused by nano-cell window w_2. The inter-window distance is $L = 50$ nm. The total frequency shift (3) is caused by windows w_1 and w_2. The atom A (in the form of a dipole) and its mirror image (MI) in an insulator (nano-cell window) are schematically shown in the inset.

temperature (*i.e.*, increasing Rb atomic density) neither spectral broadening nor transition frequency shift occur due to the Rb-Rb atomic interaction. The situation is substantially different at thicknesses $L \leqslant 100$ nm: as the temperature increases from 170 to 208 °C, an additional red frequency shift takes place (see Fig. 3.17). In this case of $N_{Rb}k^{-3} \geqslant 1$ (where k is the

wavenumber) a strong dipole-dipole interaction of Rb atoms takes place. This finds support in [35], where a red shift in the absorption spectrum of Rb atoms (D_2 line) at thickness of 90 nm is detected when increasing the temperature. Note that, to minimize the influence of the Rb-Rb interaction, we have to measure the red shift of the FR signal peak at very low densities, where the condition $N_{Rb}k^{-3} \ll 1$ is met. Low densities can be achieved at a NC reservoir temperature of 140 °C ($N = 4 \times 10^{13}$ cm^{-3}). A decrease of the temperature at a thickness of 40 to 80 nm unfavorably affects the signal-to-noise ratio and, hence, the accuracy of determining the position of the FR peak. At $T = 140$ °C, the red shift decreases by $\approx 10\%$. The related correction for the coefficient C_3 is smaller than the error given in [88] ($\approx 30\%$). Increasing the FR signal by increasing the magnetic field is unacceptable, since a strong symmetric broadening of the signal takes place in magnetic fields higher than 20 G [89]; this broadening distorts the FR spectrum caused by the vdW interaction of atoms with the NC windows. Therefore, the only acceptable parameter for increasing the signal to the level to be reliably detected is a moderate increase in the atomic density.

3.5.2 D_2 line

To study the influence of the van der Waals effect on the D_2 line spectrum at thicknesses $L \leq 100$ nm, we chose the ^{87}Rb $F_g = 2 \rightarrow F_e = 1, 2, 3$ transitions since the frequency intervals between the hyperfine structure upper levels $F_e = 1, 2, 3$ are maximal. The latter is important for diminishing the overlapping in strongly broadened spectra. Figure 3.18 shows the FR spectra when thickness L decreases from 390 nm (curve *1*) to 60 nm (curve *4*) in a magnetic field $B = 10$ G at a nano-cell reservoir temperature of 160 °C. The lower Ref curve shows the unshifted positions of the ^{87}Rb, $F_g = 2 \rightarrow F_e = 1, 2, 3$ atomic transitions. As is seen in Fig. 3.18, the FR spectrum narrows strongly (FWHM $\approx$ 40 MHz) at a thickness $L = \lambda/2 = 390$ nm, no red shift is detected and all the transitions are fully spectrally resolved. The red shift is observed at a thickness of 100, 75, or 60 nm. Using the Eq.(3.20) for the D_2 line of Rb we have

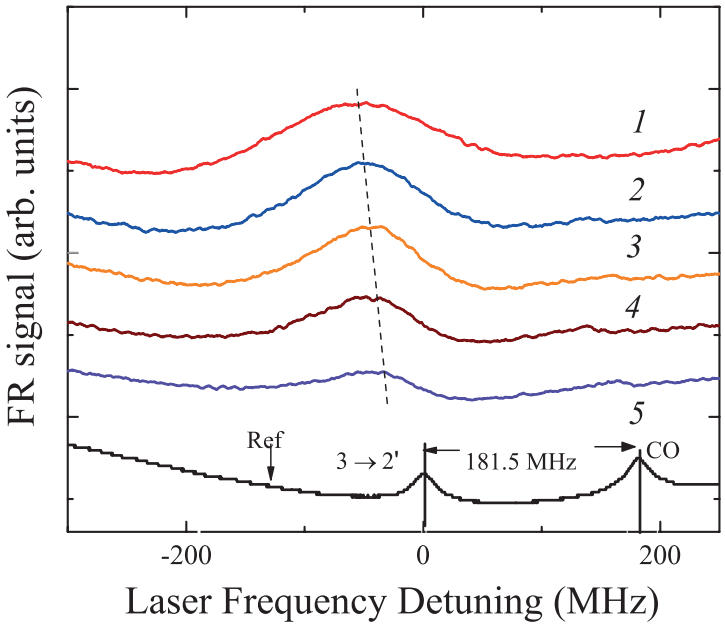

Figure 3.17: Faraday Rotation spectra of the ^{85}Rb D_1 line $F_g = 3 \rightarrow F_e = 2, 3$ transitions at $B = 15$ G, $L = 398$ nm, no frequency shift *(1)*; $L = 80 \pm 2$ nm, red frequency shift of - 30 MHz *(2)*; $L = 57 \pm 2$ nm, red shift of - 100 MHz *(3)*; $L = 46 \pm 2$ nm, red shift of - 190 MHz *(4)*; and $L = 40 \pm 2$ nm, red frequency shift of - 250 MHz *(5)* . The lower curve REF is the SA-based frequency reference. For convenience, the curves have been shifted vertically.

$\Delta\nu_{vdW} = 1.6 \pm 0.2$ kHz·μm^3, which agrees well with the value given in [37, 90]. A bigger value of the coefficient C_3 in the case of the D_2 line was predicted in [91]. At NC thicknesses $L \leq 100$ nm (as in the case of D_1 line), an additional red shift occurs when the temperature increases from 160 °C ($N_{Rb} \approx 10^{14}$ cm^{-3}) to 240°C ($N_{Rb} \approx 2 \times 10^{15}$cm^{-3}) due to the Rb-Rb interaction (see Fig. 3.19). Note that the behavior of the atomic transition frequency when the alkali metal atom vapor density increases under rigid spatial confinement by the nano-cell windows is being actively studied, since new specific features have been revealed. For example, the following unusual behavior of the D_2 line frequency of the atomic transition in potassium at a nano-cell thickness $L = 490$ nm was revealed recently in [92], where a theoretical calculation based on the cooperative effect was performed. A blue frequency shift was detected when the potassium atom density increased, and the frequency shift became zero (i.e., the transition frequency coincides with the initial frequency) when the atomic density increased further.

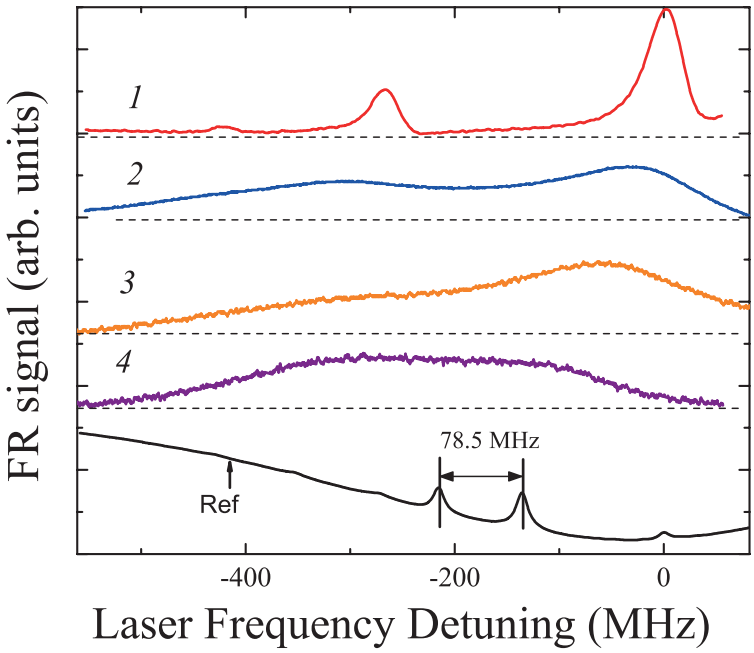

Figure 3.18: FR spectra vs NC thickness at $B = 10$ G: *(1)* $L = 390$ nm, no frequency shift; *(2)* $L = 100 \pm 2$ nm, red frequency shift of - 30 MHz; *(3)* $L = 75 \pm 2$ nm, red shift of - 57 MHz; *(4)* $L = 60 \pm 2$ nm, red shift of - 120 MHz. A further decrease of L is unreasonable since a strong overlapping of the spectra takes place. The lower curve Ref is the SA-based frequency reference. For convenience, the curves have been shifted vertically.

3.6 Application of the FR effect in magnetic field measurements

Figure 3.20 shows the FR signal (D_1 line) spectrum in a longitudinal magnetic field of $B = 2300$ G at a thickness $L = 70$ nm. We present the high-frequency wing, which was recorded using circular σ^+-polarized laser radiation. At magnetic field $B = 2300$ G the splitting of atomic levels is described by m_J and m_I. In this case, in the D_1 line of Rb ten atomic transitions are retained, from which six atomic transitions (labeled 4 - 9 in the right inset in Fig. 3.20) for the ^{85}Rb and four transitions for ^{87}Rb (1 - 3, 10 in the left inset in Fig. 3.20). Although the atomic transitions are strongly broadened because of the vdW effect, the peaks are well pronounced. The magnetic field can be measured by the following two methods: (i) from the frequency shift of transition 1 with respect to the reference frequency; however, it is necessary to take into

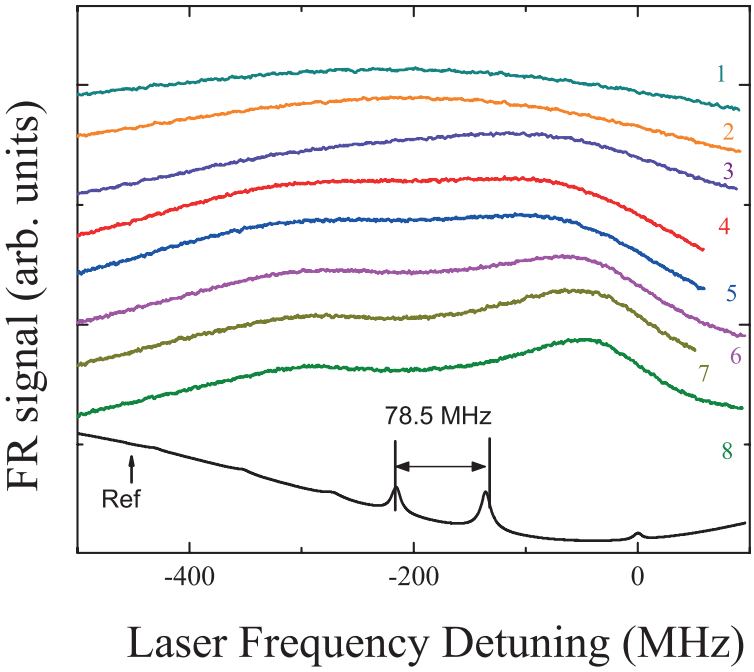

Figure 3.19: Temperature dependence on the shift of the ^{87}Rb D_2 line $F_g = 3 \rightarrow F_e = 2$ transitions Faraday Rotation spectra: $T = 240$ °C *(1)*, 220 °C *(2)*, 210 °C *(3)*, 200 °C *(4)*, 195 °C *(5)*, 178 °C *(6)*, 174 °C *(7)*, 162 °C *(8)*. The lower Ref curve is the SA based frequency reference.

account the additional frequency shift induced by the vdW interaction in this case; (ii) (more convenient method) to determine the ratio a/b as a function of B, where a is the frequency spacing between transitions 1 and 10 of ^{87}Rb and b is the frequency spacing between transitions 1 and 2 (see Fig. 3.20). Note that the vdW-induced red shift is the same for these transitions. The ratio a/b as a function of B is given in Fig. 5 (within 5%) in [85]. Note that a frequency reference spectrum is not required in this case. Thus, using a FR spectrum, we can determine magnetic fields with a spatial resolution of 70 nm and, hence, can measure both homogeneous and strongly gradient magnetic fields. The experimental data demonstrate that analogous FR spectra are recorded up to a magnetic field of 8 kG, and the only difference is that the frequency shifts increase strongly to several GHz. Note that the authors of [2] (Fig. 5) studied FR in pairs of Na atoms in cells several centimeters long at a temperature of 177 °C and showed that the plane of polarization can rotate through 180 °C in a magnetic field of several kilogauss. In this case, no FR signal takes place in the geometry of crossed polarizers. However, the cell length in

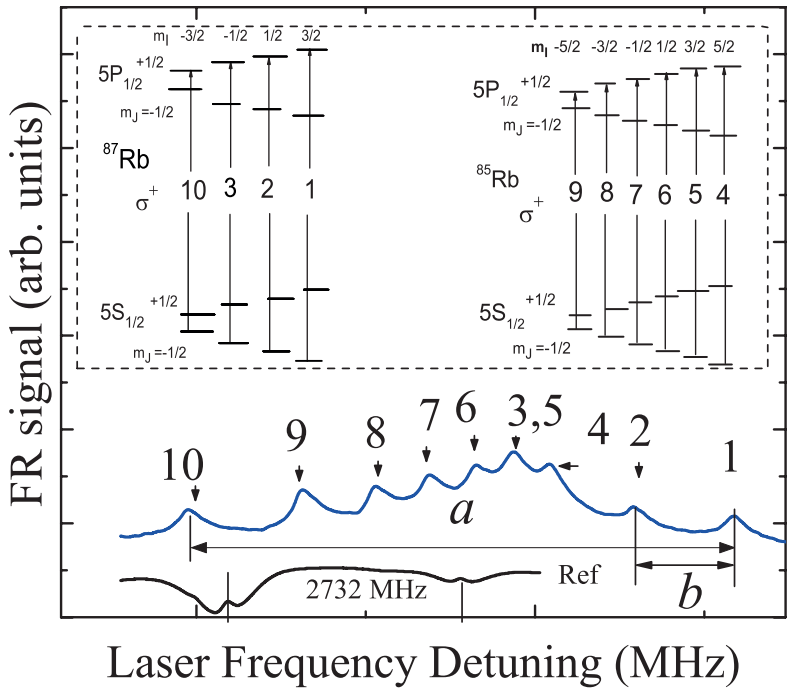

Figure 3.20: Faraday rotation spectrum of the ^{85}Rb D_1 line at $B = 2300$ G (high-frequency wing) for $L = 70$ nm, and a nano-cell reservoir temperature of 140 °C. The lower REF curve is an SA-based frequency reference, transitions ^{85}Rb, 2 -3' and ^{87}Rb, 1-2'. The insets show the diagram of ^{85}Rb and ^{87}Rb D_1 line transitions.

the case of a NC is smaller by almost six orders of magnitude; therefore, the angles of rotation are significantly lower.

3.7 Summary

In this chapter, we have presented the experimental and theoretical studies of FR effect using Cs or Rb vapor contained in a NC of half-wavelength thickness in the case of strong magnetic fields. We have seen that despite a small angle of rotation, Faraday rotation spectra exhibit resonances narrower than that for transmission. We have shown that FR spectra are very sensible to the thickness of the cell, particularly the collapse and revival of the CDN effect has been observed. A theoretical model describing FR in a NC has been developed, which describes relatively well the frequency position of atomic transitions of the recorded spectra. Note that, the difficulty of expressing the refractive index of the thin vapor layer in the NC is the reason

of discrepancies between the experimental and the theoretical results.

By recording the D lines of Cs or Rb vapor confined in a nano-cell of thickness $L \approx \lambda/2$, we have shown that the Faraday rotation in strong longitudinal magnetic fields is a convenient tool to study alkali atomic transitions in magnetic fields. Particularly, in the range 0.1 to 6 kG, the atomic transitions of Cs are split into a large number of components, and we have shown that the recorded FR signals are frequency-resolved due to sub-Doppler linewidth allowing one to investigate the behavior of individual atomic transitions.

The study of the van der Waals interaction has been experimentally performed with the help of FR process using a NC of thicknesses $L < 100$ nm and we have noticed that to study the vdW effect with the use of the FR method is more convenient than the use of other techniques, such as selective reflection or absorption. When decreasing the thickness L from 100 nm to 40 nm, we have detected the red shift of the FR signal frequency, which increases from 10 MHz to 250 MHz, meanwhile the increase of broadening of low-frequency wing takes place. Next, we have measured the vdW interaction coefficient C_3 for D lines of Rb atom. We have also demonstrated that the FR signal is very convenient to study the influence of the vdW interaction for Rb atom D_2 line $F_g = 2 \rightarrow F_e = 1, 2, 3$ transitions, for which the frequency intervals between the hyperfine structures of the upper levels are maximal.

At last, we have experimentally demonstrated that the FR effect at $L = 70$ nm can be used for measuring both homogeneous and inhomogeneous magnetic fields.

Chapter 4

New trend in high resolution atomic spectroscopy: Modified Faraday rotation method and second derivative of absorption spectra from nano-cells

Contents

In this chapter, we describe a method which is a modification of the Faraday rotation (MFR) method based on using a nano-cell. The essence of the modified FR method is the following: the output Glan polarizer is placed on a mechanical holder, which enables its smooth rotation around the axis in both clockwise and counterclockwise directions. The rotation angle relative to the crossed position is equal to 0.1 rad (note that in the case of a usual Faraday rotation method the second polarizer is crossed with the first one). In this case, the dispersion spectrum, that is, the MFR spectrum is registered at the analyzer output. The MFR method makes possible forming atomic transitions that are characterized by a spectral width a factor of 1.5 - 2 smaller than those obtained by a common method of Faraday rotation in nano-cells. It is demonstrated that using the method of MFR to study the atomic transitions of the D_2 line of the Cs atom enables a spectral separation and successful analysis of the behavior of individual atomic transitions in a wide range of magnetic fields up to 7000 G. The method of MFR works particularly well in the case of a nano-cell filled with vapors of potassium atoms, because transitions of K atoms are split into several atomic transitions characterized by a small frequency separation of $\sim$ 100 MHz in magnetic field, while Doppler broadening of atomic lines reaches $\sim$900 MHz.

4.1 Modified Faraday rotation method for studying rubidium, cesium and potassium atomic lines in magnetic fields

The experimental setup for registration of the spectrum of the modification of Faraday rotation (MFR) signal using the NC *(2)* filled with either Rb or K is illustrated in Fig. 4.1. Tunable external-cavity diode lasers (ECDL) with linewidth <1 MHz and wavelength λ = 780 nm and 767 nm are used for resonant excitation of atomic vapor on D_2 lines of Rb and K, respectively. Strong magnetic fields were obtained by using a strong permanent magnet (PM) made of a neodymium-iron-boron alloy and calibrated by means of a Teslameter HT201 magnetometer.

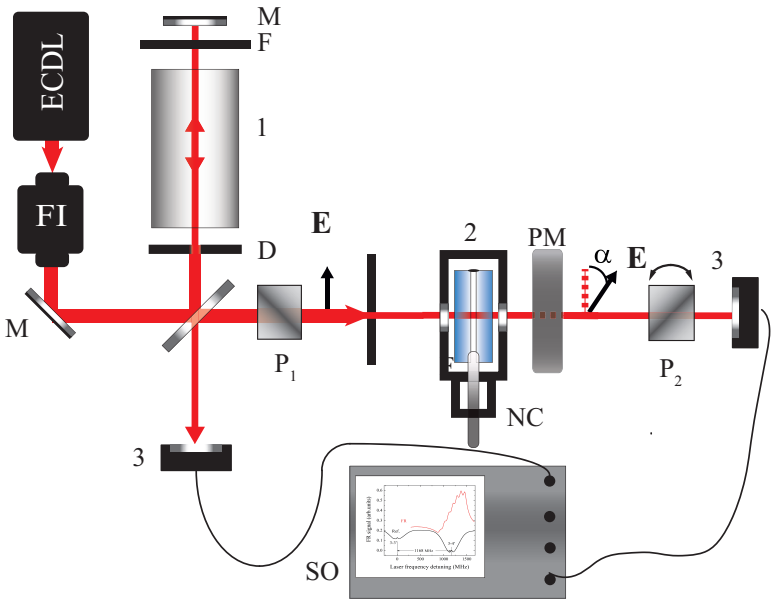

Figure 4.1: Sketch of the experimental setup. The branch 1 is to form the Reference – unit to produce the reference spectrum. The laser radiation produced by ECDL; FI – optical insulator; P_1, P_2 – Glan-Taylor polarizers; F – filter; 2 – NC filled with Cs and placed inside the oven; PM – permanent strong ring magnet; 3 – photodetectors, α–rotation angle of the polarization plane.

The magnet was placed near the output window of the NC. To create a frequency reference (Ref), a part of the laser radiation was directed into a centimeter length auxiliary cellin which saturated absorption spectrum was obtained [51]. To form a linearly polarized radiation, we used a Glan-Taylor polarizer P_1, while MFR spectra were obtained at the output of the second (output) crossed polarizer P_2 (analyzer). The output polariser P_2 is placed in a mechanical holder, which enables its smooth rotation around the axis, both clockwise and counter-clockwise. The radiations are detected by FD-24K photodiodes 3. The signals from the photodiodes were amplified by an operational amplifier and were fed into a Tektronix TDS2014B or to a Siglent SDS1202x digital oscilloscope. The MFR signal was selected by an interference filter IF with a transmission bandwidth of 10 nm at half-maximum. A diaphragm (not shown) was used to generate a beam with a diameter of 1 mm equal to the size of the region of vapors with a thickness of $L = \lambda/2$ (Fig. 4.1).

4.1.1 Vapors of Rb atoms

The atomic energy level diagrams of ^{87}Rb and ^{85}Rb in magnetic fields are presented in Fig. 4.2. The dipole allowed transitions between the lower and the upper levels of hyperfine structure F in a zero magnetic field must obey the selection rules for the full momentum of an atom of the form $F_e - F_g = \Delta F = 0, \pm 1$ and $m_{F_e} - m_{F_g} = \pm 1$, for $\sigma^{\pm}$ polarizations, respectively. It is well known that in the case of absence of magnetic field, the transitions $F_e - F_g = \pm 2$ are initially forbidden. However the applied magnetic field induces strong probability increase of these transitions. Nevertheless for some values of magnetic fields the probabilities of such transitions (forbidden in the absence of magnetic field) can exceed probabilities of allowed atomic transitions. Thus, we refer these transitions as "magneto-induced (MI) transitions [93, 94]. Magneto-induced transitions of ^{87}Rb are marked with rectangles in Fig. 4.2a while the MI transitions of ^{85}Rb are marked by circles in Fig. 4.2b. Note, that both σ^+ and σ^- radiations take part in MFR signal. The atomic transitions for σ^+ polarizations are shown with solid line while the atomic transitions for σ^- polarizations are shown by dotted lines. Figure 4.3 shows

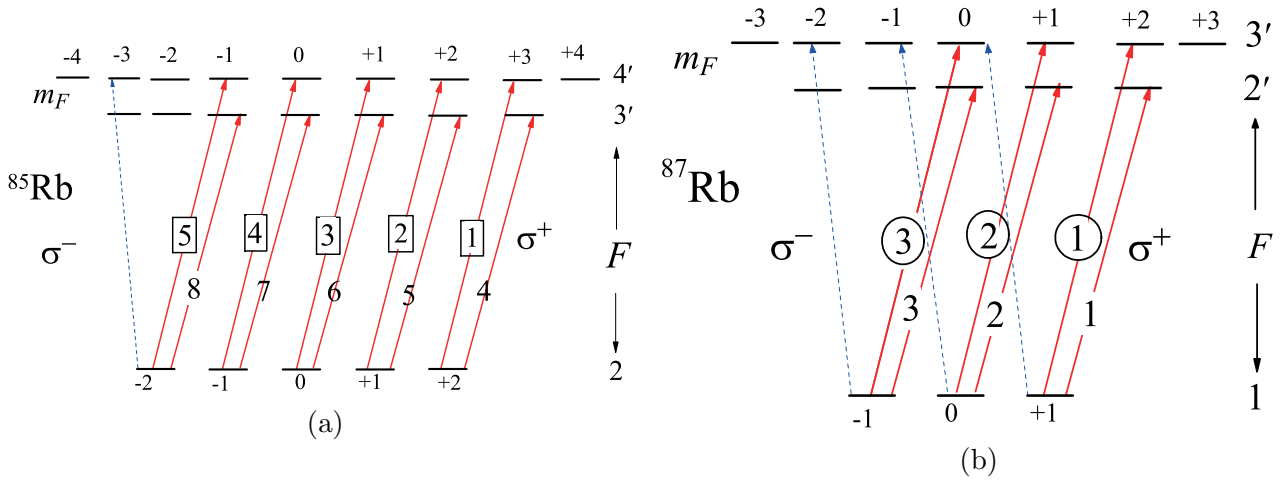

Figure 4.2: The atomic energy level diagrams of the Rb D_2 line (a) ^{87}Rb $F_g = 1 \to F_e = 2, 3$ and (b) ^{85}Rb $F_g = 2 \to F_e = 3, 4$ atomic transitions in the case of circularly σ^+ and σ^- polarized radiations. The selection rules are: $F_e - F_g = \Delta F = 0, \pm 1$, $m_{Fe} - m_{Fg} = \Delta m_F = \pm 1$ (for σ^+ and σ^- radiations, respectively). Transition in circles and rectangles are forbidden at $B = 0$ field but their probabilities experience a giant rise in magnetic field; transitions from circular polarization σ^- are shown by a dotted line.

the FR spectrum from a NC (containing Rb vapors with a thickness of $L = \lambda/2 = 390$ nm) exposed to longitudinal magnetic field $B = 600$ G. When the analyzer is rotated from the crossed position by 0.1 rad a dispersion spectrum depicted in the figure by curve MFR was obtained at the output of the analyzer. The Siglent SDS1202x oscilloscope allows real-time differentiation of

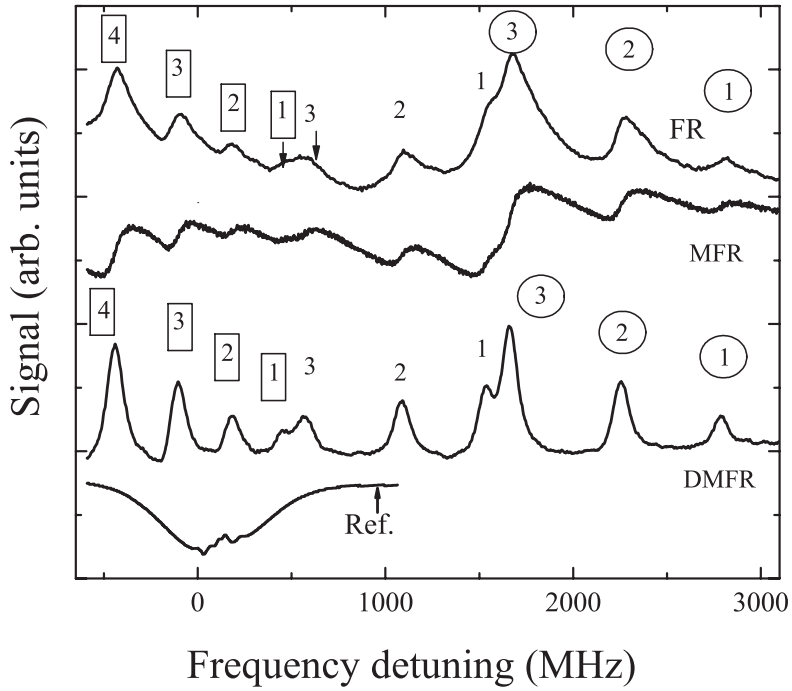

Figure 4.3: Comparison of FR, MFR and DMFR spectra from a Rb contained NC with $L = \lambda/2 = 390$ at $B = 600$G. FR - the Faraday rotation signal, MFR - Modified Faraday rotation signal and the DMFR - derivative of the MFR curve. Transitions ① - ③ and 1 - 4 in rectangles are the MI transitions of ^{87}Rb and ^{85}Rb, respectively. The lower curve is the reference spectrum recorded at $B = 0$.

the MFR curve. The result is presented by the derivative of the MFR (DMFR) curve. Magneto-induced transitions ① - ③ arise from ^{87}Rb atomic transitions $F_g = 1 \rightarrow F_e = 3$, while MI transitions 1 - 4 in rectangles are from ^{87}Rb, $F_g = 2 \rightarrow F_e = 4$ transition. It can be seen from comparison of the MFR and DMFR curves that the formed atomic lines have a spectral width a factor of 1.5 - 2 smaller in the case of the DMFR. This allows avoiding the overlap of spectra of atomic lines, which is important for correct identification of their frequency and amplitude. For example, transitions ① and ③, along with transition 1 in a rectangle and transition 3, are strongly overlapped in the FR spectrum, while in the DMFR spectrum they are well resolved.

The lower curve represents a frequency reference at $B = 0$.

Next, we will compare the experimental absorption (Abs.) spectrum with the MFR and DMFR spectra as well as with the theoretically calculated absorption (Abs. theor) spectra in the case of thickness $L = \lambda/2 = 390$ nm at magnetic field $B = 750$ G that are presented in Fig. 4.4. The theoretical spectrum shows the exact frequency position of the atomic lines and

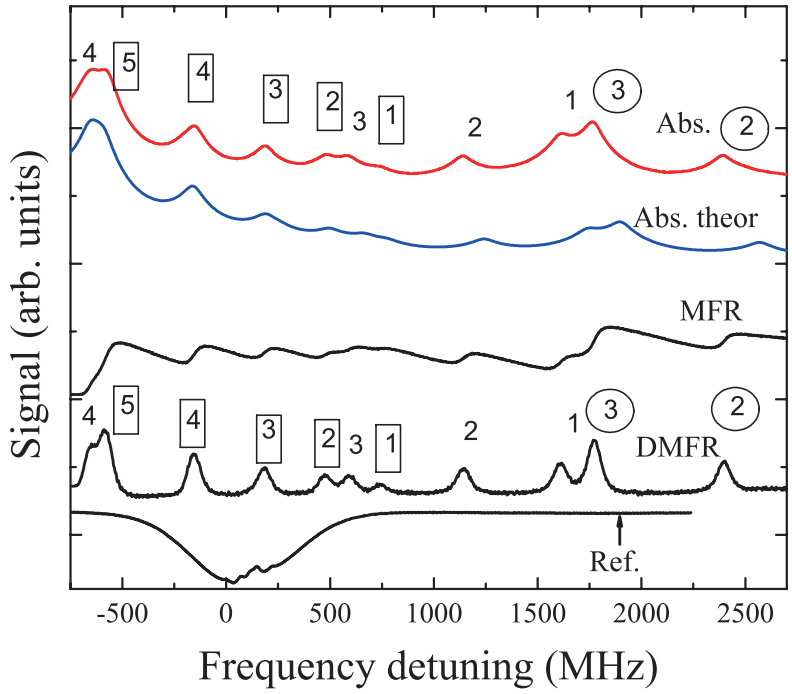

Figure 4.4: Comparison of Absorption, MFR and DMFR spectra from a Rb contained NC with $L = \lambda/2 = 390$ nm at $B = 750$ G. Abs. - the absorption spectrum, MFR - Modified Faraday rotation signal and the DMFR - derivative of the MFR , Abs. theor - calculated absorption spectrum. Transitions ② - ③ and 1 - 5 in rectangles are the MI transitions of ^{87}Rb and ^{85}Rb, respectively. The lower curve is the reference spectrum recorded at $B = 0$.

their amplitudes. Comparison of the Abs. and DMFR curves reveals that the formed atomic lines in the DMFR case (FWHM $\approx$ 70 MHz) have 2 - 2.5 smaller FWHM. For this reason, all 11 atomic lines are well resolved, whereas a number of atomic lines strongly overlap in the absorption spectrum. It can be seen from Fig. 4.4 that the theoretical curve describes position of atomic lines on the frequency scale and their amplitudes obtained by the DMFR method quite well. The lower curve is the SA based reference spectrum recorded at $B = 0$.

Note that, in Figs. 4.3, 4.4 we present the high-frequency wing of the spectrum excited

by σ^+ polarized radiation. A similar spectrum forms also in the low-frequency wing when using a σ^- polarized radiation. It can be seen from both figures that MI transition ③ has the highest amplitude among all the transitions of ^{87}Rb that originate from the lower level $F_g = 1$ (see diagram in Fig. 4.2b) at any magnitude of the applied magnetic field. This statement is confirmed both experimentally and theoretically. Since the MI transitions have zero probability at zero magnetic field, they probabilities in the presence of magnetic field experience a giant increase. A similar conclusion can also be drawn regarding MI transitions 1 - 5 in rectangles in ^{85}Rb: since these transitions have zero probability, their probabilities in the presence of magnetic field experience a giant growth. It is important to note that the probabilities of the MI transitions tend to zero at $B \gg B_0$ (for atoms of ^{85}Rb $B_0 = 0.7$ kG and for ^{87}Rb, $B_0 = 2.4$ kG). Hence, the MI transitions tend to zero at $B > 2$ kG, and at $B > 5$ kG magnetic fields for ^{85}Rb and ^{87}Rb, respectively [82].

4.1.2 Vapors of K atoms

For an atom of ^{39}K, magnetic fields can be considered as being strong starting from $B_0 = 165$ G, which is much smaller than the corresponding values for ^{85}Rb and ^{87}Rb atoms. Therefore, for atoms of ^{39}K the decoupling of **J** and **I** takes place in much weaker fields (10 - 15 times smaller), which leads in substantial change in probabilities of atomic transitions and considerable decrease in the number of transitions upon increase of the magnetic field . The realization of HPB regime, is thus realized at magnetic fields $B > 165$ G.

Figure 4.5 shows the diagram of ^{39}K atom D_2 line atomic transitions for σ^+ circularly polarized radiation in the hyperfine Paschen-Back regime in the m_J and m_I basis. The transitions obey the selection rules $\Delta m_J = +1$ and $\Delta m_I = 0$. In the case of σ^- circularly polarized radiation, the selection rules take the form $\Delta m_J = -1$ and $\Delta m_I = 0$. These transitions are not shown in order not to clutter up the diagram, since we record only the high-frequency part of the spectrum which corresponds to the case of σ^+ circularly polarized radiation.

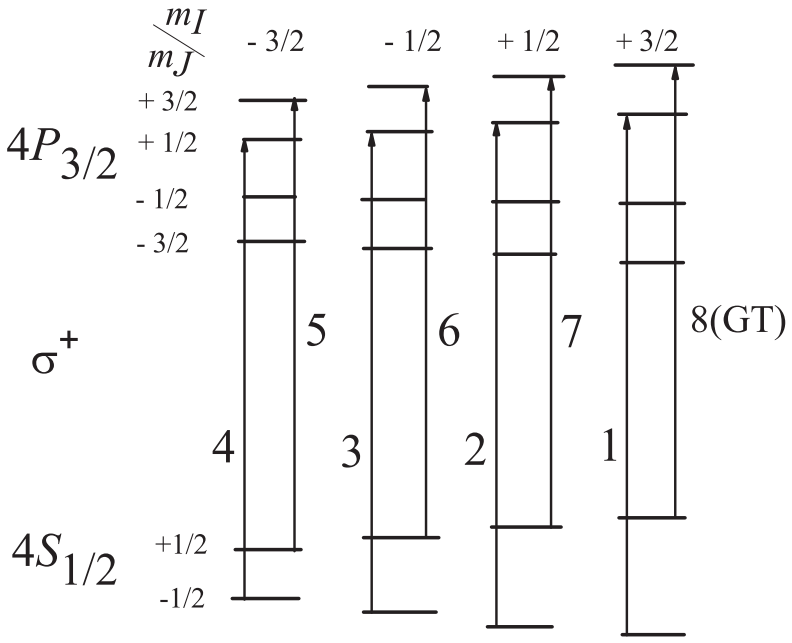

Figure 4.5: Diagram of ^{39}K atomic transition in the HBP regime in the basis m_I and m_J. The transition 8 is a "guiding" transition.

The evolution of ^{39}K, D_2 line DMFR spectra versus a magnetic field is presented in Fig. 4.6. Magnetic field induction B increases upward and amounts to B = 290 G, 360 G, 440 G, and 590 G. The FWHM of the atomic transition is approximately 60 MHz, meanwhile the Doppler width is about 900 MHz (at the temperature of $\sim$ 160 °C). It can be seen from Fig. 4.6 that two groups of lines each containing four atomic lines are detected. In so doing, in HPB regime the probabilities of transitions within each group should be equal, and frequency intervals of the transitions should be nearly the same [95]. Transition 8 deserves special attention, since it is the so-called "guiding" transition (one GT exists also in the case of σ^- circularly polarized radiation) [95]. Guiding transitions are characterized by the highest probability in their group. The probabilities of all the other transitions in the same group tend to this value in strong magnetic fields. The frequency slope of the GT (frequency shift versus B) is $s = +1.4$MHz/G. In strong magnetic fields, frequency slopes of all atomic transitions in the same group tend to this value [95, 96]. From Fig. 4.6 it is visible that the beginning of the HPB regime can be considered already at magnetic fields $B > 400$G. Note that frequency interval of atomic lines is

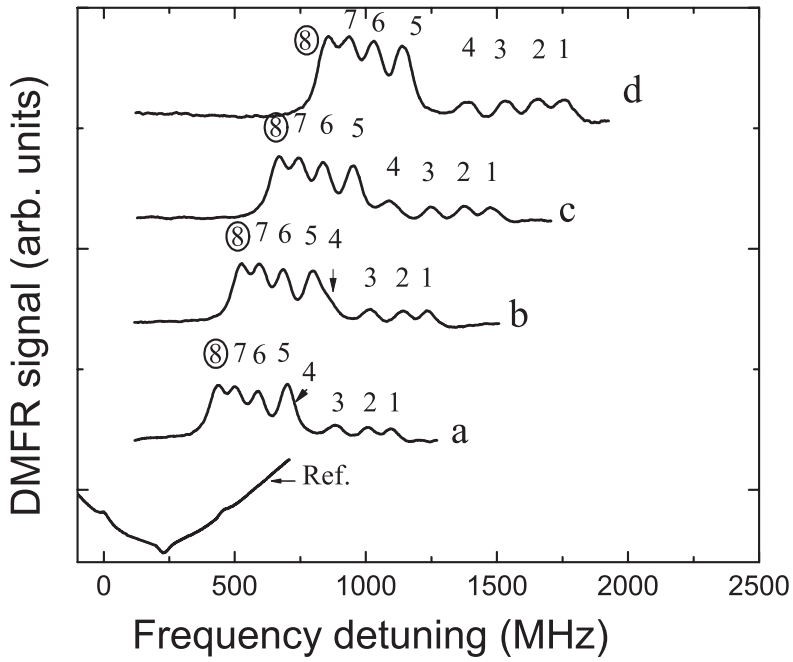

Figure 4.6: DMFR spectra of ^{39}K, D_2 in magnetic fields $B = 290$ G (a), 360 G (b), 440 G (c), 590 G (d). The lower curve is the frequency reference.

≈ 100 MHz, while the Doppler width of atomic transitions is about 900 MHz (at the temperature of ~ 160 °C). The latter speaks about the efficiency of using the DMFR method for the D_2 line of ^{39}K atoms.

Figure 4.7 shows the DMFR spectra obtained by the rotation of the analyzer clockwise (+ 0.1 rad) or counter-clockwise (- 0.1 rad). It can be seen that frequency intervals, along with the relative amplitudes within the same group, remain unchanged. The lower curve is the frequency reference at zero magnetic field.

It is important to note that, until recently, it was assumed that the best spectral resolution of atomic lines can be obtained by using selective reflection (SR) from a nano-cell of thickness $L \approx \lambda/2$, which allows spectral separation of a large number of atomic transitions formed in strong magnetic fields [97]. That is why, it is reasonable to compare the DMFR method with the method of DSR (the derivative of SR) from a nano-cell [97]. The experimental absorption, DSR and DMFR spectra of a nano-cell with a thickness of $L \approx \lambda/2$ are presented in Fig. 4.8. It can be seen that both the DMFR and the DSR spectra provide substantially higher spectral resolution

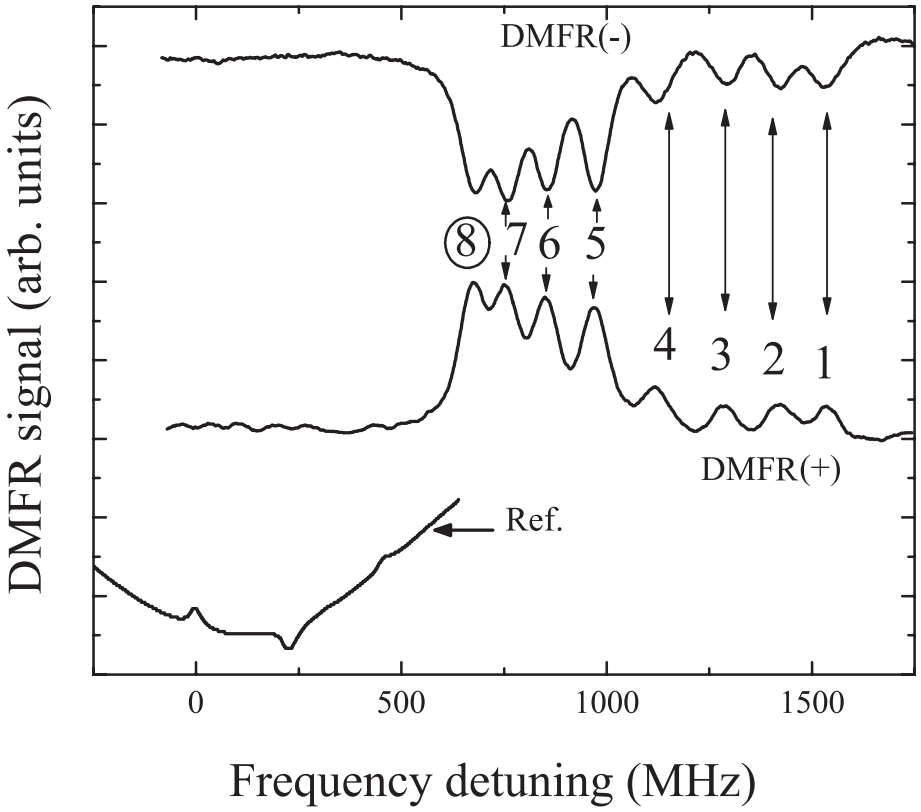

Figure 4.7: (+) and (-) derivatives of MFR spectra of ^{39}K, D_2 line, obtained upon clockwise rotation of the analyzer by + 0.1 rad and counterclockwise by -0.1 rad, respectively, at $B = 500$ G. Curve Ref serves as frequency reference.

than for the absorption spectrum of the NC. With approximately equal spectral resolution of the DMFR and DSR methods, the former has the advantage of a spectrum being formed on a nearly constant background, which is convenient when the spectral envelope has to be decomposed into individual components. Another advantage of the DMFR method is the fact that it measures the spectrum of radiation transmitted by the cell, whereas the signal reflected from a nano-cell is recorded in the DSR method. In particular, when using a permanent magnet with a small aperture for laser radiation, such a small aperture is acceptable for the DMFR method, while creating technical difficulties for implementation of the SR process.

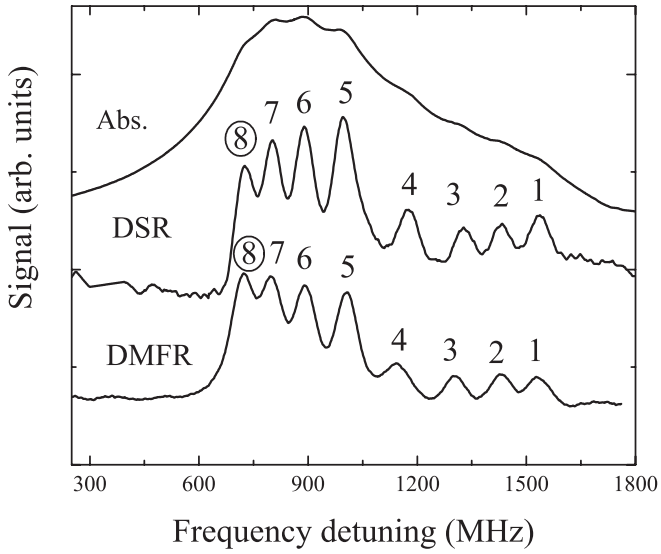

Figure 4.8: Comparison of the absorption, the derivative of selective reflection and the derivative of MFR signals at $L \sim \lambda/2$, $B = 500$ G. The curve DMFR and the curve SR have nearly the same spectral resolution, the spectrum of the DMFR forms on a constant background, which is convenient for technical applications.

4.1.3 Vapors of Cs atoms

The experimental setup for registration of the MFR signal using the NC filled with Cs slightly differs from the one presented in the section 3.4. Here the radiation of a continuous narrow-band diode laser with the wavelength $\lambda = 852$ nm (Cs D_2 line) has been used. The main requirement for the laser is the linearity of frequency scanning in a wide range of ~ 50 GHz; at the same time, the spectral linewidth of the laser was relatively large ~ 20 MHz, however, this does not affect the accuracy of determining the frequency positions of atomic transitions in magnetic fields. When using the laser with the linewidth of $\Delta\nu_L$ $\sim$1 MHz, the region of linearity of frequency scanning scales down greatly, which is unacceptable. Strong magnetic fields were obtained by using a strong permanent magnet made of a neodymium-iron-boron alloy and calibrated by the Teslameter HT201 magnetometer.

The NC containing Cs metal was placed between these magnets. To increase the magnetic field, the permanent magnets were mounted on a Π-shaped metal magnetic core with the cross section of 40×50 mm^2, which also has small holes for the passage of laser radiation. To be able to vary

the magnitude of the magnetic field, a coil was put on a metallic magnetic core on which the direct current was applied. Depending on the direction of the current in the coil, the magnetic field applied to the NC either was increased or decreased. The magnetic field created by the coil was approximately equal to 250 G at a current of 1 A (the current varied in the range of 0 –4 A). To form the frequency reference, the part of the laser radiation was directed to an additional centimeter length cell with alkali metal to form the transmission spectrum. The other details of experimental realization does not differ from the one presented in section 3.4.

Figure 4.9 shows the diagram of atomic transitions of Cs D_2 line in the basis F and m_F at magnetic fields $B \geq B_0$, when the linearly polarized laser radiation is applied. According to the selection rules for allowed (in the dipole approximation) transitions between the ground and upper levels of the hyperfine structure for the full momentum of the atom F in the zero magnetic field, the selection rules $F_e - F_g = \Delta F = 0; 1$ should be met, and for magnetic sublevels $\Delta m_F = 1$ and $\Delta m_F = +1$ for σ^- and σ^+ polarized radiations, respectively. It is well known that in strong magnetic fields there can be a gigantic increase of atomic transition probabilities (intensities) with the selection rules $F_e - F_g = 2$ [65,93,94,98,99]. As we discussed earlier, the probabilities of these transitions (which are forbidden at $B = 0$) can exceed the probabilities of allowed atomic transitions for some values of the magnetic field. Therefore, we called them magnetically induced (MI) transitions [93,94]. In the diagram presented in Fig. 4.9b, the magneto-induced transitions for Cs atoms for a σ^- radiation are indicated by rectangles while the MI transitions for σ^+ are taken into circles. Note that both radiations with circular polarizations σ^+ and σ^- are involved in the FR process. However, in order not to complicate the diagrams, the atomic transitions are shown separately for polarizations σ^+ and σ^-.

Figure 4.10a shows the frequency positions of atomic transitions in the case of σ^+ polarization. Only those transitions, whose probabilities remain large enough for strong magnetic fields $B > B_0$ are depicted. It is seen from Fig. 4.10a that the atomic transitions form three groups: 1) a group of seven MI transitions ① - ⑦ located on the high-frequency wing of the spectrum; 2) a group of eight transitions 1 - 8 (shown in the diagram of Fig. 4.9); 3) a group of eight transitions

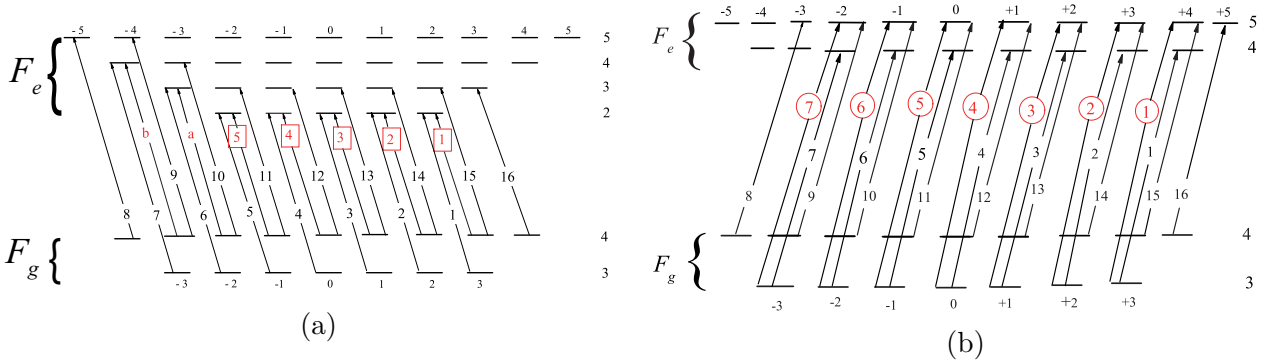

Figure 4.9: The diagram of transitions of Cs D_2 line in the basis F and m_F. Only are shown transitions that have high probabilities at magnetic fields $B \geq B_0$, (a) radiation polarization σ^-, transitions 1 - 5 in rectangles these are the MI transitions; (b) radiation polarization σ^+, transitions 1 - 7 in circles are the MI transitions. Note that to avoid confusion, transition labeling in the text is accompanied with the corresponding polarization.

labeled 9 -16. With the increase of the magnetic field, the frequency distance between these groups increases. The probabilities of these atomic transitions are represented in Fig. 4.10b. As follows from Fig. 4.10b, the probabilities of seven MI transitions ① - ⑦, have the highest probability at the magnetic fields ∼1000 G, however, at the fields > 7000 G, these probabilities tend to zero. Thus, only two groups remain the group of eight transitions 1 - 8 and the group of eight transitions 9 - 16. An explanation of such a behavior is given below. We especially note the transition number 16. This is the so-called "guiding" atomic transition for Cs D_2 line, when using radiation with the circular polarization σ^+. As can be seen from numerical simulations presented in Fig. 4.10b, the probability of the GT transition is constant, and does not depend on the value of B. The magnitude of the frequency slope of the GT transition is equal to $s = 1.4$ MHz/G and does not depend on B. In his group, the frequency slopes of all atomic transitions in strong magnetic fields tend to this value [96].

Figure 4.11a shows the frequency positions and transition intensities in the case of σ^- polarization. Similar to the Fig. 4.10, it is seen from Fig. 4.11a, that the atomic levels form three groups: 1) a group located on the low-frequency wing of the spectrum, consisting of five MI transitions 1 - 5 in the rectangles and the allowed transitions labeled as a and b; 2) a group of eight transitions 9 - 16; 3) a group of eight transitions 1 - 8. With an increase of the magnetic

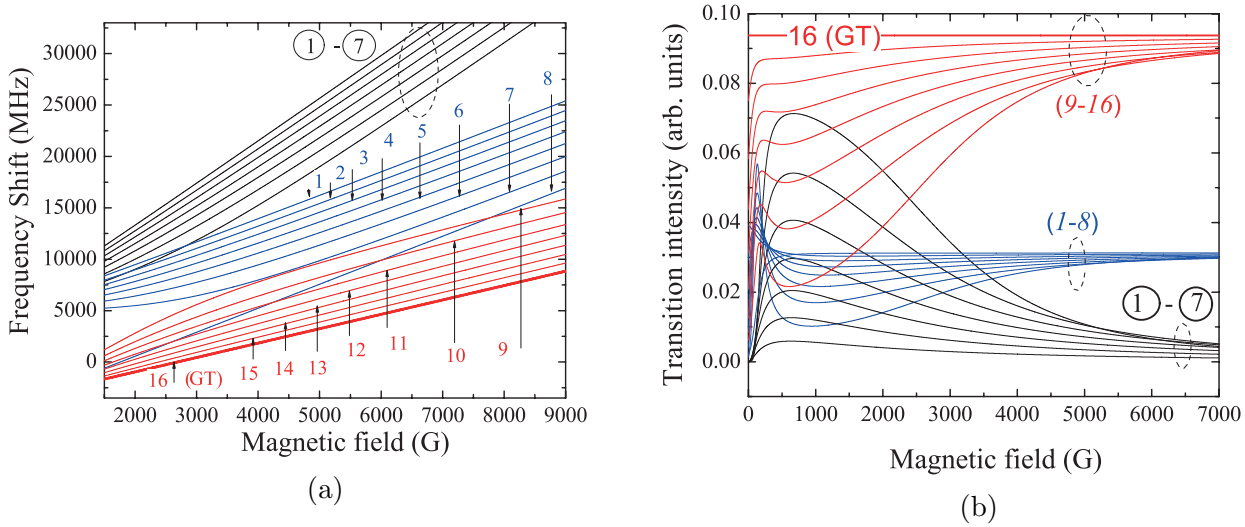

Figure 4.10: The transitions frequency shift and probability of Cs, D_2 line when a σ^+ radiation is applied versus magnetic field. The numerical simulation have performed according to the theoretical model presented in [65].

field, the frequency distances between the groups increase and they are completely separated at $B > 8000$ G. The probabilities of these atomic transitions are shown in Fig. 4.11b. As it can be seen from Fig. 4.11b, the probabilities of five MI transitions 1 - 5 in the rectangles and transitions labeled with a and b, in the magnetic fields about 1000 G have the greatest probability, however, at fields > 7000 G, their probabilities tend to zero. Thus, at $B \gg B_0$ there are only two groups left: a group of eight transitions 1 - 8 and a group of eight transitions 9 -16. The explanation is given below. We especially note the transition number 8 for σ^- polarization which is the GT atomic transition of the group.

Left hand circularly polarized laser field

The derivative of the MFR curve from a nano-cell of length $L = \lambda/2$, when the magnetic field value is $B = 6200$ G, the laser power is 0.1 mW and the temperature is 115 °C, is shown in Fig. 4.12. Figure 4.12 shows the best spectral resolution since the atomic transitions 7 and 9 are fully spectrally resolved in the case of the DMFR curve. In addition, the narrower is the width of atomic transitions in the case of the DMFR curve, the more correct information on

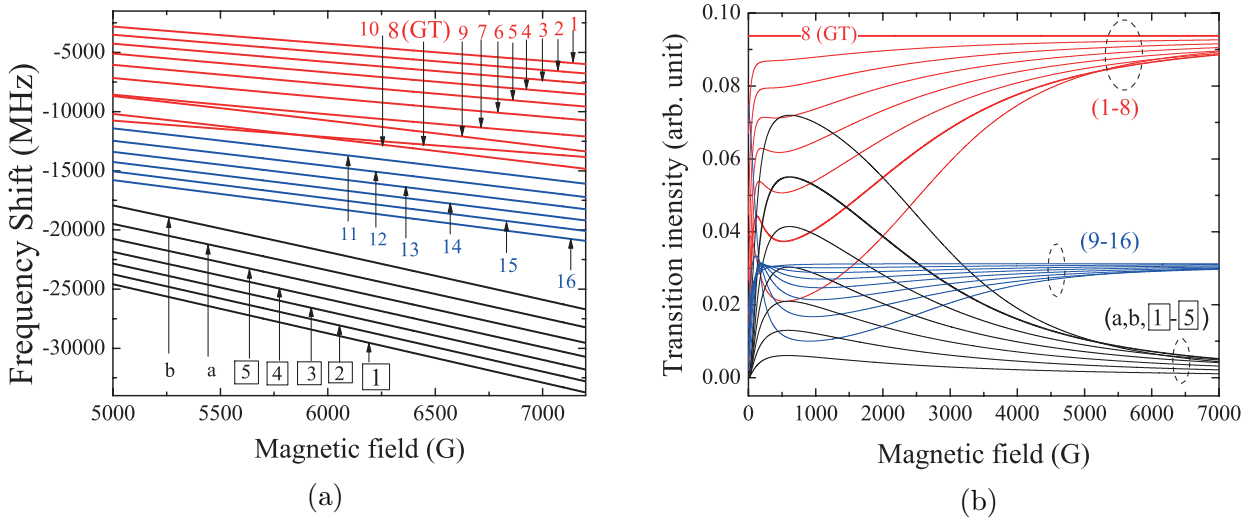

Figure 4.11: The frequency positions of atomic transitions having the highest probabilities at magnetic fields $B > B_0$ with σ^- radiation polarization, (b) the dependences of probabilities of atomic transitions on the magnetic field (σ^- polarization).

the transition amplitudes (probabilities) we obtain. Thus, the transition amplitude of the GT number 16 should be the largest in the spectrum, which corresponds to the largest amplitude on the DMFR curve, while the transition amplitude number 16 in the FR spectrum is smaller than that of the transition amplitude 15, which provides the real amplitude ratio incorrectly. Comparison of the DMFR and theoretical absorption spectra for σ^+ polarization at $B = 6600$ G are presented in Fig. 4.13. Note that all sixteen atomic transitions (transitions 1 - 8 and 9 -16) are spectrally resolved. The blue curve Abs. theor shows the calculated (theoretical) absorption spectrum in the nano-cell with the thickness $L = \lambda/2 = 426$ nm, which contains an important information about the frequency positions of atomic transitions and their amplitudes [59]. Figure 4.13 shows that the DMFR method also gives the correct positions of all atomic transitions and the values of their amplitudes.

The DMFR curves (a, b, c, d, e) in Fig. 4.14 show the derivative of the MFR spectrum at the output of the analyzer (rotated by 0.1 rad) for different values of the magnetic field B and for σ^+ polarization: for curves a, b, c, d, e, these values are equal to 5000, 5300, 6200, 6600 and 6900 G, respectively. From Fig. 4.14 it is clear that at the values of fields 6600 and 6900 G, all

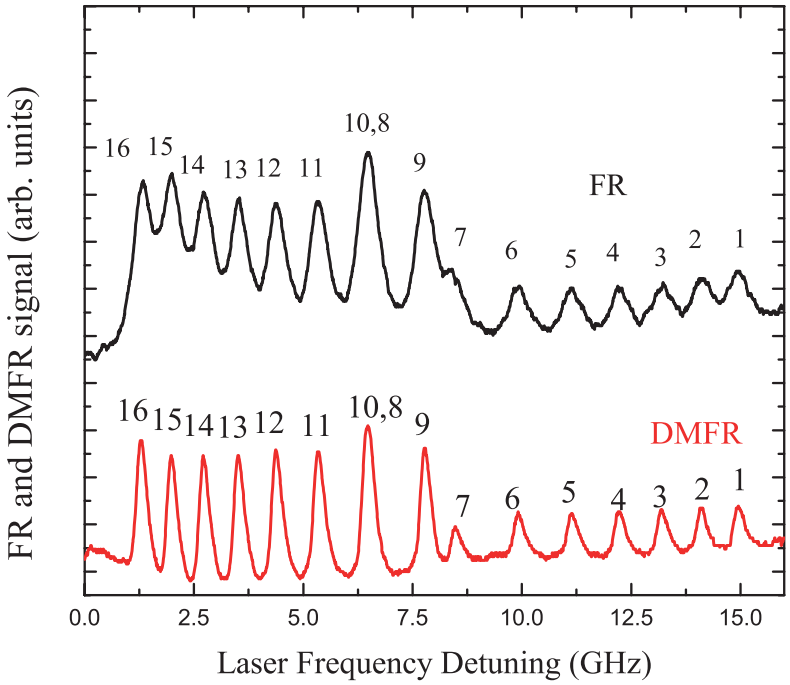

Figure 4.12: The FR spectrum in the case when the analyzer is crossed with the first polarizer when σ^+ polarized laser radiation is applied at $L = \lambda/2 = 426$ nm, $B = 6200$ G power 0.1 mW, the temperature of the nano-cell reservoir 115 °C. The lower curve is the DMFR spectrum. It can be seen that the spectral resolution is better in the case of the DMFR curve (see peaks 7 and 9 for instance).

sixteen atomic transitions are spectrally separated.

Right hand circularly polarized laser field

The middle curve in Fig. 4.15 shows the experimental spectrum obtained by the DMFR method. Note that all sixteen atomic transitions (1 - 8 and 9 -16) are spectrally resolved in this case.

In Fig. 4.16 the DMFR curves (a', b', c', d', e') show the derivative of the MFR signal at the output of the analyzer for different magnetic field values B for σ^- polarization: for curves a', b', c', d', e', these values are equal to 5230, 5340, 6170, 6700 and 6900 G, respectively. It is seen from Fig. 4.16, that all sixteen atomic transitions are spectrally separated at the fields 6700 and 6900 G.

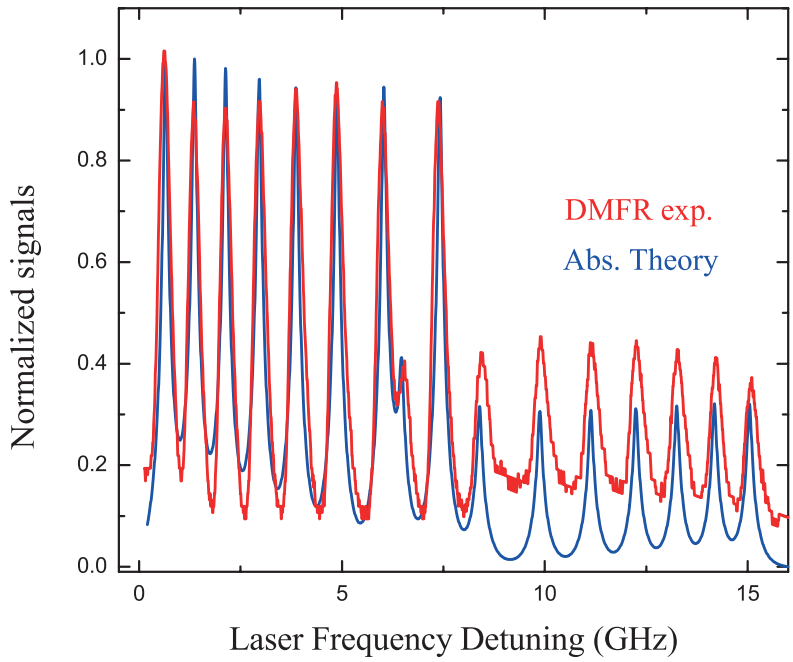

Figure 4.13: The DMFR and Absorption curves for σ^+ polarization at $B = 6600$ G. All the sixteen transitions are spectrally separated.

4.2 Resolution-enhanced quantitative spectroscopy of atomic vapor in optical nano-cells based on second-derivative processing of spectra

We propose a simple data processing technique, which allows retrieval of homogeneous lineshape of individual optical transitions in absorption spectra, which are initially masked by overlapped inhomogeneous spectral profile. The technique is efficient for the spectra of a NC with a vapor column thickness equal to half of the wavelength of the resonant laser radiation [17,34,47]. The following procedure is employed. After recording the absorption spectrum with scanning the laser radiation frequency across the resonant region, the second order derivative $A''(\omega)$ is determined from the raw absorption spectrum $A(\omega)$. As a result, the transition linewidth in the second derivative spectrum reduces down to $\sim$ 15 MHz ($\sim$ 50-fold narrower as compared with the Doppler broadening). This allows to separate and study individual atomic transitions.

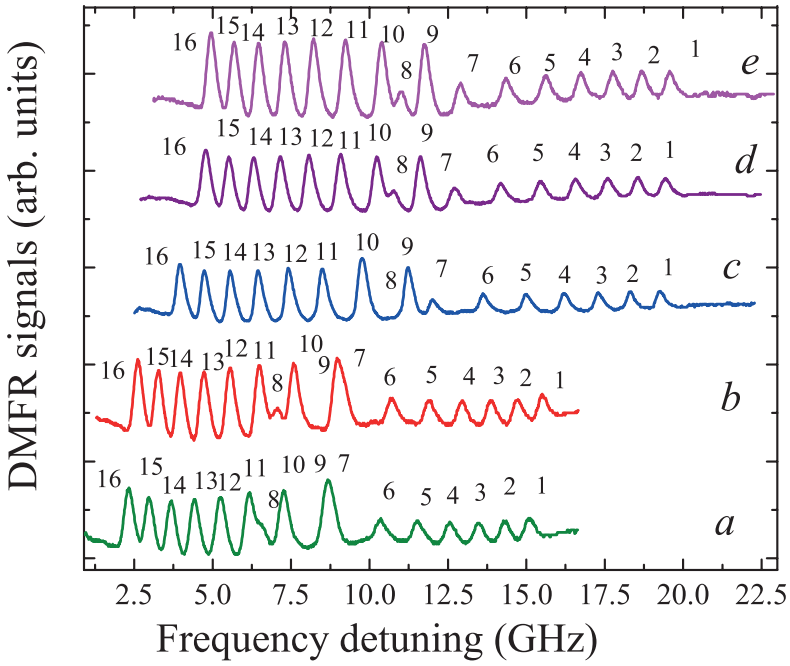

Figure 4.14: The DMFR curves (a', b', c', d, e') at various values of field B for polarization: for curves a', b',c', d', e', these values are equal to 5230, 5340, 6170, 6700 and 6900 G, respectively. It can be seen that all sixteen transitions are spectrally separated at fields 6700 and 6900 G. The numbering of atomic lines is shown in Fig. 4.9a for σ^- polarization. The lower curve is the reference.

Here we demonstrate that the SD treatment of the recorded signal preserves not only frequency positions of spectral features but, importantly, also their amplitude values linked, in linear interaction regime, with transition probabilities. We present below some particular realizations of resonant optical processes where the SD technique is employed, and prove its capability for quantitative measurements.

The experimental setup is schematically sketched in Fig. 4.17. Tunable external-cavity diode lasers (ECDL) with spectral linewidth < 1 MHz and wavelength $\lambda = 780$, 852, 767, and 770 nm were used for resonant excitation of atomic vapor on D_2 lines of Rb, Cs, K and D_1 line of K, respectively. The laser beam was directed normally to the windows of NC containing atomic vapor with a thickness of atomic vapor column $L \sim \lambda/2$. The absorption spectra are recorded with the help of photo-diodes, and a four-channel digital storage oscilloscope Tektronix TDS2014B. Thanks to the use of NC, a uniform magnetic field variable in the range of $B = 10 - 10000$ G can

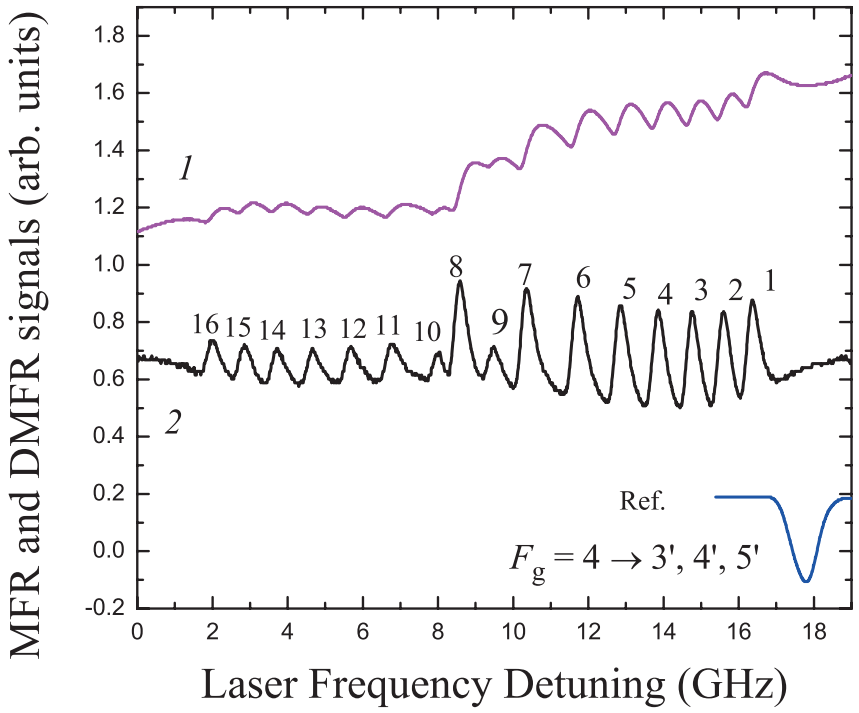

Figure 4.15: MFR and DMFR experimental spectra at $B = 6600$ G, when $L = \lambda/2 = 426$ nm. The curve *1* is the MFR, the curve *2* is the DMFR spectrum The lower curve Ref. is the frequency reference.

be applied to the vapor by strong permanent magnets mounted on the translation stages [27]. The first verification of the proposed technique was done for the NC absorption spectra on Rb D_2 line, for hyperfine transitions $F_g = 3 \rightarrow F_e = 2, 3, 4$ (hereafter use the simplified notation $3 \rightarrow 2'$, $3'$, $4'$, see the right panel in Fig. 4.18). These transitions are poorly resolved even in the NC absorption spectra, as is seen from Fig. 4.18a, meanwhile they are completely resolved in the SD spectrum (Fig. 4.18b) due to the small ($\sim$ 15 MHz FWHM) linewidth. Here and below, the modeling of experimental spectra was done using the previously developed theoretical model [17, 34, 47] with the following key assumptions: the vapor density N is low enough, so that the effect of interatomic collisions can be is ignored, and only atom-surface collisions are considered; the atoms experience inelastic collisions with the NC walls. The effect of reflection of the laser radiation from both highly-parallel windows of the NC, as well as Doppler-broadening effect are taken into account. In the experiment, the temperature of the NC reservoir was kept at 110 °C corresponding to vapor density $N_{Rb} \approx 1.1{\times}10^{13}$ cm^{-3}, the laser radiation power was P_L

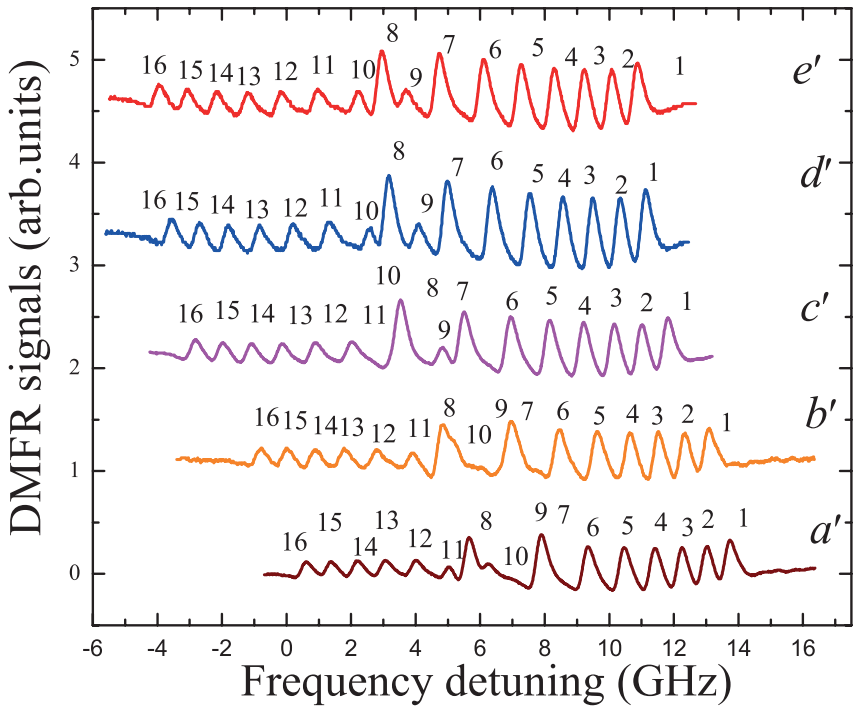

Figure 4.16: The DMFR curves (a', b', c', d', e') at various values of field B for σ^- polarization: for curves a', b', c', d, e, these values are equal to 5000, 5300, 6200, 6600 and 6900 G, respectively. It can be seen that all sixteen transitions are spectrally separated at fields 6600 and 6900 G.

$= 10$ μW, sufficiently low to avoid saturation and optical pumping effects. The extra broadening over the natural linewidth $\gamma_N/2\pi = 6$ MHz is caused by the atom-surface collisions.

As one can see from Fig. 4.18b, the SD method allows retrieving the homogeneous absorption spectra from inhomogeneously (*e.g.* Doppler) broadened one, with the use of a single low-power laser beam. Moreover, the SD method correctly displays both the frequency positions of individual transitions and their relative probabilities (the inaccuracy is 3-5%). It is also important to note that precise value $L = \lambda/2$ for the NC thickness is not crucial: narrow spectra are observed with $\Delta L = \pm$ 50 nm tolerance, which makes utilization of the proposed technique experimentally feasible.

Relatively narrow unshifted resonances obtained with SD method allow implementation of the SD spectra for frequency reference applications. A frequency reference technique mostly used in atomic physics experiments is based on saturated absorption spectroscopy [51]. In this technique, the laser beam is split into a weak probe field and a strong pump field, which are sent to

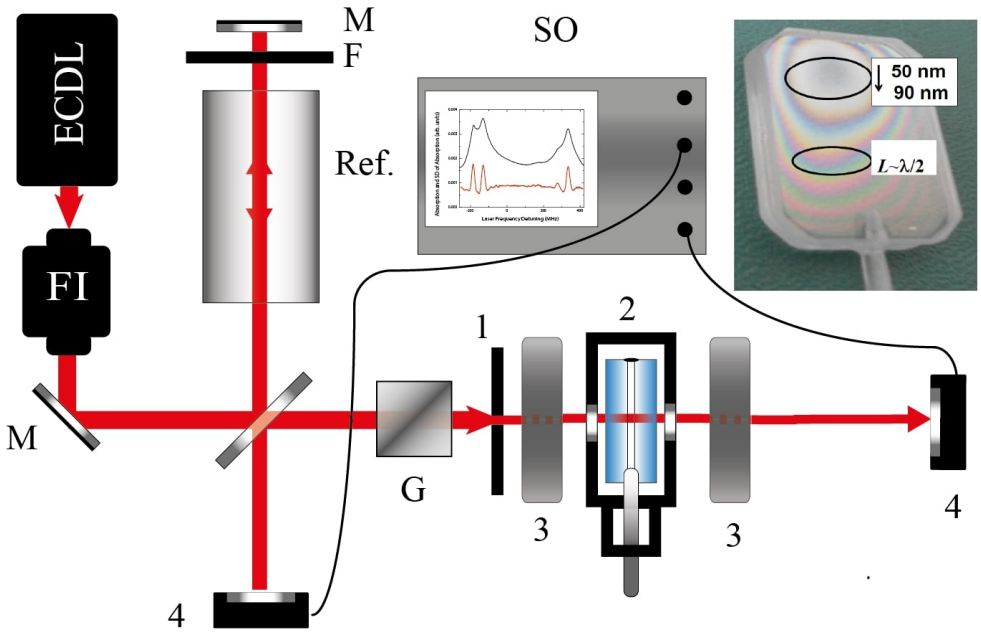

Figure 4.17: Sketch of the experimental setup. ECDL-diode laser; FI- Faraday isolator; 1 - $\lambda/4$ plate; 2 - NC filled with the Rb or Cs or K, in the oven; 3 - permanent magnets; 4 - photodetectors; M - mirror; F - filter; SO - digital storage oscilloscope, G - Glan polarizer, Ref.- frequency reference unit. The inset shows the photograph of the NC filled with Cs, where interference fringes formed at the reflection of light by the inner surfaces of the windows are seen; the upper and lower ovals mark the thickness regions 50 - 90 nm and $\sim$ 426 nm in the case of Cs ($L \approx \lambda/2$), respectively.

the interaction cell as overlapping counter-propagating beams. This allows to form Doppler-free velocity-selective optical pumping resonances located at the line center. When multiple hyperfine transitions are Doppler-overlapped, additional crossover resonances appear in the spectrum, with the amplitudes, which can exceed the VSOP amplitudes because of strongly nonlinear interaction regime. This may cause distortions affecting "real" atomic resonances. Comparison of SD and SA spectra recorded for $2 \rightarrow 2',3',4'$ transitions of ^{85}Rb D_2 line is presented in Fig. 4.19. Only three resolved atomic resonances are observed in the SD spectrum (Fig. 4.19a), while for the FR formed using SA technique (Fig. 4.19b) there are three VSOP and three CO resonances. The following advantages of the SD method as a FR tool can be mentioned: i) simplicity of the realization geometry (single-beam transmission as opposed to counter-propagating beams

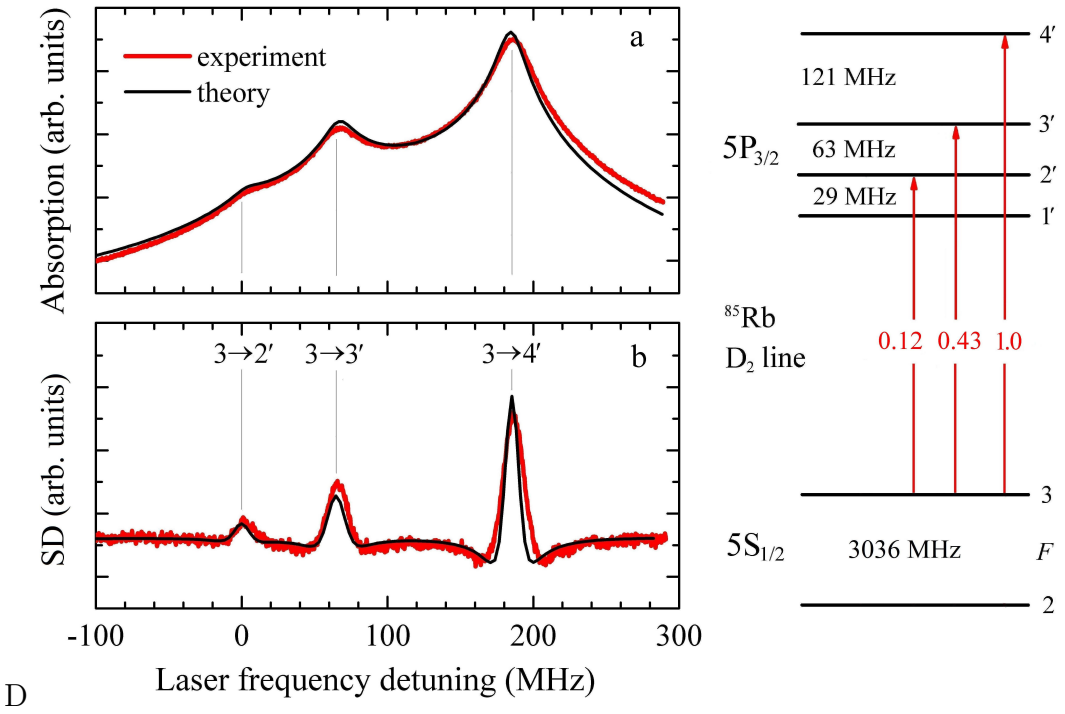

Figure 4.18: a) Absorption spectrum of a rubidium NC with $L \sim 390$ nm for $3 \rightarrow 2'$, $3'$, $4'$ hyperfine transitions of ^{85}Rb D_2 line. b) Second derivative of the absorption spectrum. Red lines: experiment; black lines: theory. Gray vertical lines indicate frequency positions of the transitions. Right panel: energy levels diagram, showing the transitions, their frequency separations and relative probabilities. Here and bellow the probabilities are normalized to the probability of the strongest transition in the group.

requirement for SA geometry); ii) low value of the required laser power (3 orders less than for the SA method); iii) absence of crossover resonances; iv) correspondence of the amplitudes of atomic resonances to their transition probabilities: in particular, the measured ratio of $2 \rightarrow 2'$ and $2 \rightarrow 1'$ SD amplitudes is 1.05, close to the ratio of their probabilities (1.053), while this ratio for the SA method is around 5. Another application where SD method can be employed is the study atom–surface van der Waals (vdW) interaction, which can be revealed from atomic spectra for $L < 100$ nm [85,91], where the use of nano-cells is advantageous. Absorption spectra for $4 \rightarrow 3'$,$4'$,$5'$ transitions of ^{133}Cs D_2 line, recorded for two values of the NC thickness, $L \approx \lambda/2 \approx 426$ nm and $L = 75$ nm, are presented in Fig. 4.20, together with the corresponding SD spectra. For $L = 426$ nm, due to the relatively large cell thickness (i.e. large mean distance of atoms from the sapphire windows of NC), the atomic transitions do not undergo frequency shift, thus serving as

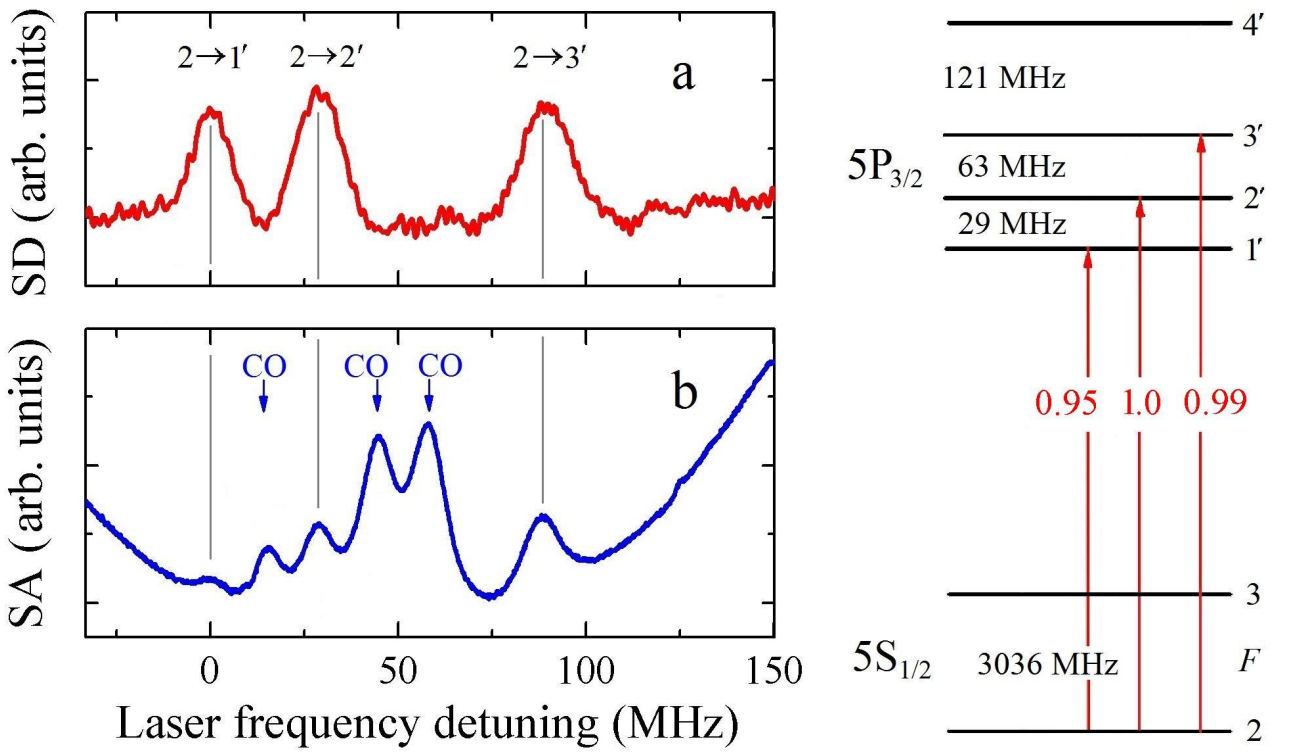

Figure 4.19: Experimentally recorded frequency reference spectra formed for $2 \rightarrow 2',3',4'$ transitions of ^{85}Rb D_2 line using absorption SD spectrum in a NC (a) and SA in an ordinary cell (b). Frequency positions of hyperfine transitions are marked with vertical gray lines; CO labels indicate positions of crossover resonances in SA spectrum. Right panel: energy levels diagram, showing the transitions, their frequency separations and relative probabilities.

frequency reference markers [85]. The red shift of frequency is observable for $L = 75$ nm, but the strong broadening and overlapping of individual lines in the absorption spectrum (Fig. 4.20a) make quantitative measurements of the frequency shift impossible. Application of SD processing results in complete frequency resolution of hyperfine transitions, revealing ≈ 70 MHz vdW red shift for all the three hyperfine transition components due to the interaction. The latter allows to estimate the value of C_3 vdW interaction coefficient using expression $\Delta\nu_{vdW} = -16C^3/L^3$ presented in Ref. [85], which yields $C_3 = 1.8\pm0.3$ kHz$\times$ μm^3, which is in a good agreement with the value reported in Ref. [91]. The inaccuracy arises from the inaccuracy in determining the NC thickness ($\pm$ 5 nm). We should note that similar measurements can be done for other transitions of Cs, and equally for other alkali metals. Furthermore, the SD method can be used

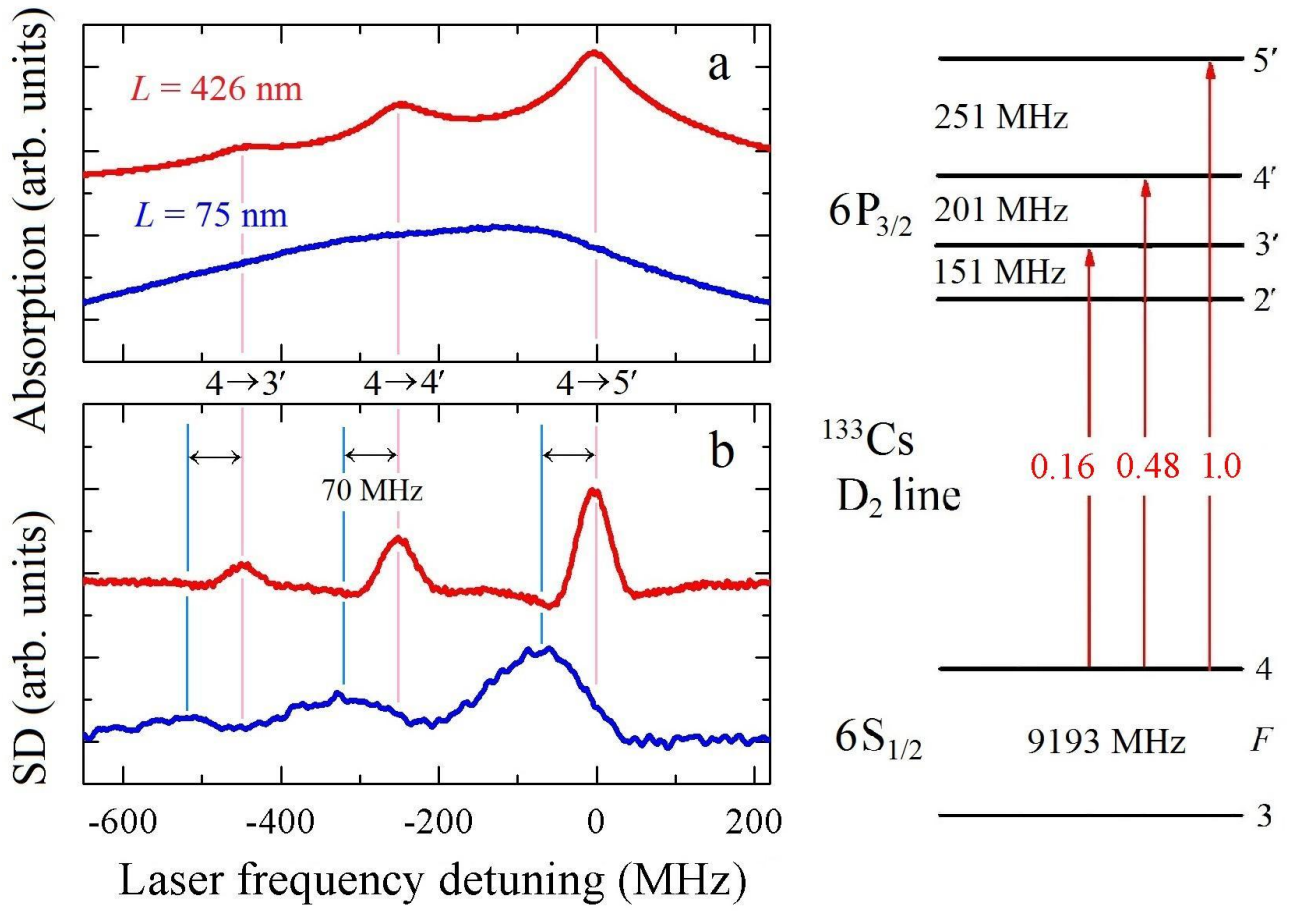

Figure 4.20: Experimental absorption (a) and SD (b) spectra for $4 \rightarrow 3',4',5'$ transitions of ^{133}Cs D_2 line, recorded for two values of the NC thickness marked by ovals on the Cs photograph in Fig. 4.17: $L = 426$ nm (red lines) and $L = 75$ nm (blue lines). $P_L = 10$ μW. A red shift of ≈ 70 MHz caused by the vdW interaction is seen for all the frequency-resolved transition components in SD spectra (see text). Right panel: energy levels diagram, showing the transitions, their frequency separations and relative probabilities.

for determination of isotopic abundance. To verify this possibility experimentally, we have chosen a NC filled with potassium as an alkali metal with strongly different percentages in natural isotopic mixture, with predominant abundance of ^{39}K (93.25 %), and minor abundance of ^{41}K (6.7%). Experiment was done for D_1 line of K, using a NC with $L \approx \lambda/2 \approx 385$ nm and reservoir temperature 150 °C corresponding to $N_K \approx 1.3\times10^{13}$ cm^{-3}. The measured absorption and processed SD spectra are shown in Fig. 4.21. Thanks to the small linewidth obtained in SD spectrum ($\approx$ 15 MHz, 60 times narrower than the Doppler width), all the hyperfine transitions

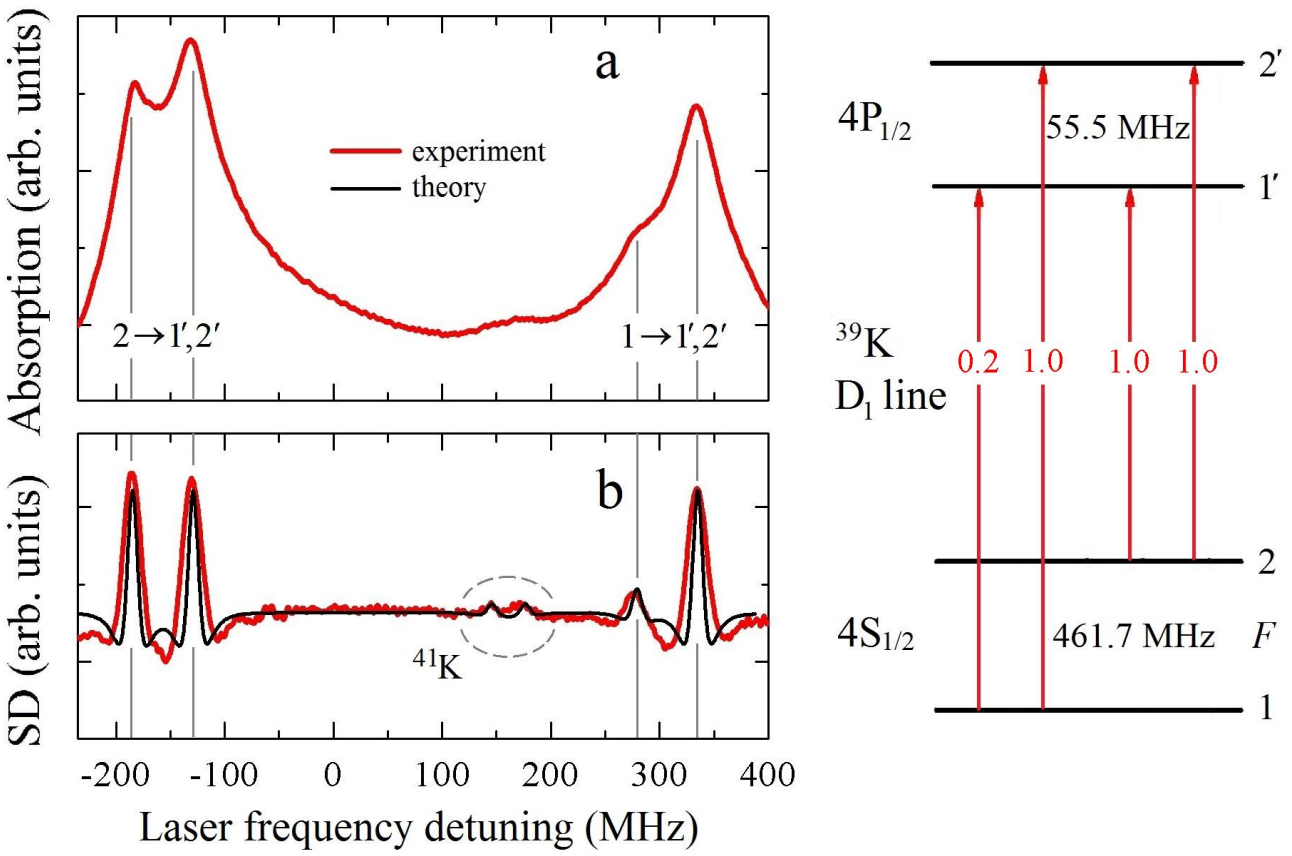

Figure 4.21: Absorption (a) and SD (b) spectra for D_1 line of K, recorded in a NC with $L \approx \lambda/2 \approx 385$ nm, and $P_L = 10$ μW. Red lines: experiment; black line: theory. SD peaks corresponding to $2 \rightarrow 1',2'$ transitions of ^{41}K separated by 31 MHz are clearly seen (marked by a dotted oval). Right panel: energy levels diagram of ^{39}K, showing the transitions, their frequency separations and relative probabilities.

of ^{39}K are completely resolved. Besides, the SD spectrum reveals also the hyperfine transitions $2 \rightarrow 1',2'$ of ^{41}K D_1 line with the frequency separation of 31 MHz (dash-circled in Fig. 4.21b). In the weak and linear absorption limit, the amplitude of absorption peak A is proportional to the absorption cross-section σ, the atomic vapor density N, and the atomic vapor thickness L: $A \sim \sigma N L$, see Ref. [51]. Therefore, the ratio of the amplitudes $A_{^{39}K}/A_{^{41}K} \approx 14$ for the corresponding hyperfine transitions of ^{39}K and ^{41}K isotopes measured from Fig. 4.21b must be proportional to the ratio of their partial densities $N_{^{39}K}/N_{^{41}K} \approx 13.9$ expected from the isotopic abundance. A good agreement between the amplitude values obtained for experimental and modelled spectra (see Fig. 4.21b) confirms the validity of the above suppositions concerning the

employed absorption regime.

We should mention that the absorption SD technique can be extended for determination of

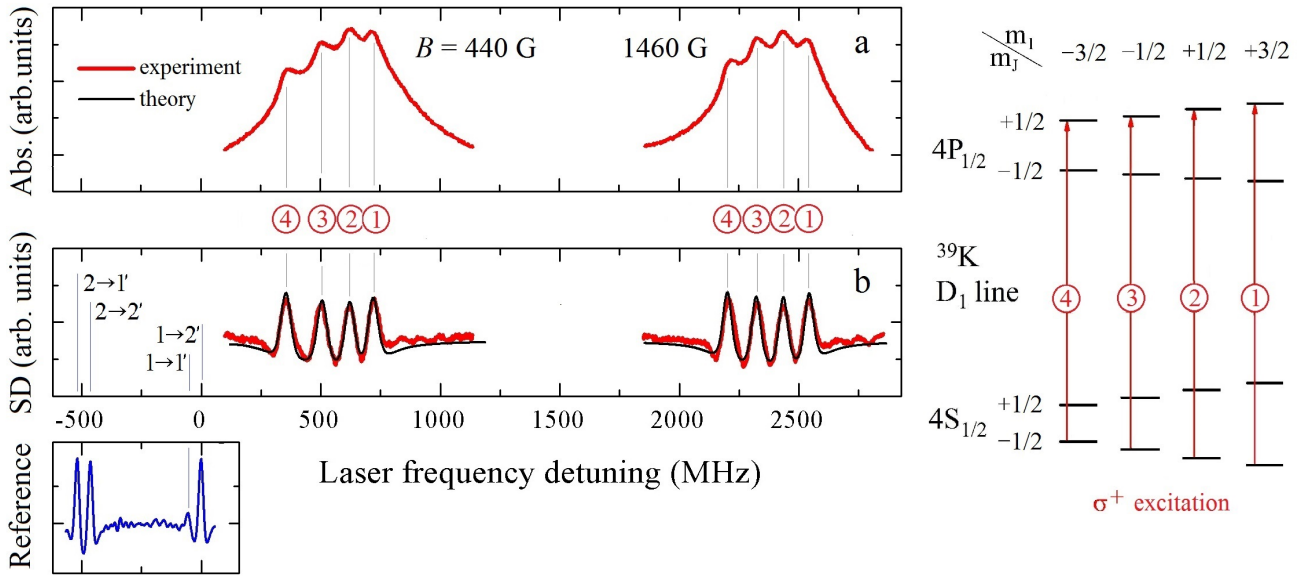

Figure 4.22: Absorption (a) and SD (b) spectra for D_1 line of ^{39}K, recorded using σ^+-polarized excitation in a NC with $L \approx 385$ nm for two values of a longitudinal magnetic field: $B = 440$ and 1460 G. Red lines: experiment, black lines: theory. Right panel shows the transitions diagram; the four components remaining in the HPB regime are labeled in circles. The lower left graph (blue line) is the reference spectrum recorded at $B = 0$.

isotopic composition of other, non-alkali vapor. In Ref. [100], SA method was employed to measure the isotopic abundance of mercury (a mixture of five Hg isotopes with the minimum frequency spacing of 100 MHz) in an atomic vapor cell. Implementation of the SD method for such measurements could be more straightforward. For this purpose it is expedient to use recently developed glass nano-cells [101], which are simpler in fabrication, but, unlike sapphire NCs [35], do not safeguard immunity against highly-aggressive hot alkali vapors.

Correct mapping of resonance frequency and transition probability provided by the SD method makes it attractive when studying processes linked with splitting of atomic transitions and modification of their probabilities in an external magnetic field. The quantity $B_0 = A_{hfs}/\mu_B$ is introduced for quantitative characterization of the atom – B-field interaction [67], where A_{hfs} is the magnetic dipole constant of the atoms hyperfine structure, and μ_B is the Bohr magneton. In

strong magnetic fields ($B \gg B_0$), the total electron momentum **J** and nucleus momentum **I** become decoupled, manifesting establishment of a hyperfine Paschen-Back (HPB) regime [66, 67], where atomic system is described by momentum projections m_J and m_I.

Absorption and SD spectra exhibiting splitting of D_1 line atomic transitions of ^{39}K in the magnetic field are presented in Fig. 4.22. The spectra are recorded with circularly (σ^+) polarized laser radiation, for two values of the magnetic field, $B = 440$ and 1460 G exceeding $B_0 = 165$ G for ^{39}K atom. As is seen from the right panel of Fig. 4.22, in the HPB regime four atomic transitions remain in the spectrum of ^{39}K D_1 line [66], governed by selection rules $\Delta m_J = +1$; $\Delta m_I = 0$. As the resonance linewidth in SD spectra is about 50 MHz, twice less than the spacing between transition components, they are completely spectrally resolved. The case of $B = 440$ G corresponds to the onset of the HPB regime, and one can see that the frequency separation between the transitions labeled 3 and 4 is larger than for 1 and 2. For $B = 1460$ G, the HPB regime is fully established, and all the components spacing becomes equidistant [66]. We should note that the transition labeled 4 is a guiding transition, which is characterized by the highest (and invariable) value of probability in the group, and the probabilities of other transitions tend to this value when $B \gg B_0$ [66]. In the case of σ^- excitation, also four atomic transitions are observable, located far on the low-frequency range of the spectrum (not shown).

Fig. 4.23 presents absorption and SD spectra for D_2 line of ^{39}K, recorded with σ^+- polarized radiation in the HPB regime ($B = 500$ G). As is seen from the right panel of the figure, eight transitions remain in the spectrum for this case (two transition groups, each containing four components). The probabilities of transitions within each group are equal, and frequency spacing of the lines is nearly the same, which is a manifestation of the HPB regime. Evidently, all the transitions are fully resolved in SD spectrum (Fig. 4.23b), unlike the raw absorption spectrum, where they are strongly overlapped. Transition labeled 8 is a guiding transition [95]. In the case of σ^--polarized excitation, the eight atomic transitions appear far on the low-frequency range of the spectrum (not shown).

Summarizing, we have implemented the proposed SD method for quantitative atomic spec-

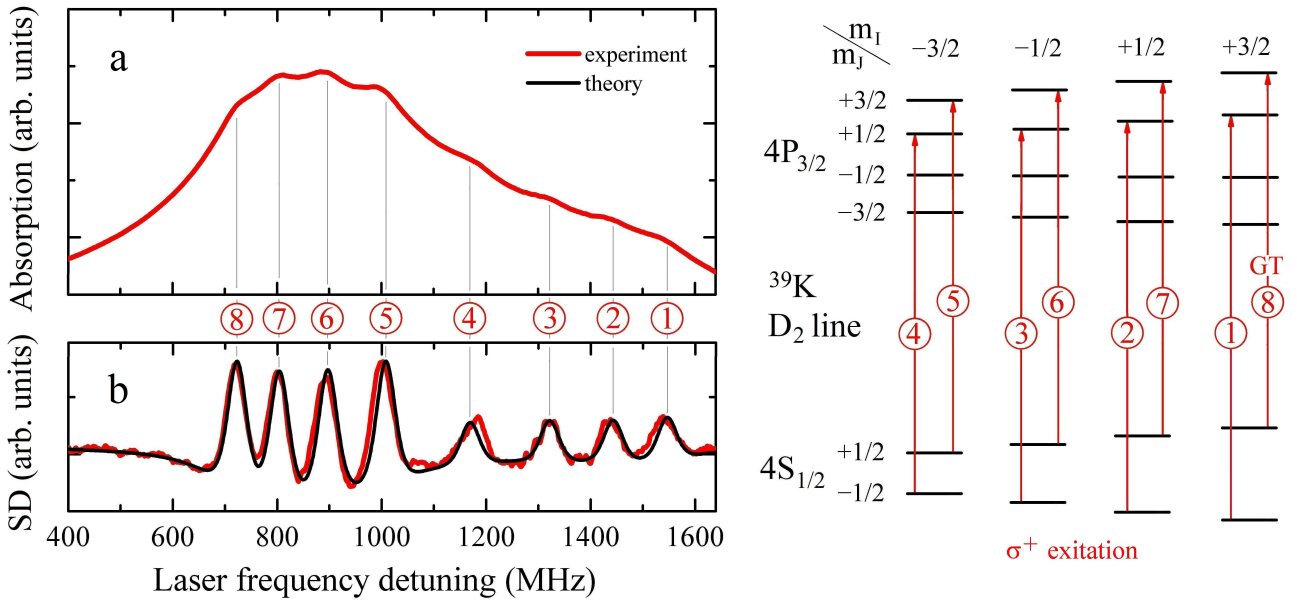

Figure 4.23: Absorption (a) and SD (b) spectra for D_2 line of ^{39}K, recorded using σ^+-polarized excitation in a NC with $L \approx 385$ nm exposed to $B = 500$ G longitudinal magnetic field. Red lines: experiment, black line: theory. Right panel shows the transitions diagram; the eight components remaining in the HPB regime are labeled in circles.

troscopy in five particular physical problems, and have shown its effectiveness. The technique is technically simpler in realization as compared with other known methods, including saturated absorption, selective reflection using a NC [85]. Moreover, the method preserves linear response of the media, it does not require high laser power, and does not generate extra resonances as for SA. We should mention that the SD technique can be especially advantageous for the spectroscopy of Na, where narrow resonances can be formed despite an extra-large Doppler broadening ($\sim$ 1.5 GHz). It can be also successfully implemented for studies of magnetically-induced atomic transitions and their applications demonstrated recently [102].

4.3 Summary

In the last chapter of this thesis, we have investigated new possibilities to form narrow optical resonances in nano-cells. We have developed a method based on the modification of Faraday rotation effect. The essence of this effect is the following: the output polarizer (analyzer) is

placed on a holder, which allows its smooth rotation around the axis in both clockwise and counterclockwise directions. When the rotation angle of the analyzer is equal to 0.1 rad, at the output of the analyzer we have recorded a dispersion spectrum of the MFR. Onward, we have performed the derivation of this signal and we have revealed atomic lines having a spectral width 1.5 to 2 times narrower than that obtained by the FR method. Using the DMFR method we have recorded the magnetically induced transitions of alkali atoms. We have compared the theoretical absorption and experimental DMFR curves and we have shown that the DMFR method is linear with respect to atomic probabilities and gives the correct positions of the atomic transitions.

At last, we have shown that second derivation processing of transmission spectra yields the strongest line narrowing among all methods studied in this thesis. We have shown that the SD method preserves the frequency positions and amplitudes of spectral transitions, thus being applicable for quantitative spectroscopy. The proposed technique has successfully applied and tested for: measurements of hyperfine splitting and atomic transition probabilities; development of an atomic frequency reference; determination of isotopic abundance; study of atom-surface interaction; and determination of magnetic field-induced modification of atomic transitions frequency and probability. We have also shown that the obtained experimental results are fully consistent with theoretical modeling.

Conclusion and outlook

We have developed a theoretical model describing the resonant interaction of the laser light with the thin alkali vapor layer in the presence of an external static magnetic field. We have shown that due to a transient regime of interaction, only slow atoms contribute to the signal and their transmission spectrum is essentially Doppler-free. The nature of the obtained spectra makes the transmission spectroscopy from a nano-cell a convenient technique to perform studies of closely-spaced atomic transitions and investigate their behavior in magnetic fields. Experimental realizations for magnetic fields up to 7000 G show an excellent agreement between theory and experiment.

We have also explored the Faraday rotation of the plane polarization of light with the propagation through the thin atomic slab. We have seen that despite a small angle of rotation, Faraday rotation spectra exhibit resonances narrower than that for transmission. We have shown that this method is a convenient tool to study D lines atomic transitions of alkali vapor confined in a nano-cell.

At last, we have investigated new possibilities to form narrow optical resonances in nano-cell. Particularly, we have implemented a method for recovery of narrow homogeneous spectral features out of broad inhomogeneous overlapped profile based on second-derivative processing of the absorption spectra of alkali metal atomic vapor nano-cells. We have shown that this method preserves the frequency positions and amplitudes of spectral transitions, thus being applicable for quantitative spectroscopy. The proposed technique was successfully applied and tested for: measurements of hyperfine splitting and atomic transition probabilities; development of an

atomic frequency reference; determination of isotopic abundance; study of atomsurface interaction; and determination of magnetic field-induced modification of atomic transitions frequency and probability.

Possible outlook of this thesis concerns the development of a proper theoretical model explaining the reason why Faraday rotation technique is not linear with respect to atomic probabilities. To do so, one will have to express the susceptibility (and refractive index) in the thin slab of atomic vapor, which is usually treatment make use of the bulk properties of a medium.

Practical applications of this work include optimization of alkali vapor Faraday filters as well as tunable atomic frequency reference and a new generation of magnetometers based on quantitative spectroscopy of alkali vapors in nano-cells with second derivative processing.

Bibliography

[1] S. Harris. *Laser without inversion: Interference of lifetime-broadened.* Phys. Today **50**(7), (1997) 36. 2

[2] D. Budker, W. Gawlik, D. Kimball, S. Rochester, V. Yashchuk, and A. Weis. *Resonant nonlinear magneto-optical effects in atoms.* Rev. Mod. Phys. **74**(4), (2002) 1153. 2, 77

[3] D. Meschede. *Optics, light and lasers: the practical approach to modern aspects of photonics and laser physics.* John Wiley & Sons (2017). 2

[4] J. Vanier. *Atomic clocks based on coherent population trapping: a review.* Appl. Phys. B **81**(4), (2005) 421. 2

[5] M. Auzinsh, D. Budker, and S. Rochester. *Optically polarized atoms: understanding light-atom interactions.* Oxford University Press (2010). 2

[6] J. B. Khurgin. *Slow light in various media: a tutorial.* Adv. Opt. Photon. **2**(3), (2010) 287. 2

[7] J. Kitching. *Chip-scale atomic devices.* Appl. Phys. Rev **5(3)**, (2018) 031302. 2

[8] S. Briaudeau, D. Bloch, and M. Ducloy. *Detection of slow atoms in laser spectroscopy of a thin vapor film.* EPL **35**(5), (1996) 337. 2

[9] B. Zambon and G. Nienhuis. *Reflection and transmission of light by thin vapor layers.* Opt. Commun. **143**(4), (1997) 308. 2, 29, 31, 42, 54, 60

[10] S. Briaudeau, D. Bloch, and M. Ducloy. *Sub-Doppler spectroscopy in a thin film of resonant vapor.* Phys. Rev. A **59**(5), (1999) 3723. 2, 4

[11] S. Briaudeau, S. Saltiel, G. Nienhuis, D. Bloch, and M. Ducloy. *Coherent Doppler narrowing in a thin vapor cell: Observation of the Dicke regime in the optical domain.* Phys. Rev. A **57**(5), (1998) R3169. 2, 4

[12] S. Briaudeau, S. Saltiel, J. Leite, M. Oria, A. Bramati, A. Weis, D. Bloch, and M. Ducloy. *Recent developments in sub-Doppler spectroscopy in a thin cell.* J Phys IV pages 8–145. 2, 4

[13] A. C. Izmailov. *On the possibility of resolving the sub-Doppler structure of spectral lines by using transit effects under optical pumping.* Laser Phys. **3**(2), (1993) 507. 2, 4

[14] T. Vartanyan and D. Lin. *Enhanced selective reflection from a thin layer of a dilute gaseous medium.* Phys. Rev. A **51**(3), (1995) 1959. 2, 4, 54

[15] D. Sarkisyan, D. Bloch, A. Papoyan, and M. Ducloy. *Sub-Doppler spectroscopy by submicron thin Cs vapour layer.* Opt. Commun. **200**(1), (2001) 201. 3, 4, 19, 20

[16] G. Dutier, A. Yarovitski, S. Saltiel, A. Papoyan, D. Sarkisyan, D. Bloch, and M. Ducloy. *Collapse and revival of a Dicke-type coherent narrowing in a sub-micron thick vapor cell transmission spectroscopy.* EPL **63**(1), (2003) 35. 3, 4, 19, 54

[17] G. Dutier, S. Saltiel, D. Bloch, and M. Ducloy. *Revisiting optical spectroscopy in a thin vapor cell: mixing of reflection and transmission as a Fabry–Perot microcavity effect.* J. Opt. Soc. Am. B **20**(5), (2003) 793. 3, 29, 30, 34, 96, 98

[18] D. Sarkisyan, T. Becker, A. Papoyan, P. Thoumany, and H. Walther. *Sub-Doppler fluorescence on the atomic D_2 line of a submicron rubidium-vapor layer.* Appl. Phys. B **76**(6), (2003) 625. 3

[19] G. V. Nikogosyan, D. G. Sarkisyan, and Y. P. Malakyan. *Absorption of resonance radiation and fluorescence of a layer of an atomic gas with thickness of the order of a wavelength.* J. Opt. Technol. **71**(9), (2004) 602. 3, 16, 19

[20] D. Sarkisyan, T. Varzhapetyan, A. Sarkisyan, Y. Malakyan, A. Papoyan, A. Lezama, D. Bloch, and M. Ducloy. *Spectroscopy in an extremely thin vapor cell: Comparing the cell-length dependence in fluorescence and in absorption techniques.* Phys. Rev. A **69**(6), (2004) 065802. 3

[21] D. Sarkisyan, A. Papoyan, T. Varzhapetyan, J. Alnis, K. Blush, and M. Auzinsh. *Sub-Doppler spectroscopy of Rb atoms in a sub-micron vapour cell in the presence of a magnetic field.* J. Opt. A: Pure Appl. Opt. **6**(3), (2004) S142. 3

[22] D. Sarkisyan, A. Papoyan, T. Varzhapetyan, K. Blush, and M. Auzinsh. *Zeeman effect on the hyperfine structure of the D_1 line of a submicron layer of ^{87}Rb vapor.* Opt. Spectrosc. **96**(3), (2004) 328. 3

[23] D. Sarkisyan, A. Papoyan, T. Varzhapetyan, K. Blushs, and M. Auzinsh. *Fluorescence of rubidium in a submicrometer vapor cell: spectral resolution of atomic transitions between Zeeman sublevels in a moderate magnetic field.* J. Opt. Soc. Am. B **22**(1), (2005) 88. 3

[24] E. Gazazyan, A. Papoyan, D. Sarkisyan, and A. Weis. *Laser frequency stabilization using selective reflection from a vapor cell with a half-wavelength thickness.* Laser Phys. Lett. **4**(11), (2007) 801. 3, 19

[25] M. Fichet, G. Dutier, A. Yarovitsky, P. Todorov, I. Hamdi, I. Maurin, S. Saltiel, D. Sarkisyan, M.-P. Gorza, D. Bloch, and M. Ducloy. *Exploring the van der Waals atom-surface attraction in the nanometric range.* EPL **77**(5), (2007) 54001. 3

[26] C. Andreeva, S. Cartaleva, L. Petrov, S. Saltiel, D. Sarkisyan, T. Varzhapetyan, D. Bloch, and M. Ducloy. *Saturation effects in the sub-Doppler spectroscopy of cesium vapor confined in an extremely thin cell.* Phys. Rev. A **76**(1), (2007) 013837. 3, 54

[27] A. Sargsyan, G. Hakhumyan, A. Papoyan, D. Sarkisyan, A. Atvars, and M. Auzinsh. *A novel approach to quantitative spectroscopy of atoms in a magnetic field and applications based on an atomic vapor cell with $L = \lambda$.* Appl. Phys. Lett. **93(2)**, (2008) 021119. 3, 98

[28] A. Papoyan and D. Sarkisyan. *Magneto-optical processes in atomic vapor cells with radiation wavelength-scale thickness.* In *15^{th} International School on Quantum Electronics: Laser Physics and Applications*, volume 7027. International Society for Optics and Photonics (2008). 3

[29] T. Varzhapetyan, A. Nersisyan, V. Babushkin, D. Sarkisyan, S. Vdović, and G. Pichler. *Study of atomic transition self-broadening and shift with the help of a nano-cell.* J. Phys. B **41**(18), (2008) 185004. 3

[30] D. Sarkisyan and A. Papoyan. *Optical processes in micro-and nanometric thin cells containing atomic vapor.* Nova Sc. Publ (2009). 3

[31] A. Sargsyan, A. Papoyan, D. Sarkisyan, and A. Weis. *Efficient technique for measuring laser frequency stability.* EPJ AP **48**(2), (2009) 1. 3

[32] S. Cartaleva, S. Saltiel, A. Sargsyan, D. Sarkisyan, D. Slavov, P. Todorov, and K. Vaseva. *Sub-Doppler spectroscopy of cesium vapor layers with nanometric and micrometric thickness.* J. Opt. Soc. Am. B **26**(11), (2009) 1999. 3

[33] G. Hakhumyan, A. Sargsyan, C. Leroy, Y. Pashayan-Leroy, A. Papoyan, and D. Sarkisyan. *Essential features of optical processes in Rb submicron thin cell filled with neon gas.* Opt. Express **18**, (2010) 14577. 3

[34] A. Sargsyan, Y. Pashayan-Leroy, C. Leroy, and D. Sarkisyan. *Collapse and revival of a Dicke-type coherent narrowing in potassium vapor confined in a nanometric thin cell.* J. Phys. B **49**(7), (2016) 075001. 4, 43, 96, 98

[35] J. Keaveney, A. Sargsyan, U. Krohn, I. G. Hughes, D. Sarkisyan, and C. S. Adams. *Cooperative Lamb Shift in an Atomic Vapor Layer of Nanometer Thickness.* Phys. Rev. Lett. **108**, (2012) 173601. 4, 20, 73, 74, 105

[36] J. Keaveney, I. G. Hughes, A. Sargsyan, D. Sarkisyan, and C. S. Adams. *Maximal Refraction and Superluminal Propagation in a Gaseous Nanolayer.* Phys. Rev. Lett. **109**, (2012) 233001. 4, 20

[37] K. Whittaker, J. Keaveney, I. Hughes, A. Sargsyan, D. Sarkisyan, and C. Adams. *Optical response of gas-phase atoms at less than $\lambda/80$ from a dielectric surface.* Phys. Rev. Lett. **112**(25), (2014) 253201. 4, 71, 75

[38] D. Sarkisyan, T. Varzhapetyan, and A. Sarkisyan. *Yu. Malakyan, A. Papoyan, A. Lezama, D. Bloch, and M. Ducloy.* Phys. Rev. A **69**, (2004) 065802. 4, 19, 43

[39] A. Sargsyan, R. Mirzoyan, A. Sarkisyan, A. Amiryan, and D. Sarkisyan. *Splitting of N-type optical resonance formed in Λ-system of ^{85}Rb atoms in a strong transverse magnetic field.* J. Contemp. Phys. (Armenian Ac. Sci.) **49**(1), (2014) 20. 7, 13

[40] A. D. Sargsyan, G. T. Hakhumyan, A. H. Amiryan, C. Leroy, H. S. Sarkisyan, and D. H. Sarkisyan. *Atomic transitions of Cs D_2 line in strong transverse magnetic fields.* J. Contemp. Phys. (Armenian Ac. Sci.) **50**(4), (2015) 317. 7

[41] A. D. Sargsyan, G. T. Hakhumyan, A. S. Sarkisyan, A. O. Amiryan, and D. Sarkisyan. *Frequency reference for atomic transitions of Rb D_2-line based on the effect of selective reflection.* J. Contemp. Phys. (Armenian Ac. Sci.) **51**(4), (2016) 312. 7

[42] A. Sargsyan, A. Amiryan, T. A. Vartanyan, and D. Sarkisyan. *Studying the regime of complete decoupling of the bond between the electron and nuclear moments at the D_1-line of the ^{39}K potassium isotope using a spectroscopic microcell.* Opt. Spectrosc. **121**(6), (2016) 790. 8

[43] A. D. Sargsyan, A. O. Amiryan, C. Leroy, T. A. Vartanyan, P. A. Petrov, and D. A. Sarkisyan. *Extreme increase in atomic transition probability of the Cs D_2 line in strong magnetic fields under selective reflection.* J. Opt. Technol. **83**(11), (2016) 654. 8

[44] A. Sargsyan, A. Amiryan, C. Leroy, T. A. Vartanyan, and D. Sarkisyan. *The effect of electromagnetically induced transparency in a potassium nanocell.* Opt. Spectrosc. **123**(1), (2017) 139. 8

[45] A. Sargsyan, A. Amiryan, S. Cartaleva, and D. Sarkisyan. *Nanocell with a pressure-controlled Rb atomic vapor column thickness: Critical influence of the thickness on optical processes.* J. Exp. Theor. Phys. **125**(1), (2017) 43. 8, 70

[46] A. H. Amiryan. *Theoretical investigation of the Faraday rotation effect in atomic alkali nano-layers.* J. Contemp. Phys. (Armenian Ac. Sci.) **53**(3), (2018) 212. 8

[47] A. Amiryan, A. Sargsyan, Y. Pashayan-Leroy, C. Leroy, and D. Sarkisyan. *Faraday rotation in cesium nano-layers in strong magnetic fields.* J. Mod. Opt. **66**(3), (2019) 328. 8, 96, 98

[48] A. Sargsyan, A. Tonoyan, G. Hakhumyan, A. Amiryan, P. Todorov, S. Cartaleva, and D. Sarkisyan. *Modified Faraday rotation method for studying cesium atomic lines in strong magnetic fields.* J. Contemp. Phys. (Armenian Ac. Sci.) **54**(1), (2019) 84. 8

[49] A. Sargsyan, A. Amiryan, T. A. Vartanyan, and D. Sarkisyan. *A modified method of Faraday rotation for investigation of atomic lines of rubidium and potassium in ultrathin cells.* Opt. Spectrosc. **126**(3), (2019) 173. 9

[50] A. Sargsyan, A. Amiryan, and D. Sarkisyan. *Faraday effect in rubidium atomic layers thinner than 100 nm.* J. Exp. Theor. Phys. **128**(3), (2019) 341. 9

[51] W. Demtröder. *Laser spectroscopy: basic concepts and instrumentation.* Springer Science & Business Media (2013). 9, 10, 11, 19, 42, 60, 82, 99, 104

[52] D. A. Smith and I. G. Hughes. *The role of hyperfine pumping in multilevel systems exhibiting saturated absorption.* Am. J. Phys **72**(5), (2004) 631. 9, 10, 11, 12

[53] A. Zibrov, C. Ye, Y. Rostovtsev, A. Matsko, and M. Scully. *Observation of a three-photon electromagnetically induced transparency in hot atomic vapor.* Phys. Rev. A **65**(4), (2002) 043817. 12

[54] R. Wynands and A. Nagel. *Precision spectroscopy with coherent dark states.* Appl. Phys. B **68**(1), (1999) 1. 13, 15, 16

[55] I. Ben-Aroya and G. Eisenstein. *Observation of large contrast electromagnetically induced absorption resonance due to population transfer in a three-level Λ-system interacting with three separate electromagnetic fields.* Opt. Express **19**(10), (2011) 9956. 16

[56] A. Sargsyan, D. Sarkisyan, and A. Papoyan. *Dark-line atomic resonances in a submicron-thin Rb vapor layer.* Phys. Rev. A **73**, (2006) 033803. 19

[57] D. Sarkisyan and A. Papoyan. *Formation of narrow optical resonances using submicron-thin atomic vapor layers.* World Scientific (2010). 21

[58] E. Jahier, J. Guéna, P. Jacquier, M. Lintz, A. Papoyan, and M. Bouchiat. *Temperature-tunable sapphire windows for reflection loss-free operation of vapor cells.* Appl. Phys. B **71**(4), (2000) 561. 22

[59] A. Sargsyan, G. Hakhumyan, R. Mirzoyan, and D. Sarkisyan. *Investigation of atomic transitions of cesium in strong magnetic fields by an optical half-wavelength cell.* JETP letters **98**(8), (2013) 441. 23, 94

[60] D. A. Steck. *Cesium D Line Data* **49**(revision 2.1.2, 12). 26, 41, 43, 60

[61] C. Alcock, V. Itkin, and M. Horrigan. *Vapour pressure equations for the metallic elements: 298–2500K.* Can. Metall. Quart. **23**(3), (1984) 309. 26

[62] T. Tiecke. *Properties of potassium.* University of Amsterdam, The Netherlands, Thesis pages 12–14. 26

[63] A. Corney. *Atomic and Laser Spectroscopy.* Oxford Science Pub (1977). 37

[64] E. Arimondo, M. Inguscio, and P. Violino. *Experimental determinations of the hyperfine structure in the alkali atoms.* Rev. Mod. Phys. **49**(1), (1977) 31. 37

[65] P. Tremblay, A. Michaud, M. Levesque, S. Thériault, M. Breton, J. Beaubien, and N. Cyr. *Absorption profiles of alkali-metal D lines in the presence of a static magnetic field.* Phys. Rev. A **42**(5), (1990) 2766. 39, 91, 93

[66] A. Sargsyan, A. Tonoyan, G. Hakhumyan, C. Leroy, Y. Pashayan-Leroy, and D. Sarkisyan. *Complete hyperfine Paschen-Back regime at relatively small magnetic fields realized in potassium nano-cell.* EPL **110**(2), (2015) 23001. 45, 66, 106

[67] B. Olsen, B. Patton, Y.-Y. Jau, and W. Happer. *Optical pumping and spectroscopy of Cs vapor at high magnetic field.* Phys. Rev. A **84**(6), (2011) 063410. 45, 46, 66, 105, 106

[68] M. Faraday. *Experimental researches in electricity.* J. M. Dent & Sons LTD (1922). 54

[69] V. Yashchuk, D. Budker, W. Gawlik, D. Kimball, Y. P. Malakyan, and S. Rochester. *Selective addressing of high-rank atomic polarization moments.* Phys. Rev. Lett. **90**(25), (2003) 253001. 54

[70] Y. Wang, X. Zhang, D. Wang, Z. Tao, W. Zhuang, and J. Chen. *Cs Faraday optical filter with a single transmission peak resonant with the atomic transition at 455 nm.* Opt. Express **20**(23), (2012) 25817. 54

[71] J. A. Zielińska, F. A. Beduini, N. Godbout, and M. W. Mitchell. *Ultranarrow Faraday rotation filter at the Rb D_1 line.* Opt. Lett. **37**(4), (2012) 524. 54

[72] M. A. Zentile, D. J. Whiting, J. Keaveney, C. S. Adams, and I. G. Hughes. *Atomic Faraday filter with equivalent noise bandwidth less than 1 GHz.* Opt. Lett. **40**(9), (2015) 2000. 54

[73] L. Weller, K. Kleinbach, M. A. Zentile, S. Knappe, I. Hughes, and C. Adams. *Optical isolator using an atomic vapor in the hyperfine Paschen–Back regime.* Opt. Lett. **37**(16), (2012) 3405. 54

[74] M. A. Zentile, R. Andrews, L. Weller, S. Knappe, C. S. Adams, and I. G. Hughes. *The hyperfine Paschen–Back Faraday effect.* J. Phys. B **47**(7), (2014) 075005. 54

[75] O. Galstyan, H. Lee, A. Babajanyan, A. Hakhoumian, B. Friedman, and K. Lee. *Magneto-optical visualization by Bi: YIG thin films prepared at low temperatures.* J. Appl. Phys **117**(16), (2015) 163914. 54

[76] W. Gawlik, J. Kowalski, R. Neumann, and H. Wiegemann. *A new method for measuring oscillator strengths using the resonant Faraday effect in monochromatic light.* J. Phys. B **12**(23), (1979) 3873. 54

[77] A. Sargsyan, Y. Pashayan-Leroy, C. Leroy, Y. Malakyan, and D. Sarkisyan. *Features of Faraday rotation in Cs atomic vapor in a cell thinner than the wavelength of light.* JETP letters **102**(8), (2015) 487. 54

[78] A. Sargsyan, Y. Pashayan-Leroy, C. Leroy, and D. Sarkisyan. *Faraday effect on the Rb D_1 line in a cell with a thickness of half the wavelength of light.* J. Exp. Theor. Phys. **123**(3), (2016) 395. 54, 70

[79] J. Peatross and M. Ware. *Physics of light and optics.* Brigham Young University, Department of Physics (2011). 55

[80] K. T. McDonald. *Faraday rotation* (2008). 56, 57

[81] A. Sargsyan, E. Klinger, G. Hakhumyan, A. Tonoyan, A. Papoyan, C. Leroy, and D. Sarkisyan. *Decoupling of hyperfine structure of Cs D_1 line in strong magnetic field studied by selective reflection from a nanocell.* J. Opt. Soc. Am. B **34**(4), (2017) 776. 62, 67, 68

[82] A. Sargsyan, G. Hakhumyan, C. Leroy, Y. Pashayan-Leroy, A. Papoyan, and D. Sarkisyan. *Hyperfine Paschen–Back regime realized in Rb nanocell.* Opt. Lett. **37**(8), (2012) 1379. 66, 86

[83] D. J. Whiting, R. S. Mathew, J. Keaveney, C. S. Adams, and I. G. Hughes. *Four-wave mixing in a non-degenerate four-level diamond configuration in the hyperfine Paschen–Back regime.* J. Mod. Opt **65**(5-6), (2018) 713. 66

[84] A. Weis, V. Sautenkov, and T. Hänsch. *Magneto-rotation and magnetic circular dichroism of cesium atoms near a dielectric surface.* J Phys II **3**(3), (1993) 263. 68, 70

[85] A. Sargsyan, A. Papoyan, I. G. Hughes, C. S. Adams, and D. Sarkisyan. *Selective reflection from an Rb layer with a thickness below $\lambda/12$ and applications.* Opt. Lett. **42**(8), (2017) 1476. 69, 77, 101, 102, 107

[86] D. Bloch and M. Ducloy. *Atom-wall interaction.* Adv. At. Mol. Opt. Phys **50**, (2005) 91. 71

[87] C. Sukenik, M. Boshier, D. Cho, V. Sandoghdar, and E. Hinds. *Measurement of the Casimir-Polder force.* Phys. Rev. Lett. **70**(5), (1993) 560. 72

[88] J. Keaveney. *Collective atom–light interactions in dense atomic vapours.* Springer (2014). 73, 74

[89] A. Sargsyan, G. Hakhumyan, and D. Sarkisyan. *Use of sub-Doppler optical resonances for measurement of weak magnetic fields by means of extremely thin rubidium vapor cell.* J. Contemp. Phys. (Armenian Ac. Sci.) **47**(2), (2012) 64. 74

[90] K. Whittaker, J. Keaveney, I. Hughes, A. Sargsyan, D. Sarkisyan, and C. Adams. *Spectroscopic detection of atom-surface interactions in an atomic-vapor layer with nanoscale thickness.* Phys. Rev. A **92**(5), (2015) 052706. 75

[91] M. Chevrollier, M. Fichet, M. Oria, G. Rahmat, D. Bloch, and M. Ducloy. *High resolution selective reflection spectroscopy as a probe of long-range surface interaction: measurement of the surface van der Waals attraction exerted on excited Cs atoms.* J. Phys.II **2**(4), (1992) 631. 75, 101, 102

[92] T. Peyrot, Y. Sortais, A. Browaeys, A. Sargsyan, D. Sarkisyan, J. Keaveney, I. Hughes, and C. S. Adams. *Collective Lamb shift of a nanoscale atomic vapor layer within a sapphire cavity.* Phys. Rev. Lett. **120**(24), (2018) 243401. 75

[93] A. Sargsyan, A. Tonoyan, G. Hakhumyan, and D. Sarkisyan. *Magnetically induced anomalous dichroism of atomic transitions of the cesium D_2 line.* JETP Letters **106**(11), (2017) 700. 83, 91

[94] A. Tonoyan, A. Sargsyan, E. Klinger, G. Hakhumyan, C. Leroy, M. Auzinsh, A. Papoyan, and D. Sarkisyan. *Circular dichroism of magnetically induced transitions for D_2 lines of alkali atoms.* EPL **121**(5), (2018) 53001. 83, 91

[95] A. Sargsyan, E. Klinger, A. Tonoyan, C. Leroy, and D. Sarkisyan. *Hyperfine Paschen–Back regime of potassium D_2 line observed by Doppler-free spectroscopy.* J. Phys. B **51**(14), (2018) 145001. 87, 106

[96] A. Sargsyan, G. Hakhumyan, A. Papoyan, and D. Sarkisyan. *Alkali metal atoms in strong magnetic fields: Guiding atomic transitions foretell the characteristics of all transitions of the D_1 line.* JETP Letters **101**(5), (2015) 303. 87, 92

[97] A. Sargsyan, E. Klinger, Y. Pashayan-Leroy, C. Leroy, A. Papoyan, and D. Sarkisyan. *Selective reflection from Rb vapor in half-and quarter-wave cells: features and possible applications.* JETP letters **104**(4), (2016) 224. 88

[98] A. Sargsyan, A. Tonoyan, G. Hakhumyan, A. Papoyan, E. Mariotti, and D. Sarkisyan. *Giant modification of atomic transition probabilities induced by a magnetic field: forbidden transitions become predominant.* Laser Phys. Lett. **11**(5), (2014) 055701. 91

[99] E. Klinger, A. Sargsyan, A. Tonoyan, G. Hakhumyan, A. Papoyan, C. Leroy, and D. Sarkisyan. *Magnetic field-induced modification of selection rules for Rb D_2 line monitored by selective reflection from a vapor nanocell.* Eur. Phys. J. D **71**(8), (2017) 216. 91

[100] M. Witkowski, G. Kowzan, R. Munoz-Rodriguez, R. Ciuryło, P. S. Żuchowski, P. Masłowski, and M. Zawada. *Absolute frequency and isotope shift measurements of mercury $^1S_0$–$^3P_1$ transition.* Opt. Express **27**(8), (2019) 11069. 105

[101] T. Peyrot, C. Beurthe, S. Coumar, M. Roulliay, K. Perronet, P. Bonnay, C. Adams, A. Browaeys, and Y. Sortais. *Fabrication and characterization of super-polished wedged borosilicate nano-cells.* Opt. Lett. **44**(8), (2019) 1940. 105

[102] A. Sargsyan, A. Tonoyan, A. Papoyan, and D. Sarkisyan. *Dark resonance formation with magnetically induced transitions: extension of spectral range and giant circular dichroism.* Opt. Lett. **44**(6), (2019) 1391. 107

Formation of narrow optical resonances in thin atomic vapor layers of Cs, Rb, K and applications

Abstract:

This thesis presents the study of coherent light interaction with a sub-wavelength atomic alkali vapor layer confined in a nano-cell and applications for the formation of narrow optical resonances.

We develop a theoretical model describing the resonant interaction of the laser light with the thin alkali vapor layer in the presence of an external static magnetic field. We show that due to a transient regime of interaction, only slow atoms contribute to the signal and their transmission spectrum is essentially Doppler-free. The nature of the obtained spectra makes the transmission spectroscopy from a nano-cell a convenient technique to perform studies of closely-spaced atomic transitions and investigate their behavior in magnetic fields. Experimental realizations for magnetic fields up to 7000 G show an excellent agreement between theory and experiment.

We also explore the Faraday rotation of the plane polarization of light with the propagation through the thin atomic slab. We see that despite a small angle of rotation, Faraday rotation spectra exhibit resonances narrower than that for transmission. At last, we investigate new possibilities to form narrow optical resonances in nano-cells and show that second derivation processing of transmission spectra yields the strongest line narrowing among all methods studied in this thesis.

Keywords: *sub-Doppler spectroscopy*; *nano-cell*; *alkali vapors*; *Faraday rotation*; *Zeeman effect.*

Formation de résonances optiques étroites dans des couches fines de vapeur atomique de Cs, Rb, K et applications.

Résumé :

Cette thèse présente l'étude de l'interaction de lumière cohérente avec une couche sub-longueur d'onde de vapeur alcaline atomique confinée en nano-cellule et applications pour la formation de résonances optiques étroites.

Nous développons un modèle théorique décrivant l'interaction résonante de lumière laser avec la couche mince de vapeur alcaline en présence d'un champ magnétique. Nous montrons qu'en raison d'un régime transitoire d'interaction, seuls les atomes lents contribuent au signal et leur spectre de transmission est essentiellement sans effet Doppler. La nature des spectres obtenus fait de la spectroscopie de transmission, en nano-cellule, une technique pratique pour l'étude de transitions très rapprochées et l'évolution de leur comportement dans un champ magnétique. Des expériences réalisées pour des champs magnétiques jusqu'à 7000 G montrent un excellent accord entre théorie et expérience.

Nous explorons aussi la rotation Faraday du plan de polarisation de la lumière lors de sa propagation dans la couche mince atomique. Bien que l'angle de rotation soit très faible, nous observons que les résonances des spectres de rotation Faraday sont plus étroites que celles de transmission. Enfin, nous étudions de nouvelles possibilités pour former des résonances optiques étroites et montrons qu'un traitement par deuxième dérivée des spectres de transmission donne le meilleur rétrécissement de raies parmi toutes les méthodes étudiées dans cette thèse.

Mots clefs : *spectroscopie sub-Doppler*; *nano-cellule*; *vapeurs alcalines*; *rotation Faraday*; *effet Zeeman.*